Origin and fate of vascular smooth muscle cells during vascular remodeling and reverse remodeling in pulmonary hypertension

Inaugural Dissertation
submitted to the
Faculty of Medicine
in partial fulfillment of the requirements
for the PhD-Degree
of the Faculties of Veterinary Medicine and Medicine
of the Justus Liebig University Giessen
by
Xuran Chu
of
Heilongjiang, China
Giessen 2022

From the Department of Internal Medicine and
Excellence Cluster Cardio-Pulmonary System (ECCPS)
Director / Chairman: Prof. Dr. Werner Seeger
Faculty of Medicine of the Justus Liebig University Giessen

First Supervisor and Committee Member: Prof. Dr. Saverio Bellusci
Second Supervisor and Committee Member: Reinhard H. Dammann
Committee Members (Chair): Prof. Dr. Norbert Weissman

Defense date: 2022.06.10

Declaration

"I declare that I have completed this dissertation single-handedly without the unauthorized help of a second party and only with the assistance acknowledged therein. I have appropriately acknowledged and referenced all text passages that are derived literally from or are based on the content of published or unpublished work of others, and all information that relates to verbal communications. I have abided by the principles of good scientific conduct laid down in the charter of the Justus Liebig University of Giessen in carrying out the investigations described in the dissertation."

Xuran Chu
Giessen, Febrary, 2022

Table of Contents

List of Tables

Table 1. Primer sequences and running protocols for genotyping.

Table 2. Expected band size of genotyping products.

Table 3. Primer sequences (forward/reverse) for qPCR.

List of Figures

Abbreviations and Acronyms

ACTA2	Alpha smooth muscle actin
ADRP	Adipose Differentiation-Related Protein
AECI	Alveolar epithelial cell type I
AECII	Alveolar Epithelial type II cells
ANOVA	Analysis of variance
ASMC	Airway smooth muscle cell
BCA	Bicinchoninic acid
BMP2	Bone Morphogenesis Protein
BPD	Bronchopulmonary dysplasia
BSA	Bovine Serum Albumin
cDNA	Complementary DNA
COPD	Chronic Obstructive Pulmonary Diseases
Cre-ERT2	Fusion protein between Cyclization recombinase and triple mutated human estrogen receptor ligand binding domain
DAPI	4′,6-diamidino-2-phenylindole
DNA	Deoxyribonucleic acid
d.p.i.	Day post instillation
DTT	Dithiothreitol
DTR	Diphtheria toxin receptor
ECM	Extra Cellular Matrix
EDTA	Ethylenediaminetetraacetic acid
EMT	Epithelial to Mesenchymal Transition
FACS	Fluorescent Activated Cell Sorting
FDA	Food and Drug Administration
FGF10	Fibroblast Growth Factor 10
FGFR	Fibroblast Growth Factor receptor
FITC	Fluorescein isothiocyanate
FSC	Forward scatter
GLI1	Glioma-associated oncogene 1
HBSS	Hank’s balanced salt solution
iDTR	*Cre*-inducible DTR transgenic mice

IF	Immunofluorescence
IP	Intraperitoneal
IPF	Idiopathic Pulmonary Fibrosis
LacZ	Bacterial β-galactosidase gene
LIF	Lipofibroblast
mT/mG	Membrane-targeted tdTomato/membrane-Targeted green fluorescent protein
MYF	Myofibroblast
NG2	Neural/Glial antigen 2
PAH	Pulmonary Arterial Hypertension
PBS	Phosphate buffered saline
PCLS	Precision-cut lung slices
PCR	Polymerase chain reaction
PDGFrα	Platelet Derived Growth Factor receptor α
PDGFrβ	Platelet Derived Growth Factor receptor β
P-value	Probability
qPCR	Quantitative polymerase chain reaction
RFP	Red fluorescent protein
SFTPC	Surfactant protein C
SDS-PAGE	Sodium dodecyl sulfate-polyacrylamide gel electrophoresis
SMC	Smooth muscle cell
SMO	Smoothend
SSC	Side scatter
SHH	Sonic hedgehog
SPF	Specific Pathogen-Free
TAE	Tris-acetate-EDTA buffer
Tam	Tamoxifen
tdTom	tdTomato
TGFβ	Transforming growth factor beta
VSMC	Vascular smooth muscle cells
WT	Wild type

Introduction

Pulmonary Hypertension

Pulmonary hypertension (PH) is a progressive disease defined by a resting mean pulmonary arterial pressure (mPAP) greater than or equal to 25 mmHg, assessed by right heart catheterization. One of the hallmark features of PH is the remodeling process occurring in the pulmonary vasculature, including but not limited to, excessive accumulation of vascular smooth muscle cells (VSMCs), deposition of extracellular matrix (ECM) proteins, and infiltration of inflammatory cells. These pathological events lead to stiffening of the vascular walls and increased vascular resistance. When left untreated, PH can lead to right heart failure (Schermuly, Ghofrani et al. 2011, Galiè, Humbert et al. 2016, Humbert, Guignabert et al. 2019). The vasculature of the adult lung can be classified into three categories based on the degree of muscularization: Proximal fully-muscularized vessels, middle partially muscularized vessels, and distal non-muscularized vessels. During PH development, there is an increased muscularization of the already muscularized proximal and middle vessels and neo-muscularization of the distal vessels. The remodeling process leads to restriction of the microcirculation and contributes profoundly to increased pulmonary vascular resistance and pressure. The cellular origin of newly formed VSMCs has gained increasing interest in recent years as it 1) contributes to the overall understanding of PH pathogenesis and 2) may help develop novel therapies targeted against culprit cells/signaling pathways in affected patients. To this end, the dominant model is that newly formed VSMCs derive from pre-existing VSMCs that expand distally along the vascular tree. In this study, we speculate that GLI1+ cells represent a novel origin of newly formed PH-associated VSMCs, besides pre-existing VSMC during PH.

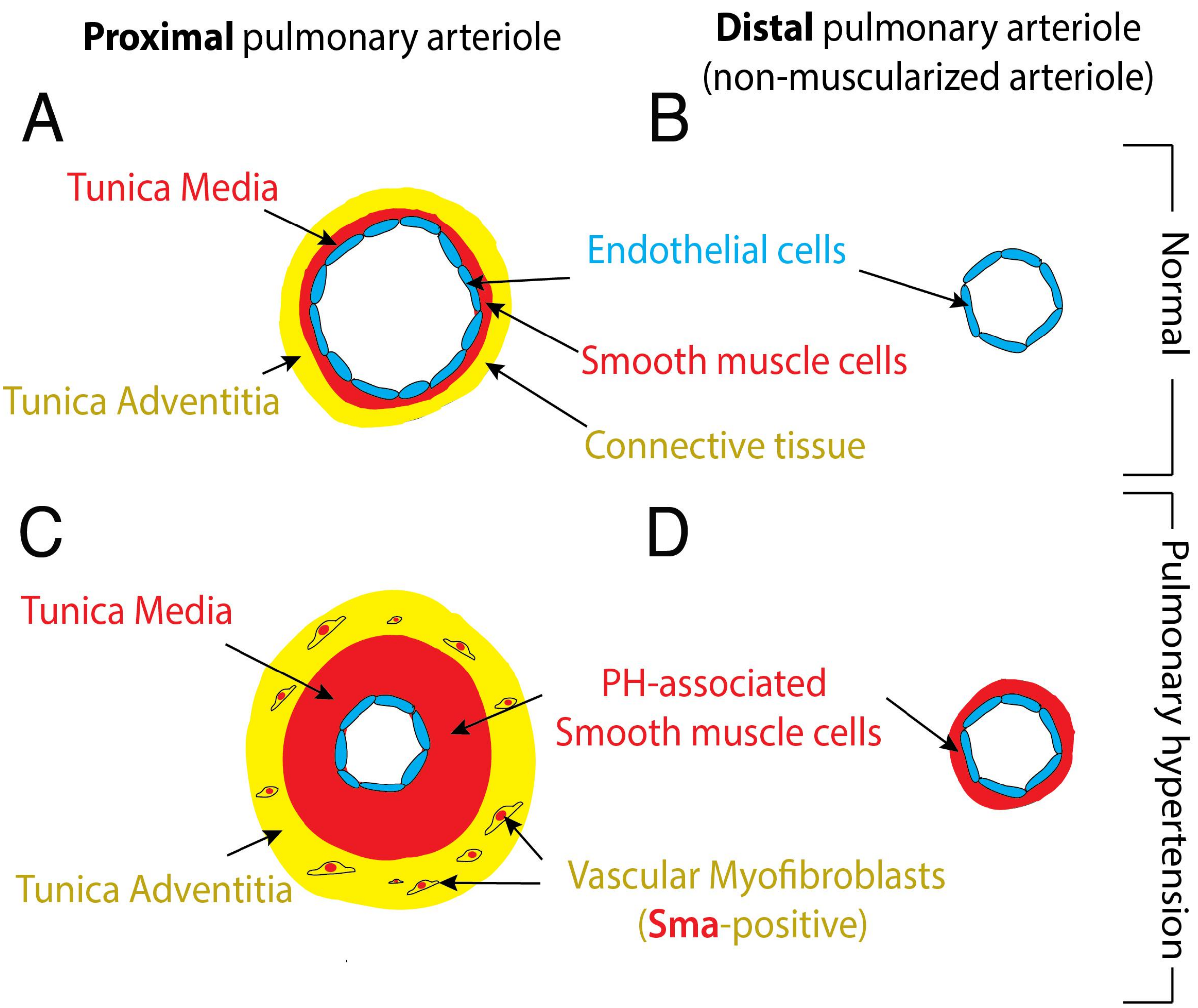

Figure 1. Schematic representation of vascular remodeling during pulmonary hypertension. (A). Under normal condition, the proximal vessels contain three layers: tunica intima, tunica media and tunica adventitia. **(B).** Under normal condition, there is only one layer of endothelial cells in the distal vessels. **(C)**. During PH, in the proximal vessels, the VSMCs in tunica media layer proliferate and the VMs in tunica adventitia layer also proliferate. **(D).** During PH, the non-muscularized distal vessels get muscularized. PH: pulmonary hypertension; VSMC: vascular smooth muscle cells; VMs: vascular myofibroblasts.

The Sonic Hedgehog (Shh) Pathway

The Sonic hedgehog (Shh) pathway is identified as one of the most significant pathways during embryonic development. *Shh* knock-out mice fail to develop many organs such as lung, brain skeletal, and gastrointestinal tract. Recent studies have shown that Shh pathway also plays an important role in regulating stem cell homeostasis in the adult stage. For instance, hedgehog signaling actively maintained quiescence of mesenchyme in the adult lung (Peng, Frank et al. 2015). Deletion of *Shh* in the lung epithelium causes proliferative expansion of adjacent lung mesenchyme.

The mammalian Shh pathway consists of three ligands: Shh, Indian-Hedgehog, and Desert-Hedgehog. The canonical activation occurs in the presence of HH ligands. Binding of HH ligand to PTCH prevents inhibition of SMO by PTCH. SMO is released from the inhibition of PTCH and turns on downstream gene expressions, such as Gli1 and Ptch1. In the absence of HH ligands, PTCH blocks SMO and therefore suppresses induction of GLI1 target gene expression.

During pulmonary hypertension, blood vessels in patients' lungs exhibit abnormal proliferation capacity, resulting in remodeling of the pulmonary vascular system and occlusion of the vascular lumen (Peng, Frank et al. 2015). Altogether, the role of SHH signaling pathway during vasculature injury and repair process appears to be important. To investigate the mechanism of vascular remodeling we first need to understand the regulating signaling pathway behind it.

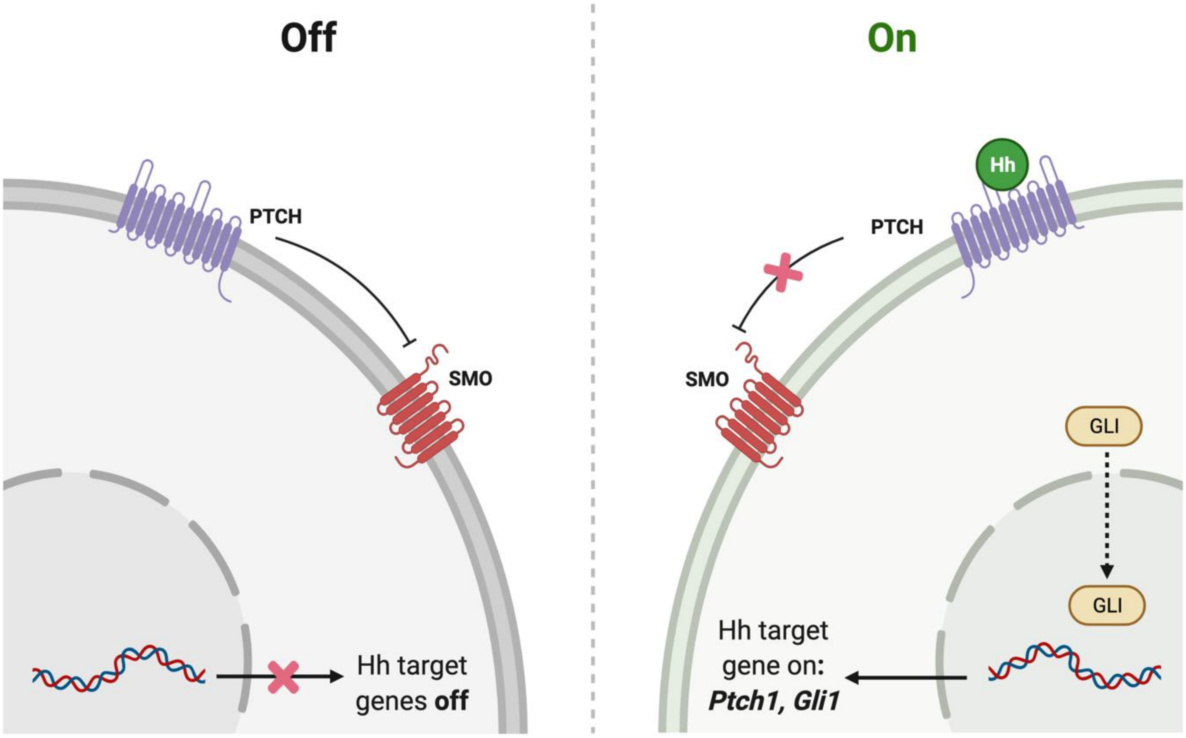

Figure 2. The sonic hedgehog (Shh) pathway. (**A**). when the signaling pathway is off, Hh ligands are absent, wherein PTCH inhibits SMO resulting in the off state of transcription. (**B**). when signal pathway is on, Hh ligand reaches its target cell and then binds to PTCH receptor. PTCH inhibits SMO, a downstream protein in the pathway. The binding of Hh ligands to PTCH relieves inhibition of SMO, leading to activation of the GLI transcription factors. The accumulation of GLI1 results in activation of target genes. Hh-sonic hedgehog; PTCH-Patched; SMO-Smoothened; GLI-glioma-associated oncogene. (Created with BioRender.com)

Origin of vascular smooth muscle cells (VSMCs) during PH

PH is a progressive disease without an effective cure. To investigate new therapeutic methods, and to study the pathogenesis of PH becomes more and more important. The study to look for the origins of the PH-associated VSMCs has gained momentum recently. Previous studies have demonstrated that resident SMC in pulmonary vasculature could be the major source of newly formed PH-associated VSMCs. However, more and more studies showed that the origin of disease involved VSMCs during vascular remodeling could be heterogeneous. Here we have summarized the mainstream theories in the field regarding this study. We proposed a novel population of cells, which also contribute to the pathogenic VSMC pool in vascular remodeling during PH.

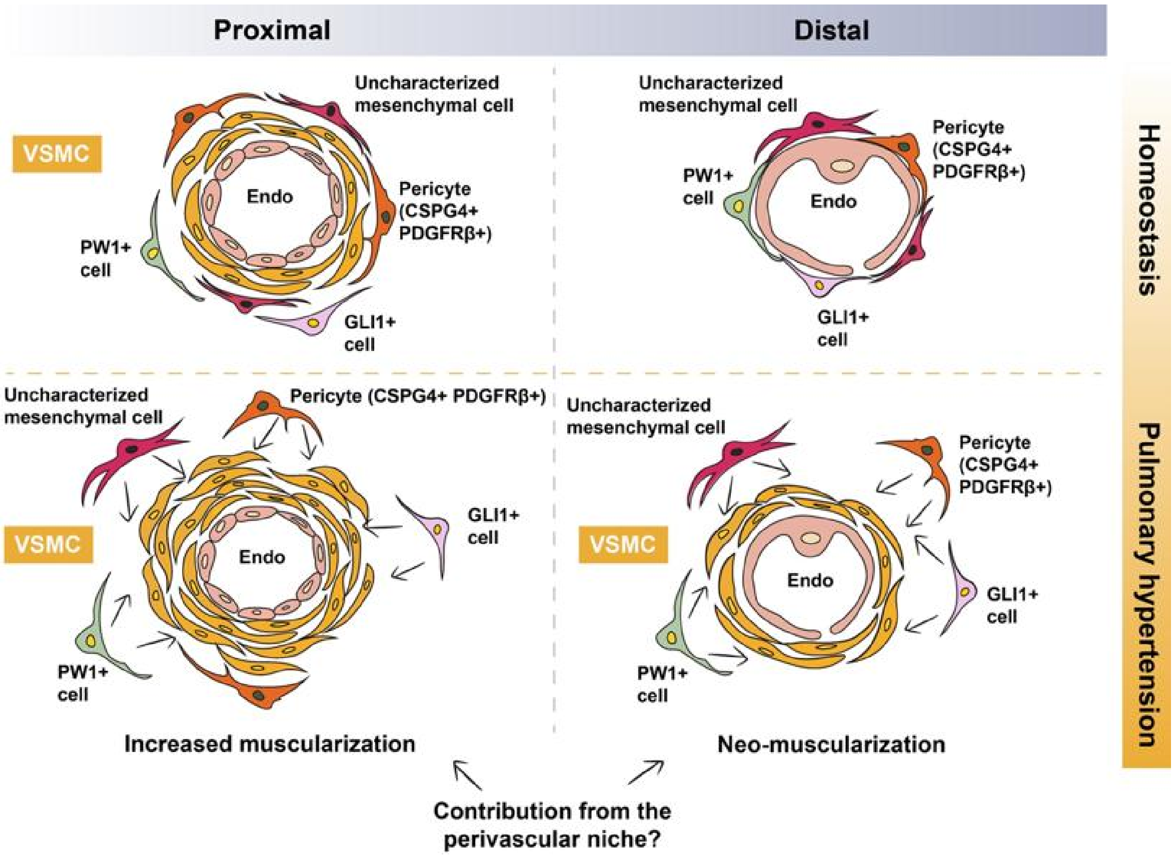

Figure 1. Proposed model of contribution of perivascular mesenchymal cells to pulmonary hypertension-associated vascular smooth muscle cells. Under homeostatic conditions, proximal vessels are muscularized while distal vessels are non-muscularized. There is increased muscularization of already muscularized vessels and neo-muscularization of non-muscularized vessels during vascular remodeling. Possible perivascular sources of VSMCs include pericytes, PW1+ cells, GLI1+ cells and other uncharacterized mesenchymal cells. VSMC: Vascular smooth muscle cell (Chu, Ahmadvand et al. 2021).

Resident smooth muscle cells

Experimental studies using hypoxia-induced PH in mice suggest that newly formed VSMCs derive from pre-existing VSMCs that initially occupy the proximal regions of the vascular tree, or at least from pre-existing ACTA2+ precursors. For instance, when several lineage-tracing mouse lines were used to map the fate of pre-existing (labeled before injury) CDH5+ (cadherin 5; vascular endothelial cadherin or VE-cadherin: endothelial marker), CSPG4+ (chondroitin sulfate proteoglycan 4; neuron-glial antigen 2 or NG2: pericytes marker), PDGFRα+ (platelet-derived growth factor receptor alpha: fibroblast marker), ACTA2+ and MYH11+ cells following hypoxia or house dust mite (HDM) exposure, the major contribution to newly formed VSMCs appeared to be originated from ACTA2+ and MYH11+ cells (Crnkovic, Marsh et al. 2018). The same study demonstrated that there is a global increase in the proliferation of the resident mesenchymal cell types mentioned above. The analysis focused on the vessels whose diameter was less than or equal to 35 µm, as these vessels lack any VSMCs in the absence of PH-associated remodeling. It is important to mention that labeling of endothelial cells in that study was incomplete and that the CSPG4+ lineage labeled around 20% of VSMCs under hypoxic conditions (Crnkovic, Marsh et al. 2018). Another note is that hypoxia represents a mild form of PH in mice and does not recapitulate the severity of human PAH including the formation of neointima and plexiform lesions.

Another elegant work showed that the progenitors of newly formed VSMCs are discrete “primed” VSMCs occupying the (muscularized) proximal - (non-muscularized) distal borders (Sheikh, Lighthouse et al. 2014). In response to hypoxia, such primed cells sequentially undergo dedifferentiation (loss of *Smmhc* expression), distal migration, clonal expansion and differentiation (reacquisition of *Smmhc* expression). These progenitors were suggested to be platelet-derived growth factor receptor beta-positive (PDGFRβ+)(Sheikh, Lighthouse et al. 2014). Endothelial cell and macrophage-derived platelet-derived growth factor B (*Pdgfb*) is dysregulated under hypoxic conditions and seems to be important for the activation of PDGFRβ+ progenitors (Sheikh, Misra et al. 2015, Ntokou, Dave et al. 2021). Moreover, the pluripotency factor Kruppel-like factor 4 (*Klf4*) was found to be upregulated in these cells, and it seems that its expression is important for neo-muscularization of distal pulmonary arterioles (Sheikh, Misra et al. 2015). These findings are based on state-of-the-art experimental approaches and analytical tools such as lineage tracing, clonal analysis, and the use of confocal imaging and 3D reconstruction of thick lung sections to analyze the “same” vessel segment in control and experimental samples.

More recently, chronic HDM treatment was combined with hypoxia exposure in mice to generate an inflammatory model that mimics PAH severity in terms of perivascular inflammation, elevated right ventricular pressures, medial thickening, and neointima formation. In this model, no clonal expansion of pre-existing VSMCs was observed but rather the proliferation of random VSMCs during medial thickening. Intriguingly, the authors showed that VSMCs expressing *Notch3*, but not endothelial cells, are the cellular source of neointima in this mode (Steffes, Froistad et al. 2020).

To sum up, these studies suggest that newly formed VSMCs in PH predominantly derive from pre-existing VSMCs located proximally. In the next sections, we present data suggesting that there are alternative cellular sources for these cells apart from proximal VSMCs.

Endothelial-to-mesenchymal transition (EndMT)

Endothelial cells form a monolayer of cells residing in the tunica intima (innermost layer) of blood vessels. They act as a barrier between circulating blood and various organs and tissues, thus controlling the traffic of nutrients, immune cells, cytokines, growth factors, and other substances between the two compartments. Endothelial-to-mesenchymal transition (EndMT) is a process by which endothelial cells lose their endothelial phenotype and acquire mesenchymal marker expression such as *Acta2*. Evidence for this phenomenon stems from early experiments involving primary cultures of endothelial cells (Arciniegas, Sutton et al. 1992, Frid, Kale et al. 2002). Although this process has been sometimes perceived as a rare event, there is a strong notion that EndMT is an important mechanism for VSMC accumulation during PH pathogenesis. Analysis of the expression of endothelial (such as CD31, CD34, VE-cadherin, and von Willebrand factor) and mesenchymal markers (such as ACTA2) are usually used to identify cells that are transitioning between the two states.

Analysis of immuno-stained lung sections revealed that the endothelial markers CD31, CD34, and VE-cadherin show diffuse staining in the intima and plexiform lesions of PAH samples and sometimes co-localize with ACTA2 expression, as opposed to a strong staining of the thin endothelial layer adjacent to ACTA2+ VSMCs in the non-PAH group (Ranchoux, Antigny et al. 2015). Using a novel rat model of spontaneous PH development linked to the human *BMPR2* mutations, the expression levels of the EndMT markers Twist1 and Phospho-vimentin were found to be increased in the lungs of these rats (Ranchoux, Antigny et al. 2015). It was also proposed that decreased *BMPR2* expression in endothelial cells induces the upregulation of high mobility group AT-hook 1 (*HMGA1*), leading to EndMT in PAH (Arciniegas, Sutton et al.). This mechanism was demonstrated using *in vitro* cultures of pulmonary artery endothelial cells and the expression data were validated by immunostaining of PAH lung explants. EndMT was identified by the loss of CD31 protein expression and gain of ACTA2, SM22α, Calponin, Phospho-vimentin, and Slug expression. Interestingly, EndMT could be reversed via co-inhibition of *HMGA1* or *Slug* expression (Hopper, Moonen et al. 2016).

In another study, endothelial cells were labeled *in vivo* using *Cdh5-Cre* or *Tie2-Cre* mouse driver lines combined with the *Rosa26*$^{mT/mG}$ reporter line in the context of left lung pneumonectomy followed by monocrotaline (MCT) treatment(Qiao, Nishimura et al. 2014). The authors reported that in this severe model of PH in mice, labeled cells contributed to neointima formation and that these cells expressed *Acta2* and *Smmhc*. Additionally, cells expressing both endothelial and smooth muscle markers were shown to be present in neointimal lesions of human PAH lung tissues (Qiao, Nishimura et al. 2014).

EndMT was also reported in the sugen/hypoxia model of PH in mice. The *Cdh5-Cre* mouse driver line was used in combination with the *Rosa26*$^{mT/mG}$ reporter line to isolate GFP+ CDH5- cells (EndMT cells) (Suzuki, Carrier et al. 2018). EndMT cells were enriched with stem cell antigen 1 (*Sca-1*) expression and displayed high proliferative and migratory properties. *In vitro* assays showed that EndMT cells contribute not only to VSMC-like cells but also to intimal and medial proliferation via paracrine-acting factors(Suzuki, Carrier et al. 2018). Finally, endothelial-like cells isolated from chronic thromboembolic pulmonary hypertension (CTEPH) patients were proposed to transit to mesenchymal phenotypes and display endothelial dysfunction when exposed to myofibroblast-like cells or their conditioned medium (Sakao, Hao et al. 2011).

Contribution of Perivascular Mesenchymal (Progenitor) Cells

During embryonic lung development in mice, arterial walls are constructed radially through a mechanism that is coordinated by two processes: One involves the successive incorporation of cells from the surrounding PDGFRβ+ mesenchyme to form the various layers, and the other one involves the invasion of the outer layer by inner-layer cells (Greif, Kumar et al. 2012). The latter process occurs via developmentally regulated cell reorientation and radial migration (Greif, Kumar et al. 2012). Such morphogenic process leads to the colonization of the tunica media of blood vessels by resident VSMCs.

As mentioned in the previous sections, distal vessels contain a single layer of endothelial cells and are, therefore, non-muscularized under homeostatic conditions. Thus, it is plausible that the muscularization of these non-muscularized vessels involves partial, or even full, recapitulation of the developmental process described above. In the microcirculation, endothelial cells are covered by mesenchymal cells such as pericytes characterized by the expression of PDGFRβ (Figure 3). Therefore, it is likely that the remodeling process involves the activation of “local” PDGFRβ+ cells, leading to their differentiation into bona fide VSMCs. In this section, we provide an overview of the literature that is in favor of this scenario.

Pericytes

Pericytes are mesenchymal cells residing in the perivascular space where they influence various aspects of vascular biology such as vessel stability, vascular tone, and ECM deposition, to name a few (Figure 1). Pericytes are also regarded as mesenchymal stem cells (MSC)-like cells due to their trilineage differentiation potential towards adipocytes, chondrocytes, and osteoblasts (Diaz-Flores, Gutierrez et al. 2009, Mills, Cowin et al. 2013, El Agha, Kramann et al. 2017). It has been demonstrated that pericytes coverage is significantly increased in pulmonary arteries of human PAH lungs (Ricard, Tu et al. 2014). Moreover, primary human lung pericytes isolated based on the expression of 3G5-ganglioside antigen (*3G5*) show increased proliferative and migratory responses when exposed to conditioned medium from PAH endothelial cells compared with controls, a mechanism that involves fibroblast growth factor 2 (FGF2) and interleukin 6 (IL-6) signaling pathways

(Ricard, Tu et al. 2014). Moreover, treatment of these cells with TGFβ1 leads to their transdifferentiation into smooth muscle-like cells. Increased pericytes coverage was also demonstrated in the MCT model in rats as well as the hypoxia model in mice. Finally, the *Cspg4-DsRed* reporter line showed that CSPG4+ cells indeed gain *Acta2* expression following exposure to hypoxia (Ricard, Tu et al. 2014).

In follow-up work, 3G5+ pericytes were isolated from human patients and shown to significantly express *NG2* and *PDGFRβ* in addition to classical MSC markers but little or no smooth muscle markers *SM22* and *SMMHC* (Bordenave, Tu et al. 2020). IPAH pericytes exhibit higher wound-closure, migratory and proliferative capabilities compared with their donor counterparts. While culturing donor and IPAH pericytes in the complete medium did not reveal major differences in terms of expression of contractile genes, serum starvation revealed a higher expression of *SM22*, *Calponin,* and a trend for *ACTA2* in IPAH pericytes (Bordenave, Tu et al. 2020). Moreover, lineage tracing of NG2+ cells showed an increase in the number of lineage-labeled cells and acquisition of *Acta2* expression. Blocking CXCL-12 signaling hindered pericytes accumulation in response to hypoxia in mice, and CXCR-7 mediated the excessive pericytes proliferation and migration in PAH. IPAH pericytes also displayed an exaggerated response to TGFβ1 stimulation likely due to higher expression of TGFβ receptor II (Bordenave, Tu et al. 2020).

Mesenchymal stem cells

The arterial adventitia has been described as a sonic hedgehog (SHH)-responsive domain that supports resident SCA-1+ vascular progenitor cells (Passman, Dong et al. 2008). Although such, and other, adventitial cells do not express SMC marker proteins *in vivo*, they express transcription factors that are involved in SMC differentiation, and they readily differentiate into SMC-like-cells *in vitro*. The perivascular region has been identified as an MSC domain in multiple human organs (Crisan, Yap et al. 2008)

PW1+ cells

Another population of perivascular MSC-like cells is the PW1+ population (Figure 3). PW1 is a zinc finger protein involved in the regulation of cell cycle and cell stress responses, β-catenin stabilization and metabolic homeostasis in addition to its requirement for the myogenic and migratory capabilities of mesangioblasts (Dierick, Hery et al. 2016). PW1+ cells were initially identified in murine skeletal muscle where *Pw1* is expressed in satellite cells and a subset of interstitial cells with myogenic potential (Pannérec, Formicola et al. 2013). PW1+ interstitial cells were shown to give rise to smooth and skeletal muscle in addition to adipocytes *in vitro* (Pannérec, Formicola et al. 2013). Perivascular PW1+ cells in the mouse lung were shown to express progenitor and pericyte markers, they undergo proliferation in response to hypoxia and they contribute to VSMC formation during vascular remodeling (Dierick, Hery et al. 2016) (Figure 3). It remains to be established whether the above (and other) populations of perivascular mesenchymal cells overlap and whether they converge on a common primed VSMC cell that is recruited to the tunica media and undergoes myogenic differentiation during vascular remodeling.

GLI1+ cells

Glioma-associated oncogene homolog 1 (GLI1) expression has been reported to identify perivascular MSC-like cells in multiple organs (Kramann, Schneider et al. 2015, El Agha, Moiseenko et al. 2017) (Figure 3). These cells are capable of trilineage differentiation and are thus termed MSC-like cells. GLI1+ cells are believed to constitute a subset of PDGFRβ+ pericytes, and they give rise to myofibroblasts in multiple models of fibrosis, particularly in the heart, lungs, kidneys, liver, and bone marrow (Kramann, Schneider et al. 2015, Schneider, Mullally et al. 2018). Genetic ablation of these cells attenuates fibrosis in the heart and kidneys, and their pharmacological targeting attenuates bone marrow fibrosis (Kramann, Schneider et al. 2015, Schneider, Mullally et al. 2018). Interestingly, GLI1+ cells have been shown to contribute to VSMC-like cells in the model of wire injury to the femoral artery (Kramann, Goettsch et al. 2016). Adventitial GLI1+ cells displayed increased proliferation, migrated into the medial and neointimal layers, and co-expressed ACTA2 and Calponin (Kramann, Goettsch et al. 2016). Last but not least, the same study showed that these cells are also progenitors for osteoblast-like cells during medial and intimal calcification in chronic kidney disease in mice (Kramann, Goettsch et al. 2016).

Lineage-tracing studies have shown that during lung development, GLI1+ cells represent a population of mesenchymal progenitors (Li, Li et al. 2015, Moiseenko, Kheirollahi et al. 2017). These cells give rise to airway SMCs and VSMCs, in addition to less characterized populations of alveolar fibroblasts. It is therefore plausible that this population of MSC-like cells undergoes reprogramming during remodeling of the pulmonary vasculature, giving rise to VSMCs (Figure 3).

Animal models of pulmonary hypertension

Exposure of mice to chronic hypoxia is the most commonly used animal model, termed a classic model, to study the pathogenesis of PH. structural change in the vasculature is the essential characteristic in this model. Muscularization of previously non-macular arteries distal blood vessels associated with increased alpha-smooth muscle actin (α-SMA) occurs. In this model, the thickening of distal arterioles is mainly found in the medial layer. In addition, it was found that proliferation and fibrosis in the adventitial layer of proximal arterioles occur (Stenmark, Meyrick et al. 2009). It has been shown that exposure of mice to cigarette smoke for up to 8 months also induces PH development (Seimetz, Parajuli et al. 2011). in the first three months, cigarette smoke exposure caused right ventricular systolic pressure increase followed by right-heart hypertrophy.

Fibroblast growth factor 10 (FGF10)

The fibroblast growth factor family consists of 22 members. FGF10 belongs to the paracrine FGF subgroup. It is a key gene during organogenesis. It has been shown that FGF10 contributes to the formation of the white adipose tissue, the associated mammary gland, heart, liver, brain, kidney, prostate, cecum, ocular, and salivary glands thymus, inner ear, tongue, and trachea (Itoh and Ohta 2014). Fgf10 expression is detected in the developing lung at the onset of the pseudo glandular stage (embryonic day E9.5-E16.5), as early as E10, when the primary bronchi are formed. It plays an essential role in regulating branching morphogenesis (Jones, Chong et al. 2020).

FGF10 regulates mesenchymal cell differentiation in the lung

It has been demonstrated that *Fgf10* hypomorphic embryos (displaying around 20% of the regular *Fgf10* expression) exhibited significant defects in different mesenchymal cell types(Ramasamy, Mailleux et al. 2007). these cell types include ASMCs, endothelial cells, and alveolar MYFs. As FGF10 acts mainly on the epithelium via the fibroblast growth factor receptor 2b (FGFR2b), some of these defects could be due to impaired epithelial to mesenchymal interactions. However, it was also reported that FGF10 acts directly on the mesenchyme to control the differentiation of LIF progenitors (Al Alam, El Agha et al. 2015). In the following sections, we will delineate what is known about the formation of the different mesenchymal cell lineages in the lung and further develop the function of FGF10 in this context.

Lineage tracing of different mesenchymal lineages during lung development

The secondary heart field (SHF), a cell set contributing progressively to the poles of the elongating heart tube during looping morphogenesis, was recently described as a source of multipotent cardiopulmonary progenitors and is identified and defined by the co-expression of *Wnt2*, *Gli1,* and *Isl1* (Peng, Tian et al. 2013). These cells migrate into the lung and differentiate into vascular and airway SMCs as well as other lineages. Fate-mapping of platelet-derived growth factor receptor beta (PDGFRβ) positive cells showed that VSMCs do not arise from mesothelial but rather from mesenchymal progenitor cells (Greif, Kumar et al. 2012). Two studies using animal models published contradicting results. The first study using the Wilms tumor 1 homolog (*Wt1*) *Cre* transgenic line showed that the mesothelium contains progenitors for vascular but not airway SMCs (Que, Wilm et al. 2008).

FGF10+ cells in the early lung mesenchyme differentiate into multiple lineages

Transgenic reporter line *Mlcv1v-nLacZ-24* (or simply $Fgf10^{lacZ}$) was used to demonstrate that FGF10+ cells serve as progenitors for airway SMCs in the distal lung during early development. These results were validated by using an $Fgf10^{Cre-ERT2}$ knock-in line (El Agha and Bellusci 2014). Lineage labeled FGF10+ cells mainly differentiate into the airway and VSMC and the LIF lineages (El Agha, Herold et al. 2014). However, it is still unclear whether this population of FGF10+

mesenchymal progenitor cells contain unipotent or multipotent progenitor cells. The progeny of FGF10-expressing cells needs to be analyzed using single-cell transcriptomic approaches as well as multi-color *Cre*-reporter mice to better characterize these progenitor cells. During the early pseudoglandular stage, FGF10 itself is not acting on the airway SMCs to control their differentiation. It has been proposed that bone morphogenetic protein 4 (BMP4), which is induced by FGF10 in the distal epithelium, is responsible for their differentiation (Mailleux, Kelly et al. 2005). In addition, it has been shown that *β-Catenin* signaling in the mesenchyme does not contribute to the differentiation of FGF10+ progenitors but rather to their proliferation (De Langhe, Carraro et al. 2008). More recently, *miR-142-3p*, a microRNA that is enriched in the mesenchyme, was reported to target *adenomatous polyposis coli* (*Apc*), a gene encoding a negative regulator of *β-Catenin*.

Upregulated *Apc* expression in the lung mesenchyme upon *miR-142* knockdown using morpholinos leads to the inhibition of mesenchymal proliferation and premature SMC differentiation. The corresponding loss of mesenchymal *β-Catenin* signaling in the mesenchyme was associated with decreased *Fgfr2c* and *Fgf10* expression (Carraro, Shrestha et al. 2014).

Repair supportive role of FGF10+ mesenchymal cells in the lung

FGF10 was secreted by mesenchymal cells residing in distal mesenchyme during lung development, which significantly impacted the adjacent epithelium cells via FGFR2b receptors. It has been shown that the cross-talk between mesenchymal cells and epithelial cells via FGF10/FGFR2b signaling plays an essential role in the development and injury repair process. During early lung development, SHH secreted by epithelium cells could inhibit the expression of *Fgf10* via GLI1 in mesenchymal cells. During the adult stage, SHH was reported to maintain epithelium cell quiescence. Additionally, the Inactivation of *Shh* promoted the proliferation of mesenchymal cells. One of our recent studies demonstrated that a group of PDGFRα+ mesenchymal cells also express FGF10. These cells have a supportive repair role of bronchial epithelium following acute lung injury caused by naphthalene. GLI1 has been the newly defined mesenchymal cell marker in recent years. Therefore, we speculate that a similar repair process is occurring during vascular injury and repair process. The GLI1+ cell lineage in vasculature expressed a low level of ACTA2 and was adjacent to the ACTA2+ SMCs. Against this background, we propose that the GLI1+ cells expressing FGF10 are involved in the repair process during the reverse remodeling of PH.

A novel *Fgf10*$^{Cre\text{–}ERT2}$ knock-in mouse line targeting FGF10+ cells postnatally

In the context of the repair process, *Fgf10* deletion in peribronchial mesenchymal cells leads to impaired repair following injury to the bronchial epithelium using naphthalene (Volckaert, Dill et al. 2011, Moiseenko, Vazquez-Armendariz et al. 2020). On the other hand, overexpression of *Fgf10* reduces the severity of lung fibrosis in bleomycin-induced mice (Gupte, Ramasamy et al. 2009). Given these diverse biological activities, it is important to generate and validate a mouse knock-in line to monitor the localization, fate, and status of FGF10+ cells during development, homeostasis and repair after injury. We have previously generated a *Fgf10*$^{Cre\text{–}ERT2}$ knock-in mouse line, called after that *Fgf10*$^{KI\text{–}v1}$ mice, to monitor the fate of FGF10+ cells after tamoxifen (Tam) administration (El Agha, Al Alam et al. 2012). In this line, the Tam-inducible *Cre* recombinase (*Cre-ERT2-IRES-YFP*) was inserted in frame with the start codon of the endogenous *Fgf10* gene. *Fgf10*$^{KI\text{–}v1}$ corresponds to a loss-of-function allele for *Fgf10*, as evidenced by our observation that *Fgf10*$^{KI\text{–}v1/KI\text{–}v1}$ homozygous embryos die at birth from multi-organ agenesis, including the lung. In the *Fgf10*$^{KI\text{–}v1/+}$ lungs, the expression of *Cre* gradually decreases to almost undetectable levels postnatally, rendering the monitoring of FGF10+ cells postnatally impossible. This is likely due to the deletion of intronic sequences containing key transcription factor binding sites at the insertion site of the *Cre*-expression cassette. To circumvent this problem, we, therefore, generated a new *Cre-ERT2* knock-in line (named *Fgf10*$^{KI\text{–}v2}$) by targeting the 3′UTR of the endogenous *Fgf10* gene.

Material and Methods

Animal experiments

All animals were housed under specific pathogen-free (SPF) conditions with free access to food and water. *Gli1*$^{Cre\text{-}ERT2}$ (stock_ Gli1tm3 (cre/ERT2) Alj/J)) mice were purchased from Jackson Laboratory (stock number 007913). In this transgenic line, *Cre-ERT2* coding sequence was inserted at the start codon of *Gli1* in a mouse bacterial artificial chromosome (BAC). *Cre* reporter line *tdTomato*^{flox} mice were purchased from Jackson Laboratory (B6; 129S6-Gt (ROSA) 26Sortm9 (CAG−tdTomato) Hze/J, ref 007905). Tandem dimer Tomato (tdTomatoflox) and membrane-targeted tdTomato/membrane-targeted green fluorescent protein (mT/mG) Cre-reporter mice were purchased from the Jackson laboratory.

Animal experimentation approval

All Animal experiments were approved by the Regierungspraesidium Giessen (approval number RP GI20/10-Nr. G47/2019; RP G120/10-Nr. G06/2017 and G67/2019).

Tamoxifen administration

For PH project, *Gli1*$^{Cre\text{-}ERT2}$ mice (8-12 weeks) were fed with tamoxifen food (400mg/kg) for 7 days. For genetic cell ablation, *Gli1*$^{Cre\text{-}ERT2}$; *iDTR*^{flox} mice (8-24 weeks old) were fed with either tamoxifen containing food (400mg/kg) for 7 days or injected intraperitoneally 5 times with tamoxifen dissolved in corn oil at a dose of 0.1 mg/g of body weight. Tamoxifen stock solution was prepared by dissolving tamoxifen powder (Sigma-Aldrich, T5648-5G) in corn oil at a concentration of 20 mg/mL at room temperature and stored in −20°C. For validation project, *Fgf10*$^{Ki\text{-}v2}$ pregnant mice received a single i.p. injection of tamoxifen (0.1 mg/g body weight) and pups also received a single subcutaneous injection of tamoxifen (0.2 mg/pup). Embryonic day 0.5 (E0.5) was assigned to the day when a vaginal plug was detected.

Hypoxia and smoked-induced PH

For hypoxia-induced PH, *Gli1*^{CreERT2} (8 to 12 weeks old) mice were sent to the hypoxia (10% of O_2) or normoxia (21% of O_2) chamber for 28 days following tamoxifen administration. Lung samples were collected for future analysis by the of treatment. For smoke-induced PH, *Gli1*$^{Cre\text{-}ERT2}$ (8 to 12 weeks old) mice were exposed to cigarette smoke or room air 8 hours per day for 8 months after tamoxifen administration. Lung samples were collected after 8 months of cigarette smoke or room air exposure.

L-NIL treatment

Gli1$^{Cre\text{-}ERT2}$ mice were fed with L-NIL (iNOS inhibitor) containing water (N6-(1-Iminoethyl)-L-lysine dihydrochloride) (Biotium, Hayward, CA, USA) at a concentration of 2.8 mM for 3 months. Lung samples were collected and analyzed after 3 months of L-NIL treatment.

Diphtheria toxin (DT) administration

For cell ablation experiments, *Gli1*$^{Cre\text{-}ERT2}$*; tdTomato*^{flox}; *iDTR*$^{\text{flox}}$ mice (8-24 weeks old) were injected intraperitoneally 3 times with DT (100ng/mice/i.p.) (Sigma) dissolved in PBS (List Biological Laboratories) at the begining of the hypoixa treatment.

RNA extraction and quantitative Real-Time PCR

RNA extraction from flow cytometry sorted cells was performed using RNeasy plus Micro kit (Qiagen). Freshly isolated embryos and lung samples were lysed and homogenized using QiaShredder columns (Qiagen), and RNA was extracted using RNeasy kit (74106, Qiagen, Hilden, Germany). Primers and probes were designed using NCBI Primer-BLAST. More details about the used primers and probes can be found in Table 1. Quantitative real-time PCR (qPCR) was performed using Light Cycler 480 real-time PCR machine (Roche Applied Science). Samples were run in doublets using *B2M* as a reference gene. The delta-delta Ct method was used to calculate the relative fold change of gene expression. GraphPad Prism 7.0 software was used to generate and analyze data. Statistical analyses were performed using either Student's t-test (for comparing two groups) or One-way ANOVA (for comparing three or more groups). Data were considered significant if $P < 0.05$.

Table 1. Primer sequences for qPCR

Gene name	Primer Sequence
iDTR (HB-EGF)	Forward **5’-** GGAGCACGGGAAAAGAAAG**-3’** Reverse **5’-** GAGCCCGGAGCTCCTTCACA**-3’**
Gli1	Forward **5’-**TGG AGG TCT GCG TGG TAG A**-3’** Reverse **5’-** TTG AAC ATG GCG TCT CAG G**-3’**
Acta2	Forward **5’-**ACT CTC TTC CAG CCA TCT TTC A**-3’** Reverse **5’-** ATA GGT GGT TTC GTG GAT GC**-3’**
Ccnd1	Forward **5’-**AGT GTG ACC CGG ACT GC **-3’** Reverse **5’-** GAT GTC CAC ATC TCG CAC G**-3’**
Shh	Forward **5’-**CCA ATT ACA ACC CCG AC TC**-3’** Reverse **5’-** GCA TTT AAC TTG TCT TTG CA**-3’**
Pdgfrb	Forward **5’-**AGT GGT CCT TAC CGT CAT CT**-3’** Reverse **5’-** CAT CGG ATV TCA TAG CGT GG**-3’**
B2m	Forward **5’-**CTC ACA CTG AAT TCA CCC CC**-3’** Reverse **5’-** GCT TAA CTC TGC AGG CGT AT**-3’**
Gli2	Forward **5’-**CCG TGG ATG TGT TCA TTG TT**-3’** Reverse **5’-** GCA GAC TGC ACC AAG GAG TA**-3’**
Gli3	Forward **5’-**GCT GAG AAG CCC ATG ACA TC**-3’** Reverse **5’-** GTT GCT GAT GGG GGA CTG**-3’**
Smo	Forward **5’-**GCA AGC TCG TGC TCT GGT**-3’** Reverse **5’-** GGG CAT GTA GAC AGC ACA CA**-3’**

Patch1	Forward **5’**-TGT GAA CCT CAC GGT CAG C**-3’** Reverse **5’-** AAC TTC GCT CTC AGC CAC AG**-3’**
Cre	Forward **5’**-CGCAAGAACCTGATGGACATG**-3’** Reverse **5’**-ACCGGCAAACGGACAGAA**-3’**

Flow Cytometry

Freshly dissected lung samples were washed with Hanks’ balanced salt solution (HBSS, 14175-095, Thermo Fisher), and then cut into small pieces using a sharp blade and digested with 0.5% collagenase Type IV in HBSS (17104019, Life Technologies, Invitrogen) at 37°C for 45 min. Lung homogenates were then passed through 18, 21, and 24G needles and then through 70 and 40 µm cell strainers (542070 and 542040, Greiner Bio-one International). Lung homogenates were centrifuged at 1000rpm at 4°C for 10 min. Cell pellets were then re-suspended in HBSS containing different antibodies. Single cell suspensions obtained from *Gli1*$^{Cre\text{-}ERT2}$ mice were incubated with anti-EpCAM (APC-Cy7-conjugated, 1:100), anti-CD31 (Pacific Blue-conjugated, 1:100) and anti-CD45 (Pacific Blue-conjugated, 1:100) antibodies (all from Biolegend) for 20 min on ice in the dark. Single cell suspensions obtained from *Fgf10*$^{Ki\text{-}v1}$ and *Fgf10*$^{Ki\text{-}v2}$ were incubated with antibodies against CD45 (103114, APC-conjugated; 1:50), CD31 (102409, APC-conjugated; 1:50), EPCAM (APC-Cy7-conjugated; 1:50) and SCA1 (108120, Pacific blue-conjugated; 1:50) (all from Biolegend) as well as LipidTOX stain (FITC-conjugated, 1:200) (H34350, Life Technologies, Invitrogen) for 30 min on ice in the dark. 20 µL single cell suspensions were taken before staining as an unstained control. Samples were then washed with 1 mL of HBSS at 4°C for 5 min. FACSAria III cell sorter (BD Biosciences) was used to carry out the FACS measurements and sorting. Endogenous tdTomato signal was detected through the PE channel. Gates were set up according to the unstained controls.

Bioinformatics

NCBI genes were used to find the mouse murine *Fgf10* sequence and the identification of putative transcription factor binding sites (TFBS) was done using PROMO software2. The list of putative TFBS located in the area including exon 3 and 30UTR was further compared with previously identified transcription factors expressed in the lung mesenchyme (Herriges, Yi et al. 2012).

Precision-cut lung slices

Mice were anesthetized with isoflurane (Baxter) and subsequently perfused via the left ventricle with 4°C PBS for 1 minute. Then lungs were infiltrated with 1.7% low melting point agarose via the trachea. Keep the lungs on ice for 15 minutes. For immunofluorescence and histology studies, lungs were fixed in 4% paraformaldehyde in PBS at 4°C overnight. Wash 3 times in PBST, each time 15 minutes. Lungs were cut into 200 µm slices using a vibratome (Leica).

Genotyping

Biopsies taken from mice were collected and then digested in 200 µl Viagen, including 1 µl proteinase K at 55 °C on a shaker overnight. The reaction is stopped by placing the biopsies in the shaker at 85 °C for 40 minutes. For protocol and primer sequences, please see Table 1. PCR products were analyzed using a 1,5 % agarose gel containing TAE buffer with SYBR safe (50 µl SYBR safe + 500 mL 1x TAE buffer). 10 µl of PCR products were loaded with 2 µl loading dye (Biorad Nucleic Acid Sample loading buffer, 5x), and then the gel was run at 120V for 30-45 min. A molecular ladder (QX Size Marker, 100-2.5kb, Qiagen) was used to detect the expected band sizes (Table 2).

Table 2. Primer sequences and protocols for genotyping

Mouse line	Primer sequences	PCR Protocol		
		Step	**Temp (°C)**	**Time**
Fgf10$^{Ki–v2}$	Mutant allele: 1) AAC ACC TCT GCT CAC TTC CTC 2) ATG TGA GCG AGT AAC AAC CCG TCG GAT TCT WT allele: 3) GCA GGC AAA TGT ATG TGG CA 4) TGC TTG CGT GTC TTA CTG CT	1	94	3 min
		2	94	30 sec
		3	60	30 sec
		4	72	1 min Repeat 2-4 33x (34 total)
		5	72	5 min
		6	12	Hold
Gli1$^{Cre\text{-}ERT2}$	1) GCG GTC TGG CAG TAA AAA CTA TC 2) GTG AAA CAG TGC TGT CAC TT 3) GGG ATC TGT GCC TGA AAC TG 4) CTT GTG GTG GAG TCA TTG GA	1	94	3 min
		2	94	30 sec
		3	51.7	1 min
		4	72	1 min Repeat 2-4 33x (34 total)
		5	72	2 min
		6	4	Hold
iDTR^{flox}	1) GGC TAC TGC TGA CTA TCA ACA TT 2) TCA TGG TGG CGA ATT CGA T	1	95	3 min
		2	95	30 sec
		3	59	30 sec
		4	72	1 min Repeat 2-4 33x (34 total)
		5	72	2 min
		6	10	Hold
tdTomato^{flox}	1) CTG TTC CTG TAC GGC ATG G	1	94	3 min
		2	94	20 sec

	2) GGC ATT AAA GCA GCG TAT CC 3) CCG AAA ATC TGT GGG AAG TC 4) AAG GGA GCT GCA GTG GAG TA	3	61	30 sec
		4	72	30 sec Repeat 2-4 33x (34 total)
		5	72	2 min
		6	4	Hold

Table 3. Expected band size of genotyping products.

Mouse line	Expected band size (WT)	Expected band size (mutant)
Fgf10$^{Ki\text{-}v1}$	-	349bp
Fgf10$^{Ki\text{-}v2}$	580bp	252bp
Gli1$^{Cre\text{-}ERT2}$	136bp	204bp
tdTomato^{flox}	297bp	196bp

PCLS staining

200 µm-thick PCLS were fixed with 4% PFA overnight and washed with PBST (three times, 30 min each) and then stored in PBS containing 0.02% sodium azide. Fixed PCLS were blocked with 3% BSA in PBS for 2 hours at RT, stained with mouse FITC-conjugated anti-alpha smooth muscle actin antibody (Sigma, 1:200) and CD31(Invitrogen 1:200) (overnight at 4°C) and washed with PBS (three times, 30 min each). HCS LipidTOX red neutral lipid dye (Invitrogen, 1:200) and Hoechst (1:5000) were added for 3 hours at RT. After washing, PCLS were placed in glass-bottomed 4-well micro slides (Ibidi) containing PBS and imaged by confocal microscopy (Leica TCS SP5).

Paraffin block preparation

Mouse lung tissues were fixed using 4% PFA followed by embedding in paraffin. Paraffin blocks were sectioned into 5 µm-thick slices and placed on glass slides. Following deparaffinization, lung sections were stained with hematoxylin (Roth) for 2 min, washed with running tap water for 10 min, and then stained with eosin (Thermo Fisher Scientific) for 2 min.

Deparaffinization

Slides will be placed in the jars with specified reagents in the following orders.

- Xylol (6 minutes)
- Xylol (6 minutes)
- 100% Ethanol (2 minutes)
- 100% Ethanol (2 minutes)
- 95% Ethanol (2 minutes)
- 70 % Ethanol (2 minutes)
- 50% Ethanol (2 minutes)
- 30% Ethanol (2 minutes)
- Deionized water (2 minutes)

IMARIS-based quantification

IMARIS provides functionality for the visualization, segmentation, and interpretation of 3D confocal images. 3D confocal images generated from PCLS were imported into the software and then analyzed. Different fluorescent signal was picked up by the software automatically. The nucleus was stained with DPAI in blue. VSMCs were stained with anti-alpha smooth muscle actin antibody, where is in green. Endothelial cells were stained with anti-CD31 antibodies, which are in grey. Lineage labeled GLI1+ cells were labeled by tdTomato, which is in red. The DAPI signal was picked up by the software using dot selection mode. Every dot with a diameter equal to or above 6 µm was counted. tdTomato and ACTA2 signals were measured by the software using surface selection mode. DAPI+ dots, which are also positive for tdTomato or ACTA2 signals, were counted in the analysis.

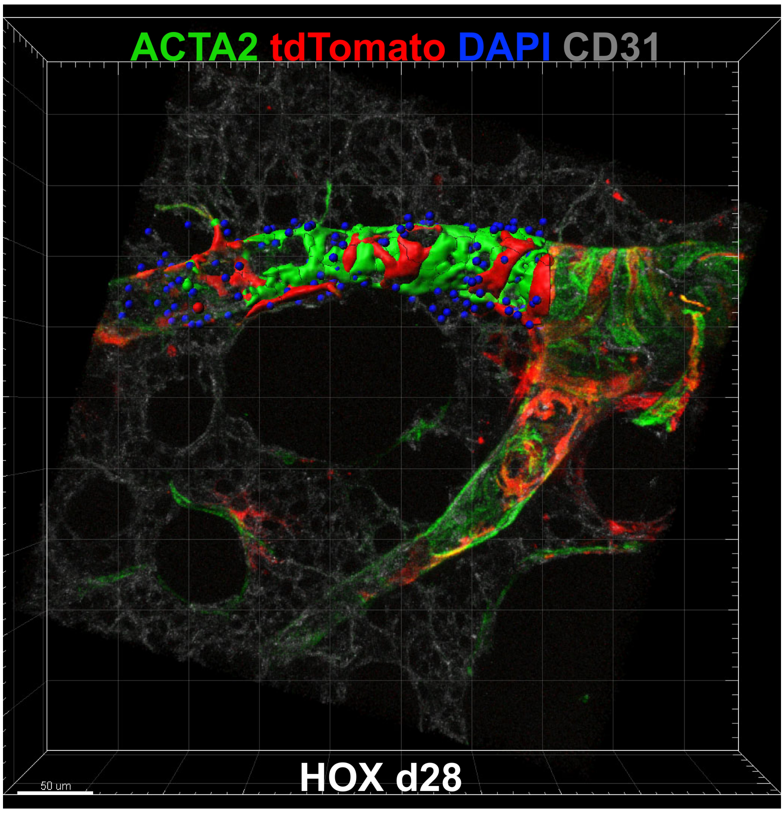

Figure 4. IMARIS-based quantification. 3D confocal image of HOX d28 mice PCLS. ACTA2 staining for smooth muscle cells in green, tdTomato labeled for GLI1+ cells in red, CD31 staining for endothelial cells in grey. DAPI staining for nucleus in blue.

Statistical analysis

Statistical analyses and graph assembly were carried out using GraphPad Prism 7 (GraphPad Prism Software). To assess the normal distribution of data sets, the D’Agostino Pearson normality test was applied. In the case of normal distribution, Student’s t-test (unpaired, two-tailed) was utilized to compare the means of two groups, while one-way ANOVA (with post-hoc tests) was used to compare the means of three or more groups. In the cases where data were not normally distributed, respective non-parametric tests were applied (Mann-Whitney test to compare the means of two groups and Kruskal-Wallis test to compare the means of three or more groups). Data are presented as mean ± SEM. The number of biological samples (n) for each group and the utilized statistical tests are stated in the corresponding figure legends. Differences in means were considered statistically significant if $P<0.05$.

Objectives

Pulmonary arteriole hypertension (PAH) is a lethal disease with unclear causes. The hallmark of pulmonary hypertension is pulmonary vascular remodeling During the process of vascular remodeling, the wall of blood vessels thickened. The compliance of blood vessels also decreased significantly. These changes are mainly caused by the overgrowth of the vascular smooth muscle cells in the tunica media layer and myofibroblast in the tunica adventitia layer. In this study, we used two injury models: hypoxia and smoke-induced, to study the pathogenesis of PAH. Given Sheikh et al.'s recent cell lineage studies, the proliferated ACTA2+ cells in tunica media and newly formed ACTA2+ cells in distal arterioles arise from pre-existing SMCs (Sheikh, Lighthouse et al. 2014). However, we provide evidence that the origin of newly formed ACTA2+ cells in distal arterioles is not solely from pre-existing VSMCs. More studies have shown that other cell types could contribute to disease-related ACTA2+ cells, such as endothelial cells, mesenchymal cells, and pericytes. One recent study from *Kramman et al.* validated that GLI1 is a marker of mesenchymal stem cells, allowing further investigation of their role in the disease and repair process (Kramann, Schneider et al. 2015). Lineage tracing studies showed that GLI1+ cells are progenitors of vascular smooth muscle cells and contribute to neointima formation following acute vasculature injury. Therefore, we hypothesize that GLI1+ cells could be one of the origins of newly formed ACTA2+ cells in pulmonary vascular remodeling occurring in PH.

Objective 1: To determine if GLI1+ cells contribute to VSMCs in hypoxia and smoke-induced PH

Objective 2: To determine if GLI1+ cells are functionally involved in the pathogenesis of PH

Objective 3: To apply single-cell sequencing analysis on GLI1 cells during hypoxia-induced PH

FGF10 is secreted from mesenchymal cells that reside in the distal lung mesenchyme during the pseudoglandular stage from embryonic day 9.5 to embryonic day 13.5. Our previous study has shown that FGF10+ cells are progenitors of the airway and vascular smooth muscle cells. We demonstrated that a group of *Pdgfr* α + mesenchymal cell populations emerged upon acute epithelium injury caused by naphthalene. Interestingly, these cells also expressed FGF10 to support the repair of the bronchial epithelium. Combining all the findings, it is rational to check if these GLI1+ lineage labelled cells could also secrete FGF10 upon vascular injury in PH. To lineage trace the FGF10+ cells in the adult stage, we have introduced a novel $Fgf10^{Cre\text{–}ERT2}$ knock-in mouse line.

Objective 4: To validate a novel $Fgf10^{Cre\text{–}ERT2}$ knock-in mouse line.

Results

Objective 1: origin and fate of vascular smooth muscle cells in hypoxia-induced pulmonary hypertension

Altered sonic hedgehog (SHH) signaling in hypoxic lungs

We performed during vascular remodeling and reverse remodeling the analysis of gene expression using quantitative PCR. In our experimental conditions, vascular remodeling was triggered by HOX treatment for 28 days (Fig. 5A). In particular, IF for ACTA2 on PCLS from NOX and HOX at day 28 indicated the presence of muscularization of the distal arterioles which is a hallmark of pulmonary hypertension. Reverse vascular remodeling was made by re-exposure to NOX treatment for another 30 days. Next, we examined the expression of genes linked to Glioma-associated oncogene 1 (*Gli1*), in particular *Shh* and *Smoothened* (a gene encoding a G protein-coupled receptor) (Fig. 5B). We performed during vascular remodeling and reverse remodeling the analysis of the expression of *Shh*, *Gli1,* and *Smo* using quantitative PCR (Fig. 5C-E). Lung samples were collected at different time points to check the expression of relevant genes from the lung homogenate (n=3 at each time point and each condition). *Shh* expression in HOX and NOX was not significantly different at all the time points considered except for day 44, during reverse remodeling (P=0.058). *Gli1* expression was upregulated in HOX vs. NOX at day 3 during vascular remodeling P=0.034. As for *Shh*, we also find *Gli1* to be up-regulated at day 44 during reverse remodeling (P=0.259). *Smo* expression trended towards a downregulation at day 28 and was then found to be upregulated at d44 and 51 during reverse remodeling (P=0.0402, P=0.0206, respectively).

Altogether the results indicate that genes involved in the SHH signaling pathway were altered during both vascular remodeling and reverse remodeling suggesting that GLI1+ cells may play a functional role in HOX-induced PH in mice.

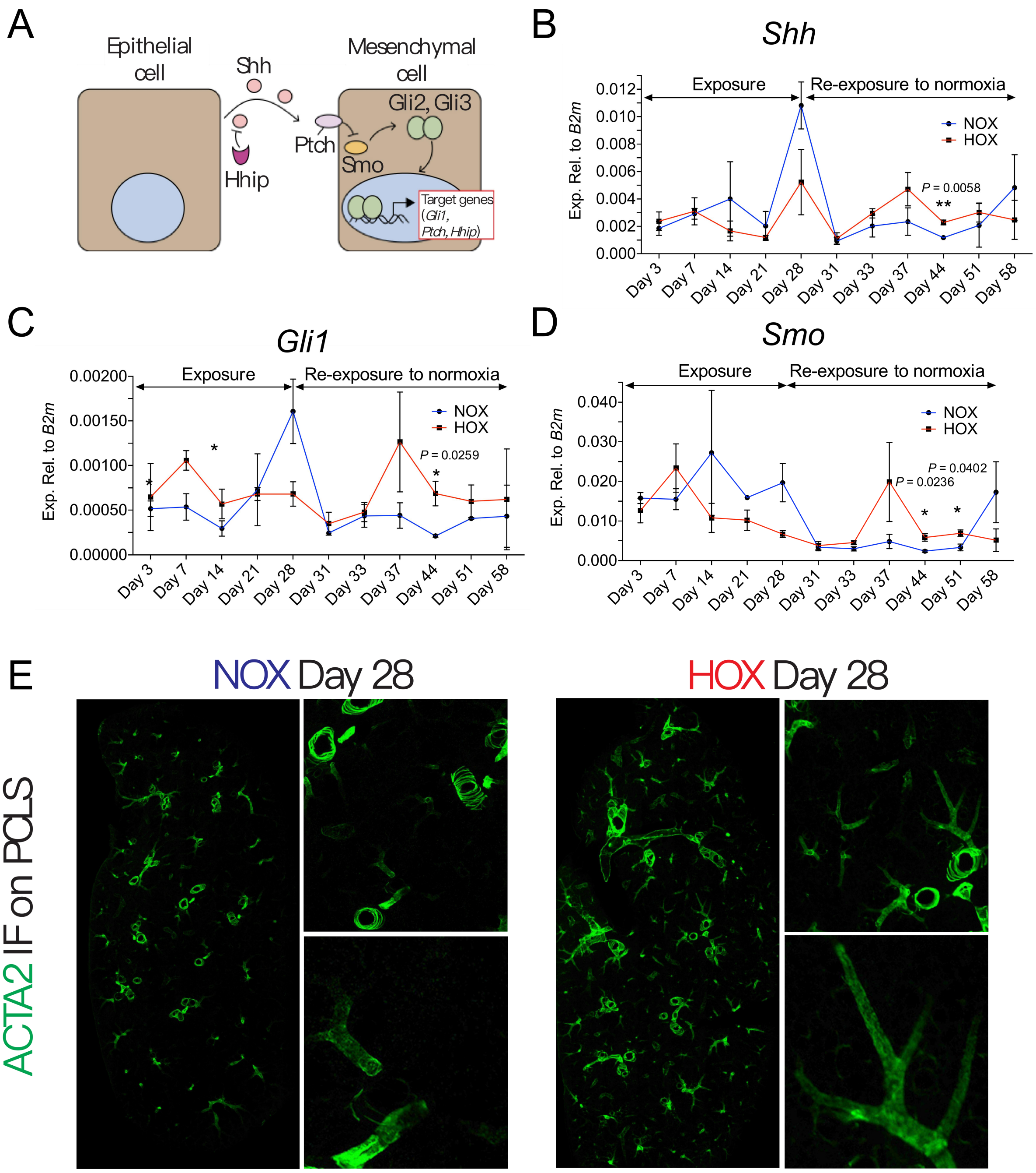

Figure 5. Evidence for dysregulation of the *Sonic hedgehog (Shh)* pathway during vascular remodeling and reverse remodeling after hypoxia injury in mice. A. Schematic of the Shh pathway. **B-D**. Expression of *Shh*, *Gli1,* and *Smo* in lung homogenates from WT animals during vascular remodeling (HOX, Day 3-28) and reverse remodeling (HOX+NOX, Day 28-58) at different time points (n=3 at each time point and each condition). NOX-exposed WT animals at each time point were used as controls. **E**. IF for ACTA2 on PCLS generated from HOX and NOX at Day 28.

Validation of hypoxia-induced PH in *Gli1^{CreERT}; tdTomato^{flox}* mice

In order to lineage-trace GLI1+ cells, we generated *Gli1^{CreERT2}; tdTomato^{flox}* mice. Upon tamoxifen food administration, GLI1+ cells are permanently labeled and can be monitored in the context of NOX, HOX, and HOX+NOX (Fig. 6A) allowing us to study the fate of GLI1+ cells during vascular remodeling and reverse remodeling. Hypoxia exposure of adult mice is one of the most commonly used models to study PH. To validate the development of PH caused by hypoxia exposure in our *Gli1^{CreERT2}; tdTomato^{flox}* mice, hemodynamic measurements on experimental mice were performed in experimental group (HOX) and control group (NOX) after 28 days of treatment as well as in re-exposure group (HOX+NOX) at day 56 (Fig. 6B). We first quantified the ratio of the right ventricular (RV) and the left ventricular plus septum (LV+S) mass as an indicator of right heart hypertrophy, which is one of the most significant characteristics of PH. The right ventricular systolic pressure was also measured to confirm the injury (Fig. 6B). The hemodynamic results clearly indicate PH development in our experimental conditions as well as in the re-exporsure group (reverse remodeling phase).

Quantification of the GLI1+ cells by Fluorescence-active cell-sorting (FACS).

Next, we used flow cytometry to quantify the abundance of lineage-labeled GLI1+ cells during vascular remodeling and reverse remodeling: NOX, HOX, and HOX+NOX. Right lungs obtained from *Gli1^{CreERT2}; tdTomato^{flox}* mice were used to carry out FACS. As it has been shown that GLI1+ cells are negative for the endothelial marker CD31 and hematopoietic lineage marker CD45, we excluded the CD31+ and CD45+ cells while sorting (tdTom+) GLI1+ cells. Also, because the GLI1+ lineage is being studied as a group of mesenchymal cells, we have excluded the epithelial cells (EPCAM+). GLI1+ cells and ACTA2+ cells in freshly dissected lungs obtained from *Gli1^{CreERT2}; tdTomato^{flox}* mice out of the CD45, CD31 and EPCAM negative population (representing the lung resident mesenchymal cells or rMC) were sorted and analyzed by flow cytometry (Fig 6C).

We first compared the HOX vs. NOX conditions (Fig. 6D). The percentile of ACTA2+ cells out of the rMC, showed a significant increase in HOX compared to NOX (HOX: 17.0% ± 1,2%, n=7 vs. NOX: 6.5% ± 1,5%, n=7) confirming the hemodynamic data that our model of hypoxia-induced pulmonary hypertension is functional with a quantifiable increase in vasculature remodeling. Interestingly, no significant change in the number of GLI1+ cells was detected between NOX and HOX (NOX: 29.3% ± 2.8%, n=7 vs. HOX: 31.2% ± 4.4%, n=7) suggesting that GLI1+ cells are not amplified following injury. Then, we checked the percentile of ACTA2+GLI1+ cells arising from GLI1+ cell population. We found a significant increase in HOX vs. NOX in the percentile of ACTA2+GLI1+ out of the GLI1+ cell population (HOX: 12,21 % ± 0.7774%, n=7 vs. NOX: 2.836% ± 1.626%, n=6) indicating that GLI1+ cells acquire ACTA2 expression during vascular remodeling. Finally, we also quantified the percentile of ACTA2+GLI1+ out of the ACTA2+. We found an increase in this ratio for HOX vs. NOX (HOX: 29.16 % ± 2.862%, n=7 vs. NOX: 13.26% ± 2.142%, n=6) confirming that GLI1+ cells greatly contribute to the ACTA2+ pool following injury.

Next, we compared lineage labeled cells during vascular reverse remodeling phase (HOX+NOX) vs. vascular remodeling phase (HOX) (Fig. 6D). The percentile of ACTA2+ cells out of the rMC, showed a significant decrease in reverse remodeling phase (HOX+NOX: 11.8 % ± 0.5329%, n=5) compared to remodeling phase (HOX: 16.97% ± 1.232%, n=7) confirming the hemodynamic data that our model of hypoxia-induced PH is reversible by returning of the mice to normoxia condition. Of note, the rescue is not complete as the %ACTA2+/rMC in reverse remodeling (HOX+NOX: 11,80% ± 0,5329%, n=5) is still higher compared to normoxia condition (NOX: 6.490% ± 1.488%, n=7). There is no significant change of GLI1+ cells between HOX and HOX+NOX (HOX: 31.23 % ± 4.407%, n=7 vs. HOX+NOX: 28.42% ± 1.683%, n=5) suggesting that lineage-labeled GLI1+ cells are not cleared during reverse remodeling. Then, we checked the percentile of ACTA2+GLI1+ double positive cells arising from GLI1+ cell population. We found a significant decrease in HOX +NOX vs. HOX (HOX+NOX: 6.626 % ± 0.4921%, n=5 vs. NOX: 12.21% ± 0.7774%, n=7) indicating that GLI1+ cells lose ACTA2 expression during reverse remodeling. Finally, we also quantified the percentile of ACTA2+GLI1+ out of the ACTA2+. We found a decrease in this ratio for HOX +NOX vs. HOX (HOX+NOX: 16.70 % ± 3.748%, n=5 vs. HOX: 29.16% ± 2.862%, n=7) confirming that the lack of contribution of the GLI1+ cells to the ACTA2+ pool during reverse remodeling. Besides the perivascular sites, tdTomato+ cells could also be found around the airway and parenchyma space in the blood vessels at homeostasis.

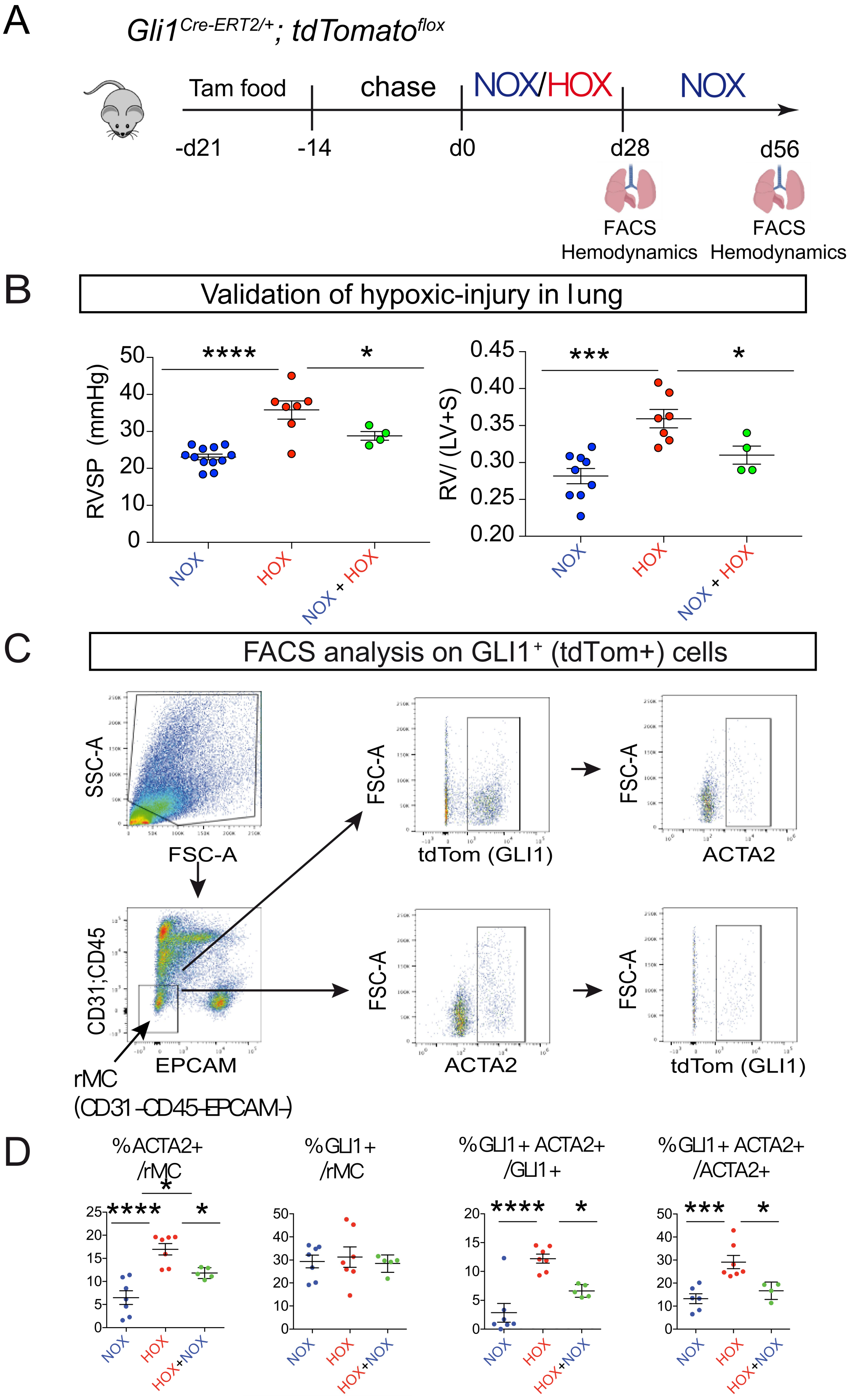

Figure 6. Validation of hypoxia injury in *Gli1$^{CreERT2/+}$*; *tdTomato^{flox}* mice by hemodynamics and flow cytometry. A. Experimental set up for hypoxic injury using the *Gli1$^{CreERT2/+}$; tdTomato^{flox}* mice. **B.** Hemodynamic measurements of NOX and HOX exposed animals at day 28. **C.** FACS strategy to isolate GLI1+ (tdTomato+) cells. **D.** Corresponding quantification of FACS.

GLI1+ cells quantified on PCLS by IMARIS-based 3D rendering indicate that GLI1+ cells give rise to newly formed ACTA2+ cells in proximal and distal blood vessels upon hypoxia exposure

Next, we introduced the cutting-edge quantification software IMARIS to confirm the flow cytometry data above by determining whether GLI1+ cells give rise to ACTA2+ cells in the arterioles (Fig. 7). Tamoxifen food were fed to *Gli1$^{Cre-ERT2}$; tdTomoto^{flox}* mice to induce the labeling of GLI1+ cells before injury. Two weeks of chase time was allowed to clean up the tamoxifen in the system. Normoxia or hypoxia exposure were applied to *Gli1$^{Cre-ERT2}$; tdTomoto^{flox}* mice for 28 days. For investigation in reverse remodeling phase, 28 days hypoxia-treated mice were sent to normoxia chamber for another 28 days. 200 μm thick PCLS were prepared by vibratome and stained for DAPI in blue, ACTA2 in green and CD31 in grey. 3D Confocal images were then taken and maximum projection pictures were processed through the IMARIS software to get high resolution 3D rendering of the structure of arterioles. CD31 signal served to delineate the blood vessel and DAPI was used to distinguish individual cells.

We separated the blood vessels into two groups: distal arterioles (blood vessel diameter smaller than 25 µm) and proximal arterioles (blood vessel diameter greater than 26 µm). Although PH formation in the HOX model was suggested by the hemodynamic measurements and the FACS approach, IMARIS-based quantification and analysis of ACTA2+ cells in the blood vessel wall provide a better validation that this pathological process occurred. First, we compared HOX with NOX and we quantified the ACTA2+, GLI1+ and ACTA2+GLI1+ cells in the distal arterioles. Each dot on the graphs displayed in Fig. 7N represents one blood vessel (10-30 blood vessels total per condition, 5-7 blood vessels per animal, n= 3-5 per condition).

We observed an increase in the percentile of ACTA2+ cells in HOX vs. NOX in the distal arterioles (HOX: 14,73% ± 2,293%, n=4 vs. NOX: 0,3369% ± 0,2058%, n=4). A similar increase was observed for GLI1+ cells in distal arterioles (HOX: 11,17 % ± 1,492 %, n=4 vs. NOX: 1,437 % ± 0,4309 %, n=4) as well as GLI1+ACTA2+ double positive cells out of GLI1+ cell population (HOX: 56,58% ± 6,230%, n=4 vs. NOX: 0% ± 0%, n=4) and GLI1+ACTA2+ double positive cells out of ACTA2+ cell population in the distal arterioles (HOX: 47,99 % ± 5,598 %, n=4 vs. NOX: 0% ± 0%, n=4). These data are validating the flow cytometry results (Fig. 6) and confirm that GLI1+ cells contribute to half of the newly formed ACTA2+ cells in the small arterioles upon HOX exposure. Finally, we quantified the ACTA2+, GLI1+ and ACTA2+GLI1+ cells in the proximal arterioles in HOX vs. NOX. Our results mimic what is seen for the small arterioles.

GLI1+ cells quantified on PCLS by IMARIS-based 3D rendering indicate a decreased contribution of GLI1+ cells in the blood vessels during reverse remodeling

Next, we compared lineage labeled cell population in reverse remodeling phase (HOX+NOX) with remodeling phase (HOX). We have quantified the ACTA2+, GLI1+ and ACTA2+GLI1+ cells in the small arterioles. We observed an decrease in the percentile of ACTA2+ cells in HOX+NOX vs. HOX in distal arterioles (HOX+NOX: 0,7524 % ± 2,293 %, n=4 vs. HOX: 14,73 % ± 2,293 %, n=4). A similar decrease was observed for GLI1+ cells (HOX+NOX: 1,024 % ± 0,3734 %, n=4 vs. NOX: 11,17 % ± 1,492 %, n=4) as well as for GLI1+ACTA2+ out of GLI1+ (HOX+NOX: 6,964 % ± 4,876 %, n=4 vs. HOX: 56,58 % ± 6,230 %, n=4) and GLI1+ACTA2+ out of ACTA2+ (HOX+NOX: 15,45 % ± 8,019 %, n=4 vs. HOX: 47,99 % ± 5,598 %, n=4). These data are validating the flow cytometry results (Fig. 7) and suggest that GLI1+ cells are causative for the PH phenotype.

Next, we quantified the ACTA2+, GLI1+ and ACTA2+GLIt1+ cells in the proximal arterioles in HOX+NOX with HOX. Our results are quasi-identical to what is seen for the small arterioles. In addition, the reverse remodeling process seems to occur more efficiently in the distal arterioles.

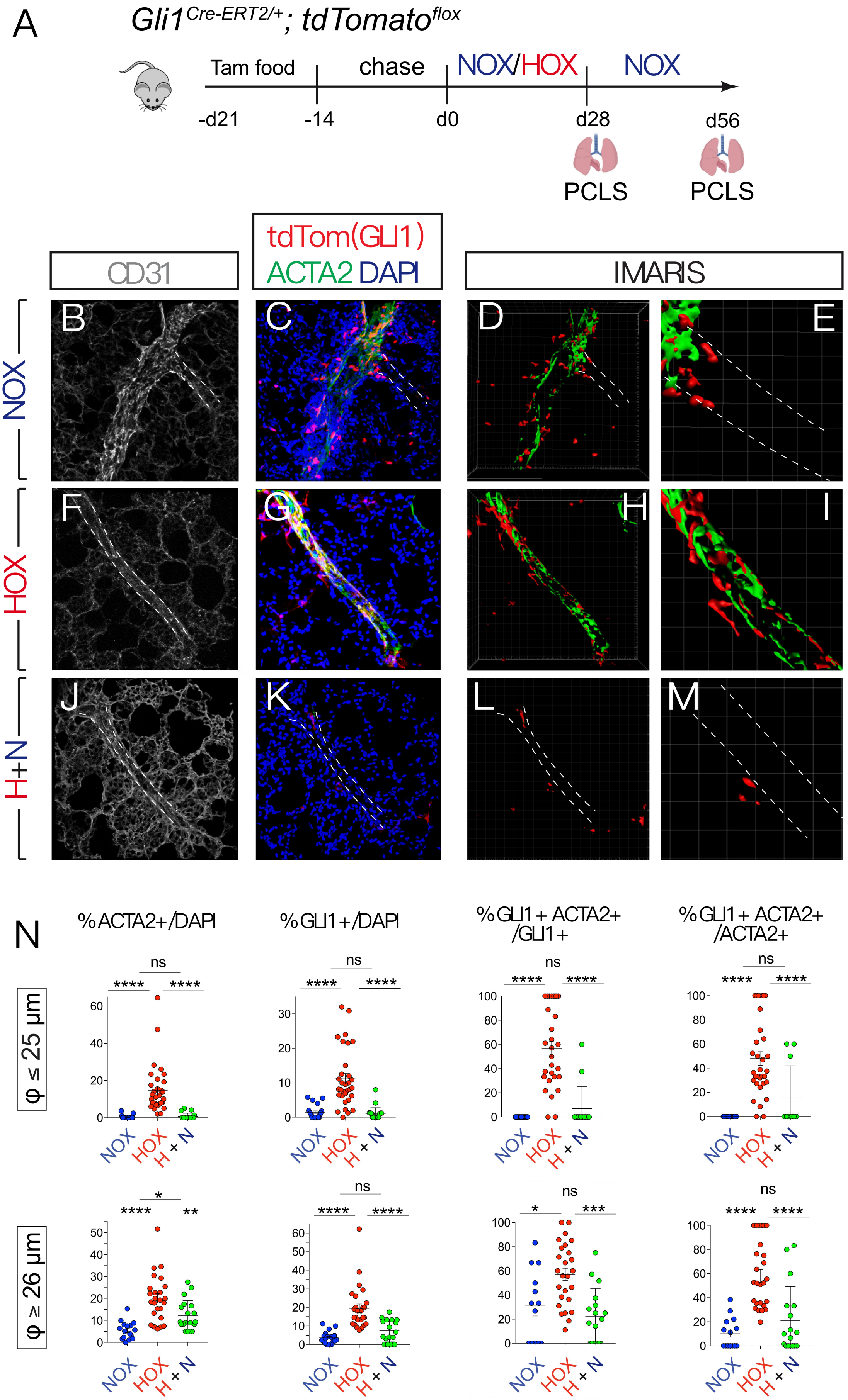
A
Gli1 Cre-ERT2/+; tdTomato flox
Tam food
chase
NOX/HOX
NOX
-d21
-14
d0
d28
d56
PCLS
PCLS
CD31
tdTom(GLI1)
ACTA2 DAPI
IMARIS
B
C
D
E
F
G
H
I
J
K
L
M
NOX
HOX
H+N
N
%ACTA2+/DAPI
%GLI1+/DAPI
%GLI1+ ACTA2+ /GLI1+
%GLI1+ ACTA2+ /ACTA2+
φ ≤ 25 µm
φ ≥ 26 µm
ns
****
*
**
***
0
10
20
30
40
50
60
80
100
NOX
HOX
H+N

Figure 7.: IMARIS-based quantification of GLI1+ cells in NOX, HOX (vascular remodeling), and HOX+NOX (reverse remodeling). A. Experimental set up for hypoxic injury using the *Gli1*$^{CreERT2/+}$; *tdTomato*^{flox} mice. **B-J**. IF for CD31 (B, E, H) and DAPI/ tdTom and ACTA2 (C, D, F, G, I, J) on PCLS sections from NOX (B-D), HOX (E-G), and HOX+NOX (H-J). **K.** IMARIS-based cell quantification on PCLS of distal arterioles (blood vessel diameter: 10-25 µm) and proximal arterioles (blood vessel diameter: 28-65 µm) for the presence of ACTA2 and/or GLI1+ cells.

Use of a second mouse model: Validation of smoke-induced PH

Apart from the fact that both hypoxia (HOX) and cigarette smoke exposure (SE) lead to PH formation in mice, it is still unclear whether common or distinct cellular mechanisms are at play for PH pathogenesis. Therefore, we investigated whether the GLI1+ cells also contributed to PH in SE mice. Studies have shown that compared to room air (RA) exposed mice, cigarette smoke exposure of mice led to increased right ventricular systolic pressure followed by right heart hypertrophy starting at three months of treatment (Seimetz, Parajuli et al. 2011). After eight months of cigarette smoke exposure in our experimental conditions, the onset of PH was confirmed in SE vs. RA mice. The increased ratio of the right ventricular (RV) and the left ventricular plus septum (LV+S) mass confirmed the presence of right heart hypertrophy, which is one of the most significant features acquired in PH. An increase in right ventricular systolic pressure also validated the functionality of our cigarette smoke exposure mouse model to induce PH.

FACS-based analysis of GLI1+ cells in SE vs. RA mice

Gli1$^{CreERT2/+}$; *Tom*^{flox} mice were exposed to RA or SE for eight months, and then lung samples were collected to perform further analysis. FACS analysis on lung samples was carried out. An increase was observed for ACTA2+ cells out of rMC in SE vs. RA (SE: 11.89% ± 1.489% n=3 vs. RA: 6.523% ± 0.9340%, n=3). Contrary to what was observed in HOX vs. NOX, we found that GLI1+ cells increased between SE and RA mice (SE: 41.6% ± 2.098% n=3 vs. RA: 21.37% ± 2.310% n=3) suggesting that GLI1+ cells were amplified in this PH model. The contribution of GLI1+ cells towards the ACTA2+ lineage out of the GLI1+ lineage (ratio ACTA2+GLI1+/GLI1+) also increased in SE vs. RA (SE: 8.645% ± 0.0957% n=3 vs. RA: 4.943% ± 0.6353% n=3). We also found a trend towards increased contribution of GLI1+ cells towards the

ACTA2+ lineage out of the ACTA2+ lineage (ratio ACTA2+GLI1+/ACTA2+) in SE vs. RA (SE: 31,33% ± 4,017%, n=3 vs RA: 20,53% ± 1,81%, n=3).

Reverse remodeling in the SE model can be achieved by L-NIL administration (Seimetz, Parajuli et al. 2011). Nitric oxide (NO) produced by inducible nitric oxide synthase (iNOS) is involved in pulmonary vascular wall damage during the onset of pulmonary hypertension (Seimetz, Parajuli et al. 2011). An effective and selective dose of an iNOS inhibitor, L-N6-(1-iminoethyl) lysine (L-NIL), can induce reverse remodeling, thereby rescuing the PH phenotype (Seimetz, Parajuli et al. 2011). We compared iNOS induced vascular reverse remodeling (SE+L-NIL) vs. cigarette smoke exposure induced vascular remodeling (SE). A decrease was observed for ACTA2+ cells out of rMC in SE+L-NIL (8,21% ± 0,4828%, n=3) vs. SE (11,89% ± 1,489%, n=3). GLI1+ cells also decreased in SE+L-NIL (19,33% ± 1,036%, n=3) vs. SE (41,6% ± 2,098%, n=3). suggesting that GLI1+ cells were amplified in this PH model. The contribution of GLI1+ cells towards the ACTA2+ lineage out of the GLI1+ lineage (ratio of ACTA2+GLI1+/GLI1+) did not significantly change in SE+L-NIL vs. SE. However, we found a significant decrease in the contribution of GLI1+ cells towards the ACTA2+ lineage out of the ACTA2+ lineage (ratio of ACTA2+GLI1+/ACTA2+) in SE+L-NIL vs. SE. The GLI1+ cells appear to be causative for the PH phenotype in this model. This model seems to involve GLI1+ cell proliferation and differentiation towards the ACTA2 lineage, while the HOX model only consists of the differentiation of these cells.

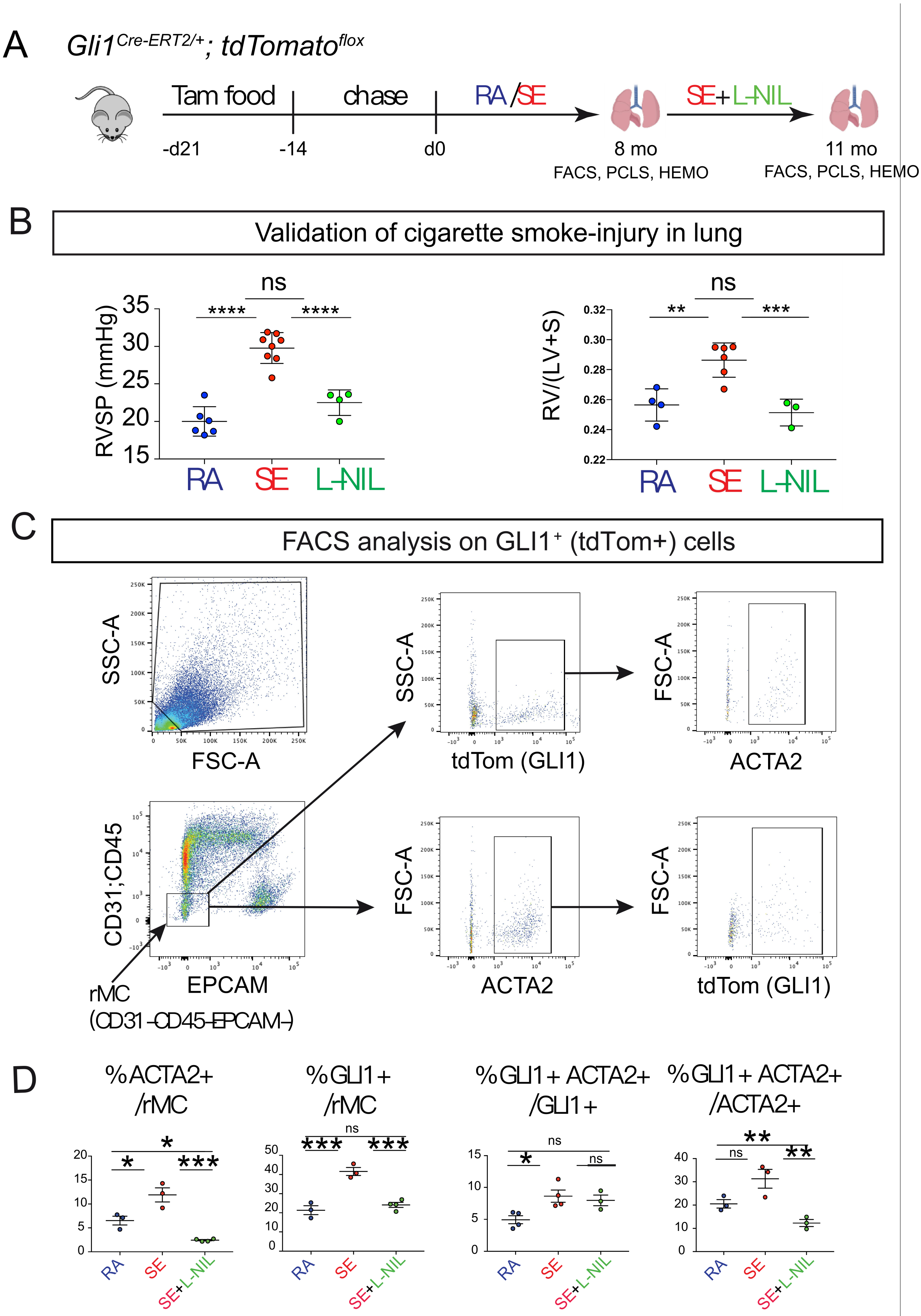
A
Gli1Cre-ERT2/+; tdTomatoflox
Tam food
chase
RA /SE
SE+L-NIL
-d21
-14
d0
8 mo
FACS, PCLS, HEMO
11 mo
FACS, PCLS, HEMO
B
Validation of cigarette smoke-injury in lung
RVSP (mmHg)
35
30
25
20
15
ns
****
****
RA
SE
L-NIL
RV/(LV+S)
0.32
0.30
0.28
0.26
0.24
0.22
ns
**
***
RA
SE
L-NIL
C
FACS analysis on GLI1+ (tdTom+) cells
SSC-A
FSC-A
SSC-A
tdTom (GLI1)
FSC-A
ACTA2
CD31;CD45
EPCAM
rMC
(CD31-CD45-EPCAM-)
FSC-A
ACTA2
FSC-A
tdTom (GLI1)
D
%ACTA2+
/rMC
%GLI1+
/rMC
%GLI1+ ACTA2+
/GLI1+
%GLI1+ ACTA2+
/ACTA2+
20
15
10
5
0
*
*
***
50
40
30
20
10
0
ns
***
***
15
10
5
0
ns
*
ns
40
30
20
10
0
**
ns
**
RA
SE
SE+L-NIL

Figure 8. **Validation of cigarette smoke injury in *Gli1*$^{CreERT2/+}$*; tdTomato*^{flox} mice by hemodynamics and flow cytometry. A.** Experimental set up for vascular remodeling induced by cigarette smoke exposure (SE) injury and reverse remodeling using L-NIL. Room air-exposed (RA) mice were used as controls. **B.** Hemodynamic measurements in RA and SE mice at 8 months. **C.** FACS strategy to isolate GLI1+ (tdTomato+) cells. **D.** Corresponding FACS quantification.

GLI1+ cells quantified on PCLS by IMARIS-based 3D rendering indicate an increased contribution of GLI1+ cells mainly in the smaller arterioles during vascular remodeling following SE exposure

To confirm the flow cytometry data above, we determined whether GLI1+ cells give rise to ACTA2+ cells around the arterioles in lung (Fig 9). RA or SE treatment of *Gli1*$^{Cre\text{-}ERT2}$*; tdTomoto*^{flox} mice started two weeks after the one-week- tamoxifen food regimen. Lung samples were collected after 8 months of RA or SE and 11 months for SE+L-NIL. 200 µm thick PCLS were prepared by vibratome and stained for DAPI, ACTA2, and CD31. Confocal pictures were then taken (and maximum projection pictures were processed through the IMARIS software to get high-resolution 3D rendering of GLI1+ and ACTA2+ cells. CD31 signal delineated the blood vessel, and DAPI was used to distinguish individual cells.

Like for the HOX model, we separated the vessels into distal arterioles (blood vessel diameter smaller than 25 µm) and proximal blood arterioles (blood vessel diameter greater than 28 µm). As a quality control, we also compared blood vessels with equal diameters in our different groups (Fig. 9C). We also considered a similar number of blood vessels (Fig. 9D). (Each dot represents a blood vessel). Although PH formation in the SE model was suggested by the hemodynamic measurements and the FACS approach, IMARIS-based quantification and analysis of ACTA2+ cells in the blood vessel wall provide a superior validation that this pathological process occurred.

First, we compared SE vs. RA. Then, we quantified the ACTA2+, GLI1+ and GLI1+ ACTA2+ cells in the small arterioles. Each dot on the graphs displayed in Fig. 3N represents one blood vessel (10-30 blood vessels total per condition, 5 bv per animal, n= 3-5 per condition). We observed an increase in the percentile of ACTA2+ cells in SE vs. RA. (17,52% ± 4,275%, n=4, 0,4463% ± 0,2370%, n=4, respectively). A similar increase was observed for GLI1+ cells (6,137 % ± 2,024 %, n=4, 0,9199% ± 0,3941%, n=4, respectively) as well as for GLI1+ACTA2+ out of GLI1+ (53,10% ± 10,22%, n=4, 0,000% ± 0,000%, n=4, respectively) and GLI1+ACTA2+ out of ACTA2+ (44,26% ± 9,06%, n=4, 0,000% ± 0,000%, n=4, respectively). These data are validating the flow cytometry results (Fig. 5) and confirm that GLI1+ cells contribute to 40% of the newly formed ACTA2+ cells in the small arterioles upon SE exposure.

Next, a similar quantification was carried out in the proximal arterioles in SE vs. RA. Our results indicate an increase in the percentile of ACTA2 cells (13.77% ± 2.234%, n=4, 6.212% ± 1.249%, n=4, respectively indicating increased muscularization. The percentile of GLI1+ cells does not appear to significantly increase (4.578% ± 1.698%, n=4, 2.273% ± 0.6626%, n=4, respectively). This is also the case of the GLI1+ACTA2+ out of GLI1+ (55.89% ± 5.190%, n=4, 14.69% ± 6.065%, n=4, respectively). The only significant increase is the percentile of GLI1+ACTA2+ out of ACTA2+ (32.40% ± 6.944%, n=4, 8.595% ± 3.520%, n=4, respectively). Altogether these results indicate that in the SE model, proliferation and differentiation of the GLI1+ cells occur in the distal arterioles, while in the proximal arterioles, only differentiation is observed. Second, we compared SE + L-NIL vs. SE. In the small arterioles, a decrease was observed for ACTA2+ cells out of rMC in SE+L-NIL vs. SE (17.52% ± 4.275%, n=4, 2.907% ± 1.611%, n=4, respectively). GLI1+ cells also decreased in SE+L-NIL vs. SE (0.9603 ± 0.3919%, n=4, 6.137% ± 2.204%, n=4, respectively).

The contribution of GLI1+ cells towards the ACTA2+ lineage out of the GLI1+ lineage (ratio ACTA2+GLI1+/GLI1+) as well as out of the ACTA2+ lineage also decreased. In the proximal arterioles, a decrease was observed for ACTA2+ cells out of rMC in SE+L-NIL vs. SE (5.195% ± 3.353%, n=4, 53.10% ± 10.22%, n=4, respectively).

However, the percentile of GLI1+ cells over rMC and the contribution of GLI1+ cells towards the ACTA2+ lineage out of the GLI1+ lineage (ratio ACTA2+GLI1+/GLI1+) was not impacted by L-NIL treatment. Interestingly, the contribution of GLI1+ cells towards the ACTA2+ lineage out of the ACTA2+ lineage was decreased, suggesting that the L-NIL has an impact on the differentiation of the GLI1+ cells

In conclusion, the GLI1+ cells appear to be causative for the PH phenotype in the SE model. This model seems to involve GLI1+ cell proliferation and differentiation towards the ACTA2 lineage, while the HOX model only involves the differentiation of these cells. There is also a difference between proximal (differentiation) and distal arterioles (proliferation and differentiation) in the SE model.

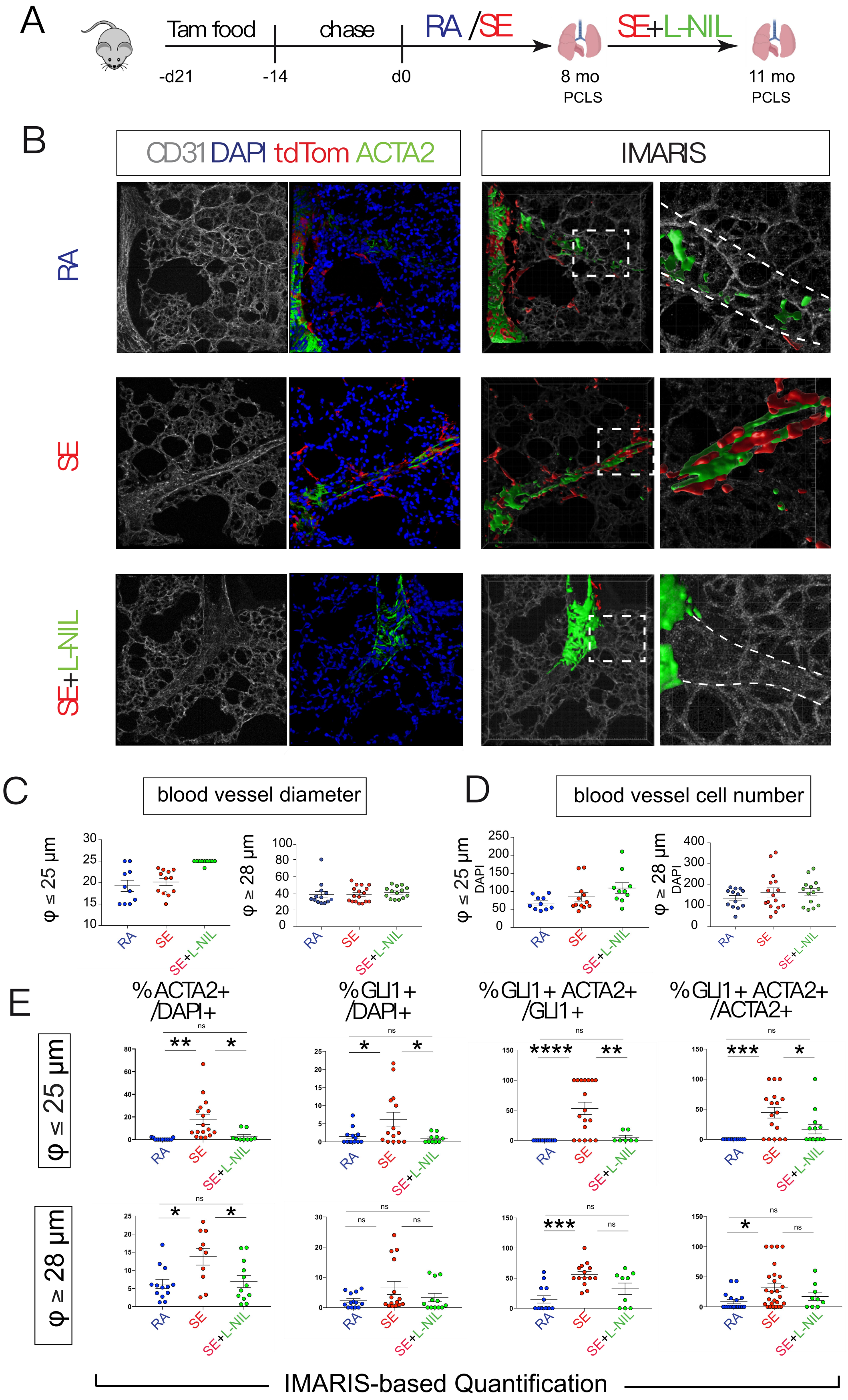
A
Tam food
chase
RA /SE
SE+L-NIL
-d21
-14
d0
8 mo
PCLS
11 mo
PCLS
B
CD31 DAPI tdTom ACTA2
IMARIS
RA
SE
SE+L-NIL
C
blood vessel diameter
φ ≤ 25 μm
φ ≥ 28 μm
RA
SE
SE+L-NIL
D
blood vessel cell number
φ ≤ 25 μm DAPI
φ ≥ 28 μm DAPI
E
%ACTA2+ /DAPI+
%GLI1+ /DAPI+
%GLI1+ ACTA2+ /GLI1+
%GLI1+ ACTA2+ /ACTA2+
φ ≤ 25 μm
φ ≥ 28 μm
ns
*
**
***
****
IMARIS-based Quantification

Figure 9. IMARIS-based quantification of GLI1+ cells in RA, SE (vascular remodeling), and SE+L-NIL (reverse remodeling). A. IF for CD31 and DAPI/ tdTom and ACTA2 on PCLS sections from RA, SE, and SE+L-NIL. **B.** IMARIS-based cell quantification on PCLS of the diameters of the blood vessels selected for quantification in the distal arteriole and proximal arteriole groups in RA, SE and SE+L-NIL animals. **C.** IMARIS-based cell quantification on PCLS of total cell number of the blood vessels selected for quantification in the distal arteriole and proximal arteriole groups in RA, SE and SE+L-NIL animals. **D.** IMARIS-based cell quantification on PCLS of distal arterioles (blood vessel diameter: 10-25 µm) and proximal arterioles (blood vessel diameter: 28-65 µm) for the presence of ACTA2 and/or GLI1+ cells.

Objective 2: To determine if GLI1+ cells are functionally involved in the pathogenesis of PH

Genetic ablation of GLI1+ cells indicate that these cells are functionally involved in the pathogenesis of PH driven by HOX.

Next, we tested whether GLI1+ cells are causative for PH using a genetic ablation approach for GLI1+ cells specifically. *Gli1*$^{Cre\text{-}ERT2}$*; tdTomato*^{flox} mice were crossed with *iDTR*^{flox} mice to generate *Gli1*$^{Cre\text{-}ERT2}$*; tdTomato*^{flox}*; iDTR*^{flox} mice (Figure 10A). Administration of tamoxifen allowed the expression of diphtheria toxin receptors in GLI1+ cells specifically. Upon the injection of diphtheria toxin (DTX, experimental group), genetic ablation of GLI1+ cells were carried out in mice. PBS injection were used as the control group. The injection of DTX or PBS was carried out at the beginning of hypoxia exposure (Fig 10B). As shown in the confocal pictures of DTX vs. PBS-treated lungs in proximal and distal arterioles (Fig. 10C-F), genetic cell ablation was efficiently carried out as indicated by a significant reduction of GLI1+ cells. Echocardiography measurements show that deletion of GLI1+ cells before hypoxia exposure decreased the severity of the PH phenotype (Fig. 10G). We measured and compared the cardiac output (CO), cardiac index (CI), right ventricle walls thickness (RVWT) and the tricuspid annular plane systolic excursion (TAPSE) in HOX+PBS vs. HOX+DTX animals. We observed an increase in CO and CI, indicating that the heart function normalizes upon GLI1+ cell ablation. In addition, the

RVWT decreases and TAPSE increase indicated a reduction of the right heart hypertrophy.

Next, IF images of PCLS generated from the lungs of these mice were subjected to IMARIS-quantification as previously described. Results are shown in Fig. 4H. Each dot on the graphs represents one vessel from PCLS made from HOX+PBS (8-10 blood vessels total per condition, 3-5 PCLS per animal, n= 3 animals) or HOX+DTX lungs (3-5 blood vessels total per condition, 5-7 PCLS per animal, n= 4 animals).

We have compared IMARIS-based quantification generated from HOX+PBS vs. HOX+DTX PCLS. In small arterioles, we observed a decrease in the percentage of ACTA2+ cells (HOX+PBS: 14,43% ± 1,992, n= 3; HOX+DTX: 2,143% ± 0,7241%, n=4). A similar decrease was observed for GLI1+ cells (HOX+PBS: 9,887% ± 1,349%, n=3; 1,065% ± 0,4391%, n=4). While GLI1+ACTA2+ out of ACTA2+ cells showed a trend towards a decrease (HOX+PBS: 43,62% ± 5.125%, n= 3; HOX+DTX: 3.961% ± 2.177%, n=4), the quantification of GLI1+ACTA2+ out of GLI+ indicated a significant decrease (HOX+PBS: 61,14% ± 5.898%, n= 3; HOX+DTX: 9.712% ± 5%, n=4).

Similar observations were made for the proximal arterioles for the percentile of ACTA2 (HOX+PBS: 20,38%±1,671%, n=3; HOX+DTX: 10,85% ± 1.312%, n=4) and GLI1 (HOX+PBS: 14,17% ± 1.534%, n= 3; HOX+DTX: 3,433% ± 0,9456%, n=4). In addition, the contribution of GLI1+ACTA2+ double positive cells to the pool of ACTA2+ cells is decreased (HOX+PBS: 62,63% ± 4.607%, n= 3; HOX+DTX: 10,36% ± 2.976%, n=4) while only a trend towards the percentile of GLI1+ACTA2+ out of GLI1+ cells are observed (HOX+PBS: 61,80% ± 4,428%, n= 3; HOX+DTX: 29,76% ± 7,167%, n=4). This indicates that in DTX-treated animals most of the reverse remodeling process occurs in the distal arterioles.

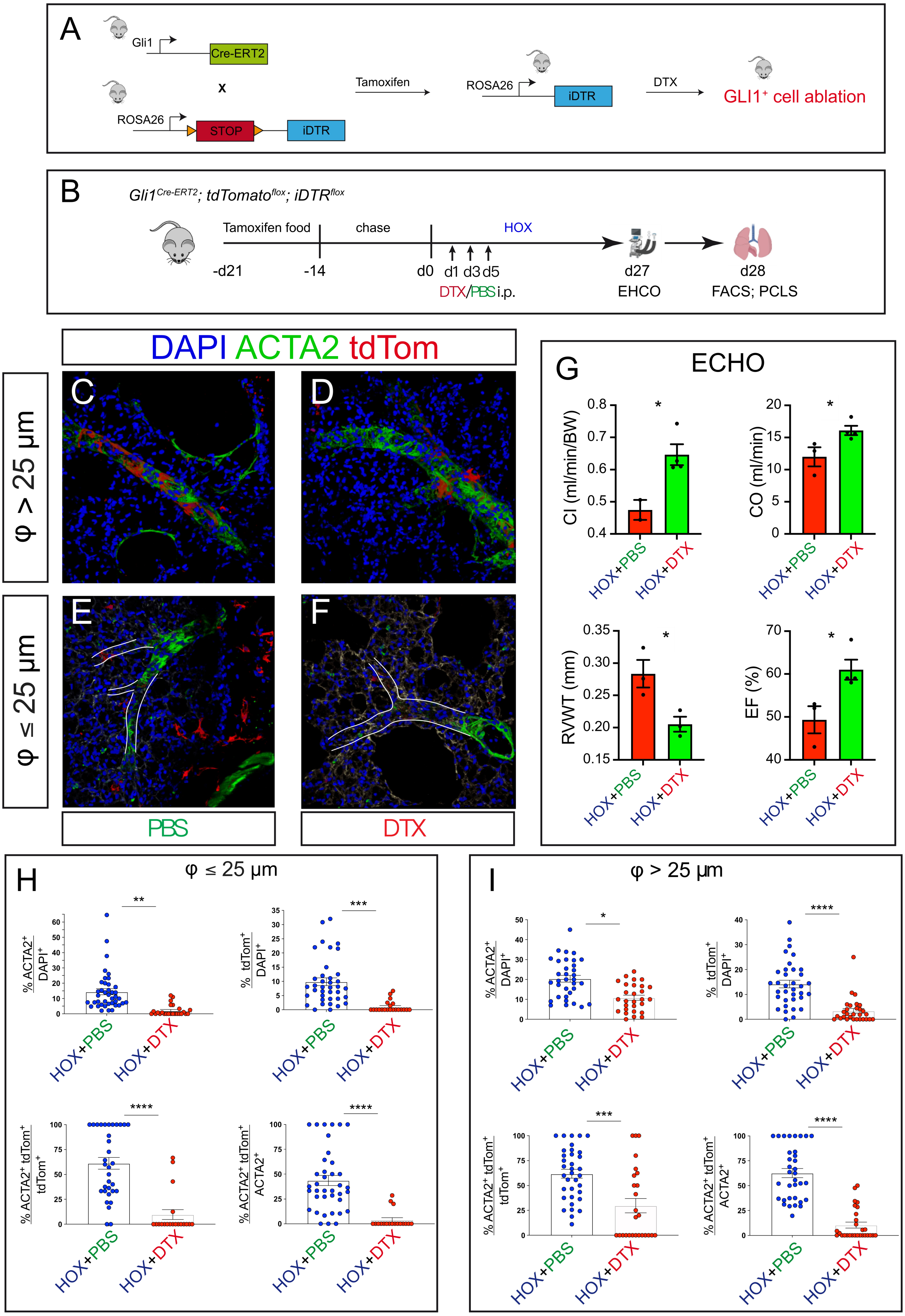
A
Gli1
Cre-ERT2
x
ROSA26
STOP
iDTR
Tamoxifen
ROSA26
iDTR
DTX
GLI1⁺ cell ablation
B
Gli1Cre-ERT2; tdTomatoflox; iDTRflox
Tamoxifen food
chase
HOX
-d21
-14
d0
d1 d3 d5
DTX/PBS i.p.
d27
EHCO
d28
FACS; PCLS
DAPI ACTA2 tdTom
φ > 25 µm
φ ≤ 25 µm
C
D
E
F
PBS
DTX
G
ECHO
CI (ml/min/BW)
CO (ml/min)
RVWT (mm)
EF (%)
HOX+PBS
HOX+DTX
H
φ ≤ 25 µm
% ACTA2⁺ / DAPI⁺
% tdTom⁺ / DAPI⁺
% ACTA2⁺ tdTom⁺ / tdTom⁺
% ACTA2⁺ tdTom⁺ / ACTA2⁺
I
φ > 25 µm
*
**
***
****

Figure 10. Genetic ablation of GLI1+ cells protect from PH. A. Schematic for the genetic ablation of GLI1+ cells using the *Gli1*$^{CreERT2/+}$*; tdTomato*^{flox}*; iDTR*^{flox} mice. **B**. Experimental set up for GLI1+ cells genetic ablation during HOX using *Gli1*$^{CreERT2/+}$*; tdTomato*^{flox}; *iDTR*^{flox} mice. Echocardiography and FACS were used as readouts on days 27 and 28. **C-F**. IF for DAPI, tdTomato, CD31 and ACTA2 on PCLS from PBS-treated (C, E) and DTX-treated (D, F) lungs. Representative pictures of distal arterioles (diameter 10-25 µm) and proximal arterioles (26-65 µm). **G.** Echocardiography of PBS- and DTX-treated mice at day 27 after HOX. **H.** IMARIS-based cell quantification on PCLS of distal arterioles (10-25 µm) and proximal arterioles (26-65 µm) for the presence of ACTA2 and/or GLI1+ cells. **I.** FACS-based quantification of GLI1+ cells in PBS- or DTX-treated animals at day 28.

Objective 3: To apply single cell sequencing analysis on GLI1+ cells during hypoxia-induced PH

Different sub-populations of GLI1+ cells respond to HOX

Next, we used scRNAseq on FACS-isolated GLI1+ cells from NOX and HOX group to analyse the cellular composition of GLI1+ cells and their respective responses to hypoxia exposure. We used the 10X genomic platform to analyze 6623 and 5941 cells in HOX and NOX. Our quality control steps indicate that we have choosen relatively unbiased cell populations represent the biological heterogeneity under different conditions.

The comparison of the UMAP in NOX and HOX is shown in Fig. 11A. Our results indicate that the GLI1+ cells can be grouped in 4 clusters, which could be further grouped into 12 subclusters. Cluster A, made of Clusters 8-12 is related to SMC (subcluster 8: SMC-Pericyte subset 2, subcluster 9: VSMCs, subcluster 10: SMC pericyte subset 1, subcluster 11: Endo/mesenchymal progenitor's subset 1 and subcluster 12 Endo/mesenchymal progenitor's subset 2). Cluster B made of subclusters 4 and 5 is related to lipofibroblasts. Cluster C made of subclusters 6 and 7, which are related to the Myofibroblasts/matrix fibroblasts, and finally cluster D made of subclusters 1-3, which are related to the Col14a1+ matrix fibroblasts. As PH development involves the increased presence of ACTA2+ cells in the blood vessels, we focussed on ACTA2+ cells. Cluster A, in particular subcluster 9, expresses a high level of *Acta2* as well as *Pdgfrb* and *Myh11* (Figure 11C). In addition, the cell distribution in subcluster 8-12 is shown in Fig. 11D and indicates that the number of cells in subclusters 8, 10 and 11 decreases in HOX vs. NOX. While the number of cells in subcluster 9 increases in HOX vs. NOX. A minor increase is also observed in subcluster 12. Subcluster 9 contains the VSMC and likely corresponds to the newly formed ACTA2+ cells upon HOX. Figure 11E describes the top genes differentially expressed within subclusters 8-12. The top differentiated genes in subcluster 9 are the markers of VSMCS, such as *Acta2*, *Myh11*, and *Tagln*. Additionally, markers of pericytes have also been found to be upregulated in subcluster 9, such as *Tpm1* and *Tpm2*. Although subclusters 8, 9 and 10 share similar SMC markers, subcluster 9 contains a unique genomic signature compared to subclusters 8 and 10. Finally, we carried out a velocity analysis on the subclusters 8-12. Our analysis indicates that VSMCs (subcluster 9) originate from SMC/pericytes (Subclusters 8 and 10), which themselves arise from Endothelial/mesenchymal progenitors (subclusters 11 and 12) (Figure 11F).

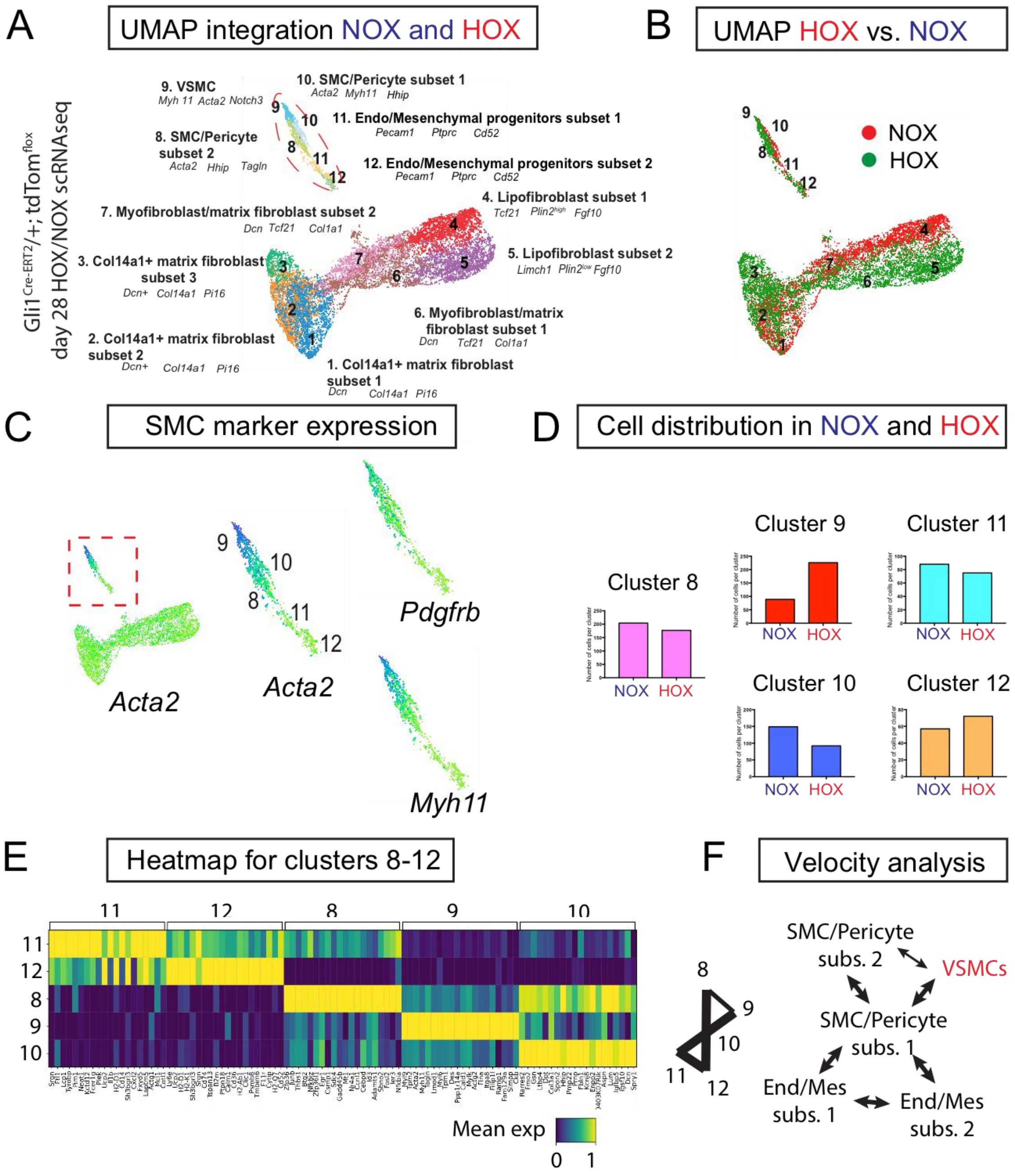

Figure 11. scRNAseq analysis of FACS-isolated GLI1+ cells in HOX and NOX. A. UMAP integration for GLI1+ scRNAseq data from NOX and HOX lungs on day 28. **B.** NOX and HOX origin of the cells displayed in the integrated UMAP. **C.** *Acta2*, *Pdgfrb* and *Myh11* expression are enriched in clusters 8-12. **D.** Quantification of the NOX and HOX cell number in clusters 8-12. **E.** Heatmap for the top 20 genes differentially expressed in clusters 8-12. **F.** Velocity analysis of clusters 8-12.

Objective 4: Validation of a novel *Fgf10*$^{Cre\text{-}ERT2}$ knock-in line

Generation of a novel *Fgf10* knock-in line (C57BL6-Fgf10tm2 (YFP-Cre-ERT2) Sbel/J aka *Fgf10*$^{KI\text{-}v2}$)

129Sv ES cells were electroporated with a targeting vector containing the first 3 kb of exon 3 of the *Fgf10* open reading frame (Fig.12A, B). Immediately downstream of the stop codon of exon 3 is the F2A sequence encoding for the self-cleaving peptide, followed by the coding sequence of eYFP, the self-cleaving peptide sequence T2A, the tamoxifen-inducible form of *Cre* recombinase (*Cre-ERT2*)(Feil, Wagner et al. 1997), and the Neomycin-resistance gene (Neo) respectively. Resistant ES cell clones were selected, screened by PCR and then verified by Southern blotting. Selected ES clones were injected into C57BL/6J blastocysts to generate chimeric pups (Fig. 12C). Chimeras were then crossed with C57BL/6J mice ubiquitously expressing *Flp* recombinase to generate heterozygous *Fgf10*$^{Ki\text{-}v2}$ knock-in mice where the *Neo* cassette was totally excised (Fig. 12D). Genotyping strategy with primers P1/P2 (with P1 located just before the STOP codon and P2 being part of the F2A sequence) to detect the *Fgf10*$^{Ki\text{-}v2}$ mutant allele and P3/P4 (located before and after the STOP codon in exon 3, respectively) to detect the *Fgf10*+ wild type allele (Fig. 12E).

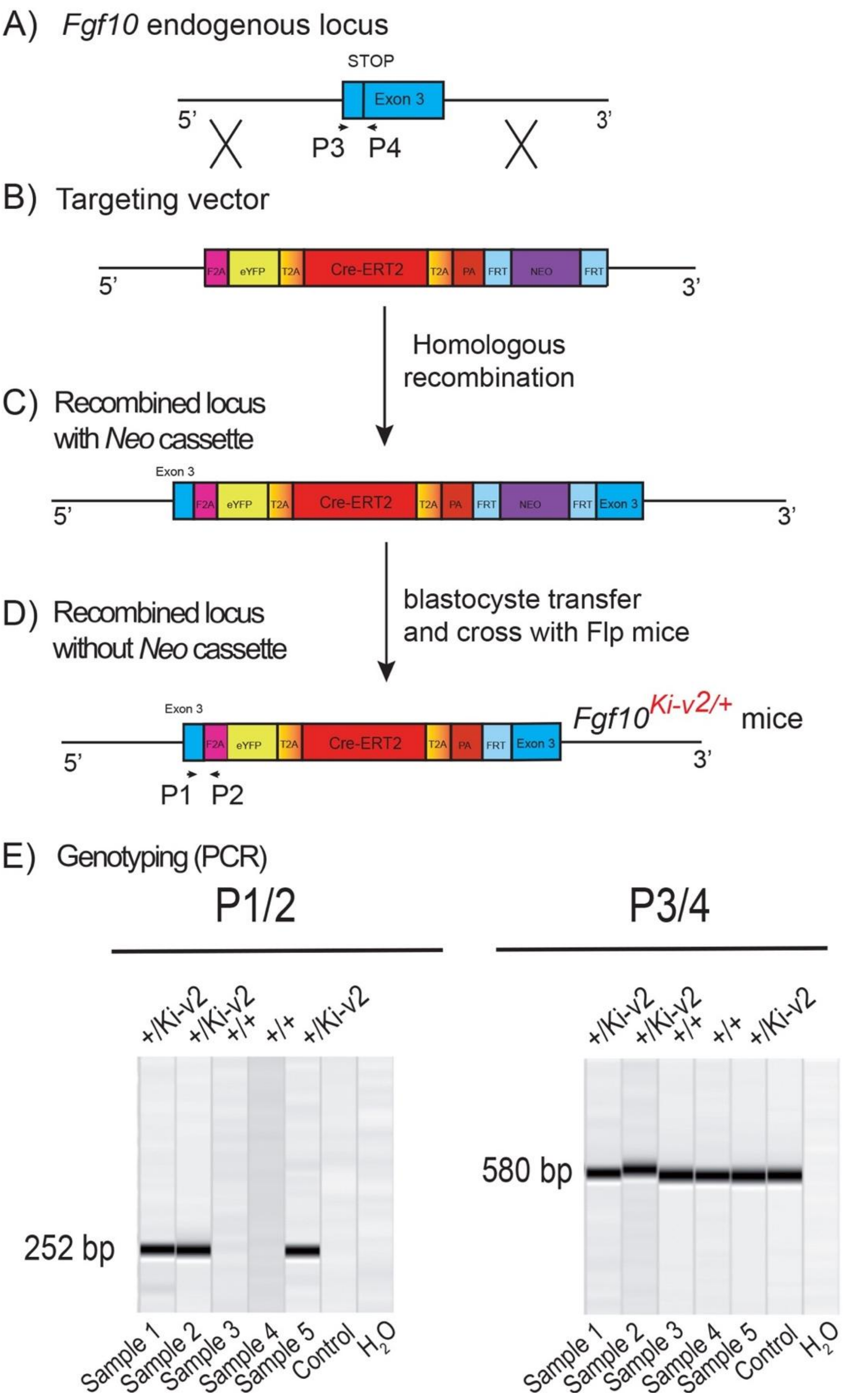

Figure 12. Generation and genotyping of the novel *Fgf10*$^{Ki\text{-}v2}$ line. (A, B) Homologous recombination was carried out to insert the *F2A-eYFP-T2A-Cre-ERT2-T2A-PA-NEO* construct in frame with the stop codon of exon 3 of the mouse *Fgf10* gene. Neomycin resistance coding gene was used for the

positive selection. **(C, D)** Recombined ES cells clones were treated with flippase to remove the Neo cassette and blastocyst transfer of the selected ES cells was carried out to generate chimera animals. **(E)** PCR strategy to genotype mutant and wild type animals. Primers 1 and 2 were used for the detection of the mutant *Fgf10*$^{Ki\text{-}v2}$ allele (252 bp) and Primers 3 and 4 were used for the detection of the wild type *Fgf10+* allele (580 bp). (Chu, Taghizadeh et al. 2021)

Validation of Cre activity to label FGF10+ cells during embryonic development

To test the recombinase activity of Cre-ERT2, *Fgf10*$^{Ki\text{-}v2/+}$ heterozygous mice were crossed with *tdTomato*$^{flox/flox}$ reporter mice. Pregnant mice received a single intraperitoneal (IP) injection of tamoxifen at E11.5 (Fig. 13A) or E15.5 (Fig. 14A). Embryos were harvested at E18.5. No fluorescent signal was observed in *Fgf10*$^{+/+}$*; tdTomato*$^{flox/+}$ embryos (Fig. 13B and Fig. 14B; n=4) indicating the absence of recombination in control embryos and lack of leakiness of the *tdTomato*^{flox} allele. By contrast, tamoxifen treatment at E11.5 led to a strong fluorescent signal in the limbs, stomach, cecum, colon and lungs of *Fgf10*$^{Ki\text{-}v2/+}$*; tdTomato*$^{flox/+}$ embryos (n=3). In the limb, the labeled cells were more abundant in the digit tip area, known to express a high level of *Fgf10* (Danopoulos, Parsa et al. 2013). Along the gastro-intestinal tract, labeled cells were located in the anterior part of the stomach and in the duodenum (data not shown) both reported to express a high level of *Fgf10* (Lv, Wu et al. 2019). A similar observation was made in the cecum and the distal colon (Lv, Wu et al. 2019). We found a robust tdTomato expression throughout the lung with a higher expression in the interlobular septa. This is similar to what was observed with the previously validated *Fgf10*^{LacZ} reporter line and *Fgf10*$^{KI\text{-}v1/+}$ line (Mailleux, Kelly et al. 2005, El Agha, Al Alam et al. 2012, El Agha, Herold et al. 2014). Interestingly, no labelled cells were observed in the trachea in this experimental condition (Fig. 13C). Additionally, tamoxifen treatment at E15.5 revealed a strong fluorescent signal in the pinna of the developing ear and the trachea and in between the cartilage rings (Fig. 14C). These two additional expression domains are consistent with sites of *Fgf10* expression (Sala, Del Moral et al. 2011, Zhang, Fons et al. 2020). We, therefore, conclude that *Cre* expression reflects *Fgf10* expression and that this line can be used to target FGF10+ cells.

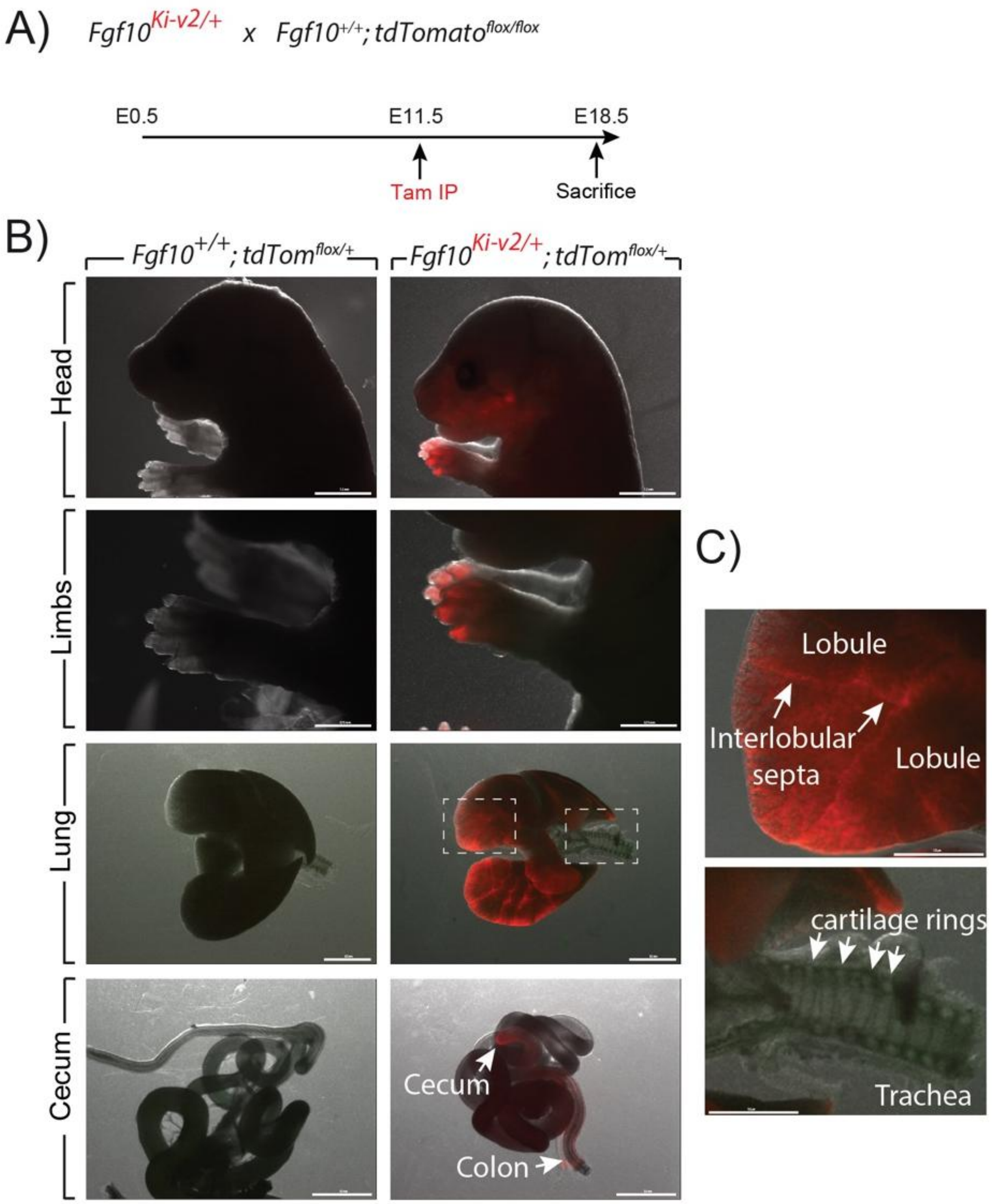

Figure 13. Validation of the labeling of FGF10+ cells at E11.5. (A) *Fgf10*$^{Ki\text{-}v2/+}$ were crossed with *Fgf10*$^{+/+}$; *tdTom*$^{flox/flox}$ mice. Pregnant females received a single injection of tamoxifen IP when the embryos were at E11.5 and sacrificed at E18.5. **(B)** Head, limbs, lung and cecum of *Fgf10*$^{+/+}$; *tdTom*$^{flox/+}$ and *Fgf10*$^{Ki\text{-}v2/+}$; *tdTom*$^{flox/+}$ embryos are shown. Note the absence of fluorescence in the *Fgf10*$^{+/+}$; *tdTom*$^{flox/+}$ indicating that the non-recombined *LoxP-Stop-LoxP-*

tdTomato allele is not leaky. **(C)** Higher magnification of lung and trachea showing enriched tdTomato expression in the interlobular septa and the lack of tdTomato expression between the cartilage rings, respectively. Scale bar in **(B)**: head: 1.5 mm, Limb: 0.75 mm, Lung: 0.5 mm, cecum: 0.5 mm. Scale bar in **(C)**: 125 µm. (Chu, Taghizadeh et al. 2021)

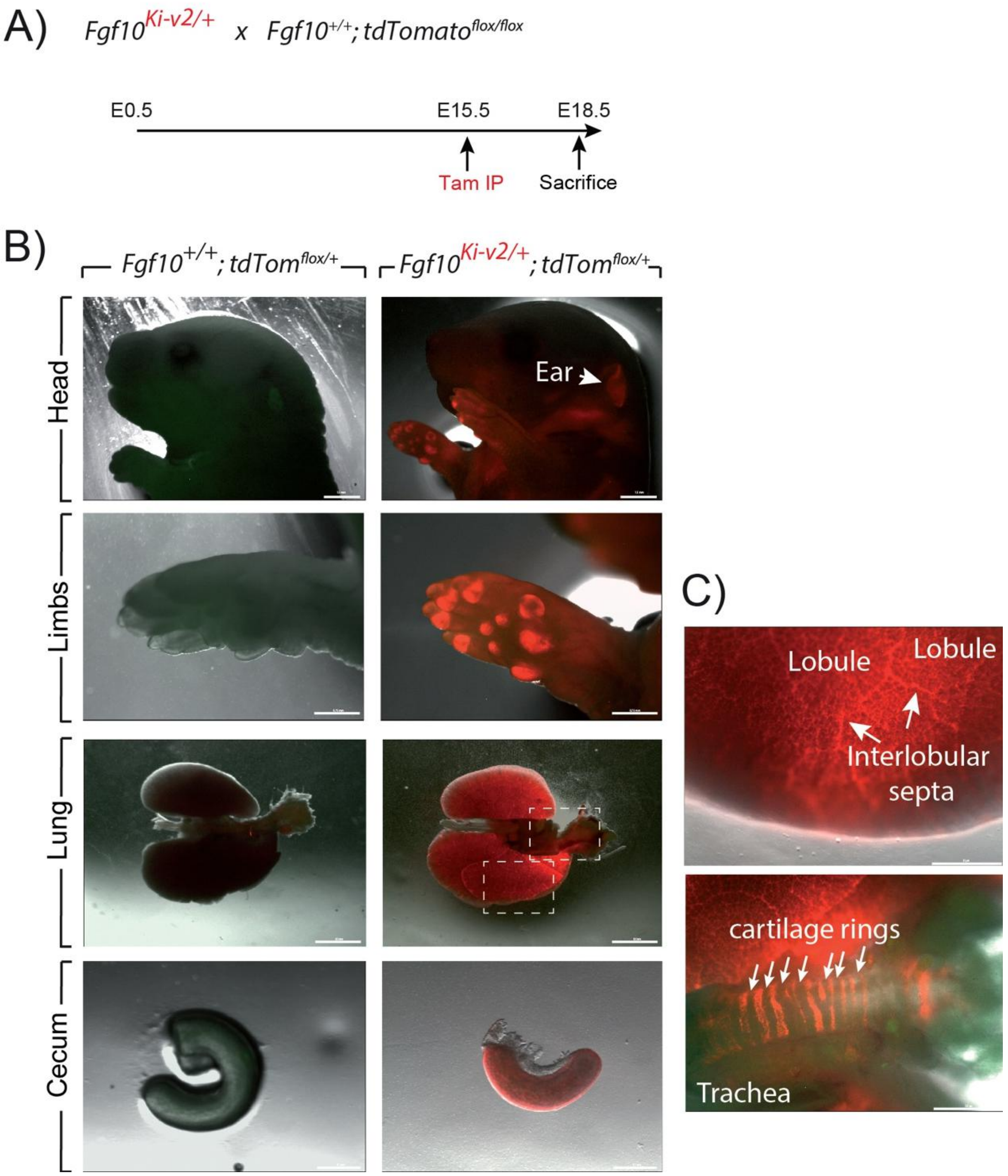

Figure 14. Validation of the labeling of FGF10+ cells at E15.5. (A) $Fgf10^{Ki-v2/+}$ were crossed with $Fgf10^{+/+}$; $tdTom^{flox/flox}$ mice. Pregnant females received a single injection of tamoxifen intraperitoneal (IP) when the embryos

were at E15.5 and sacrificed at E18.5. **(B)** Head, limbs, lung and cecum of *Fgf10*$^{+/+}$; *tdTom*$^{flox/+}$ and *Fgf10*$^{Ki\text{-}v2/+;}$ *tdTom*$^{flox/+}$ embryos are shown. Note the expression in the external ear (arrow). **(C)** Higher magnification of lung and trachea showing enriched tdTomato expression in the interlobular septa and the presence of tdTomato expression between the cartilage rings, respectively. Scale bar in **(B)**: head: 1.5 mm, Limb: 0.75 mm, Lung: 0.5 mm, Cecum: 0.1 mm. Scale bar in **(C)**: Lung 25 µm, Trachea 125 µm. (Chu, Taghizadeh et al. 2021)

FGF10+ cells labelled after birth contribute to the lipofibroblast lineage but not to the smooth muscle cell lineage

Using the previously generated *Fgf10*$^{Ki\text{-}v1/+}$ line, we demonstrated that FGF10+ cells labelled postnatally strongly contribute to the lipofibroblast (LIF) lineage but not the smooth muscle cell (SMC) lineage. In particular, they do not contribute in a major way to the Acta2+ secondary crest myofibroblasts (SCMF), which are abundant during the first 2-3 weeks during alveologenesis, which takes place from postnatal day 5 (P5) to -P28(El Agha, Herold et al. 2014). To confirm this observation with the new *Fgf10*$^{Ki\text{-}v2/+}$ line, we labelled FGF10+ cells at P4 and examined the status of the labelled cells at P21, one week before the end of the alveologenesis phase (Fig. 15A). Analysis of the whole lung by fluorescence stereomicroscope indicated a much higher number of labelled cells in the *Fgf10*$^{Ki\text{-}v2}$*; tdTomato*$^{flox/+}$ lung compared with the *Fgf10*$^{Ki\text{-}v1;}$ *tdTomato*$^{flox/+}$ lung (Fig. 15B). Quantification of tdTom+ cells indicated that a higher percentile of tdTom+/DAPI is observed on sections of *Fgf10*$^{Ki\text{-}v2}$*; tdTomato*$^{flox/+}$ vs. *Fgf10*$^{Ki\text{-}v1;}$ *tdTomato*$^{flox/+}$ (4.7% ± 0.6% vs. 1.5% ± 0.2%, n=2) thereby confirming the fluorescence stereomicroscopy results (Fig. 15C). LipidTOX staining of these lungs was used to visualize LIFs (Fig. 15D). Quantification of this staining indicated that 62.6% ± 5.0% (n=2) of the total tdTom+ are LT+ and that 27.0% ± 4.4 % (n=2) of the LT+ derive from tdTom+ cells. These data align with our results obtained with the previous *Fgf10*$^{Ki\text{-}v1/+}$ line. Immunofluorescence (IF) for ACTA2 on these lungs was also carried out (Fig. 15E and 15F). First, we quantified the number of ACTA2+/tdTom+ present in the respiratory airway (Fig. 15E). ACTA2+ cells in the respiratory airway during alveologenesis mark secondary crest myofibroblasts (SCMF). We found 4.7% ± 0.9% (n=2) tdTom+ACTA2+/tdTom+ indicating in our experimental conditions, a minimal commitment of the FGF10+ cells to the SCMF lineage. Second, we identified peribronchial tdTom+ cells in longitudinal and crosssections of the bronchi (Fig. 15F). Airway smooth muscle cells express ACTA2 and display the typical bundle-like circular shape, which is located in near the bronchial epithelium. tdTom+ cells are located close to ACTA2+ ASMCs but are nevertheless negative for ACTA2. A similar observation was made for the perivascular tdTomato+ cells (data not shown).

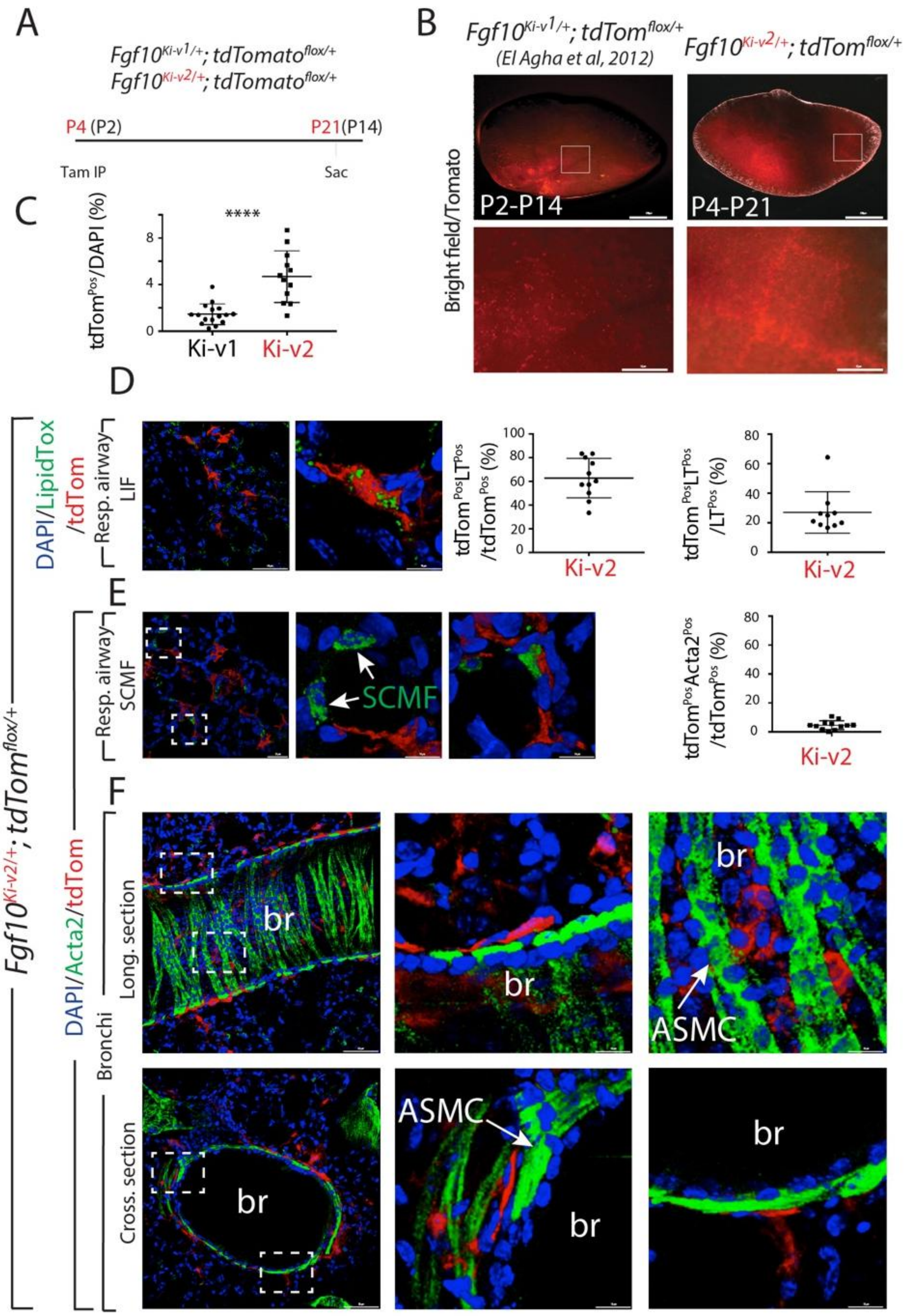

Figure 15. FGF10+ cells labeled after birth do not contribute significantly to secondary crest myofibroblasts during alveologenesis. (A) FGF10+ cells

in *Fgf10*$^{Ki\text{-}v2/+}$*; tdTomato*$^{flox/+}$ pups were labeled *in vivo* at P4 and analyzed at P21. We also used previously generated *Fgf10*$^{Ki\text{-}v1/+}$*; tdTomato*$^{flox/+}$ samples labeled between P2 and P14. **(B)** Whole-mount fluorescence images of *Fgf10*$^{Ki\text{-}v2/+}$; *tdTom*$^{flox/+}$ and *Fgf10*$^{Ki\text{-}v1/+}$; *tdTom*$^{flox/+}$ lungs showing more abundant labeled cells in *Fgf10*$^{Ki\text{-}v2/+}$ vs. *Fgf10*$^{Ki\text{-}v1/+}$ lungs. **(C)** ACTA2 IF on *Fgf10*$^{Ki\text{-}v2/+}$; *tdTom*$^{flox/+}$ lungs show little contribution of FGF10+ cells to SCMF (ACTA2+tdTom+/ACTA2+). **(D)** Quantification of tdTom+ cells. Br: bronchi. Scale bar in (B): low magnification: 0.5 mm, High magnification: 50 µm. Scale bar in (D): low magnification: 50 µm, High magnification: 10 µm. Scale bar in (**E**): low magnification: 25 µm, High magnification: 10 µm. Scale bar in **(F)**: Low magnification: 50 µm, High magnification: 10 µm. ****$P \leq 0.0001$**.** (Chu, Taghizadeh et al. 2021)

The new *Fgf10*$^{Ki\text{-}v2}$ line allows more efficient labelling of FGF10+ cells in the adult lung compared with the previous *Fgf10*$^{KI\text{-}v1}$ line.

Two-month-old *Fgf10*$^{K\text{-}v2/+}$; *tdTomato*$^{flox/flox}$ mice were treated with Tam IP or oil at day 1 (D61), 3 (D63) and 5(D65) and the lungs were collected at day 7 (D67) (Fig. 15A). No fluorescent signal was observed in oil-treated *Fgf10*$^{K\text{-}v2/+}$; *tdTomato*$^{flox/flox}$ mice, indicating that the line is not leaky. By contrast, a solid signal was found in Tam-treated *Fgf10*$^{Ki\text{-}v2/+}$; *tdTomato*$^{flox/flox}$ lungs. A weak signal was detected in Tam-treated *Fgf10*$^{Ki\text{-}v1/+}$; *tdTomato*$^{flox/flox}$ lungs as described in a previously study (El Agha, Herold et al. 2014) (Fig. 15B). Flow cytometry analysis was also conducted to quantify the total number of tdTom+ cells in both conditions and their identity (El Agha, Herold et al. 2014) (Fig. 15C). Only 0.3% tdTom+ cells over total number of cells were detected in *Fgf10*$^{Ki\text{-}v1/+}$; *tdTomato*$^{flox/flox}$*.* This number is in line with the previously reported 0.1% (El Agha, Herold et al. 2014) and confirms that the *Fgf10*$^{Ki\text{-}v1/+}$ line does not effeciently target FGF10+ cells in the adult lung. By contrast, we observed 5.8% of tdTom+ cells over total cells in *Fgf10*$^{Ki\text{-}v2/+}$ lungs. Further analysis showed that these cells were mostly CD31^{Neg}CD45^{Neg}EPCAM^{Neg} cells (85 %), identifying them as resident mesenchymal cells (rMC). 14.3% of the tdTom+ cells were also SCA1^{High}, a functional marker of the rMC subpopulation capable of sustaining the self-renewal of AT2 stem cells in the alveolosphere organoid model (Taghizadeh, Heiner et al. 2021).

Of note, 53% of the SCA1^{High} were LipidTOX+ identifying as lipofibroblasts (LIFs). Altogether these results suggest that tdTom+ cells are heterogeneous and comprise a significant percentile of LIFs as previously reported (El Agha, Herold et al. 2014).

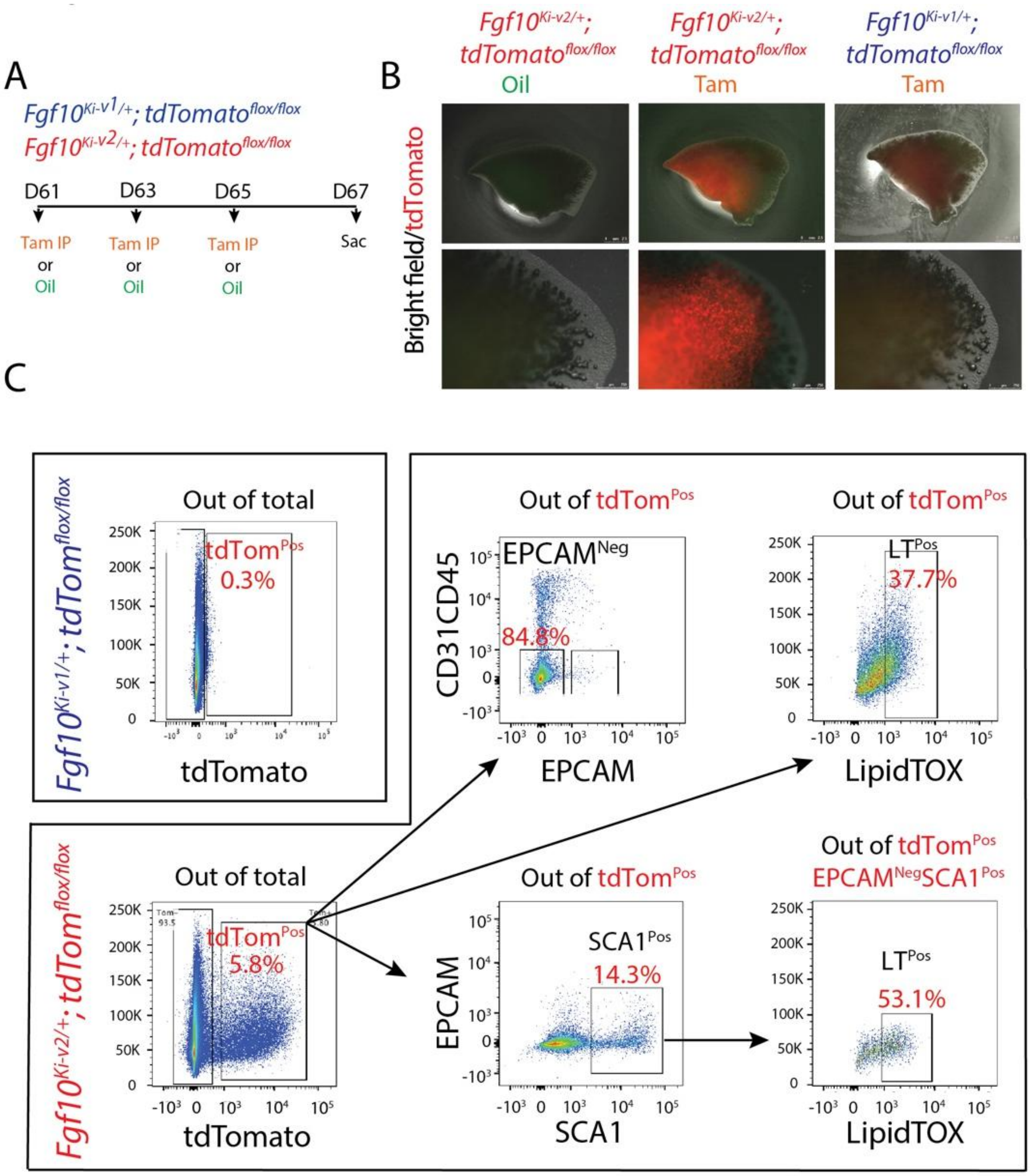

Figure 16. *Fgf10*$^{Ki-v2/+}$; *tdTom*$^{flox/+}$ adult lungs display enhanced number of tdTom+ cells compared to the *Fgf10*$^{Ki-v1/+}$; *tdTom*$^{flox/+}$ adult lungs. (A) 2-

months-old $Fgf10^{+/+}$; $Fgf10^{Ki\text{-}v1/+}$; $tdTom^{flox/+}$ and $Fgf10^{Ki\text{-}v2/+}$; $tdTom^{flox/+}$ mice received 3 Tam IPs or oil at P61, P63 and P65 and were sacrificed at P67. **(B)** Whole-mount fluorescence images of oil-treated $Fgf10^{Ki\text{-}v2/+}$; $tdTom^{flox/+}$, Tam-treated $Fgf10^{Ki\text{-}v2/+}$; $tdTom^{flox/+}$ and Tam-treated $Fgf10^{Ki\text{-}v1/+}$; $tdTom^{flox/+}$ lungs at P67. Higher magnification of the lungs is shown in the lower panel. **(C)** Flow cytometry analysis of $Fgf10^{Ki\text{-}v2/+}$; $tdTom^{flox/flox}$ mice lung homogenate. Scale bar in **(B)**: low magnification: 2.5 mm, High magnification: 0.75 mm. (Chu, Taghizadeh et al. 2021)

The 3'UTR region for *Fgf10* gene contains many key transcriptional factors binding sites.

The decrease in *Fgf10* expression in $Fg10^{Ki\text{-}v2}$ mice (data not shown) suggested that important transcription factor binding sites (TFBS) were impacted by the genetic manipulation in the 3'UTR of the *Fgf10* gene. We determined the identity of TFBS located at proximity of the 3'UTR of the *Fgf10* gene using an online TFBS prediction tool. We compared this TFBS with previously published TF expressed in the lung mesenchyme (Herriges, Yi et al. 2012). We found several key TFBS matching the previously reported TF expression in the lung, such as *Hoxa5*, *Pou3f1*, *Pou2f1*, *Foxm1* and *Meis1* (Fig. 17). Interestingly, all these transcription factors play a functional role in the lung. Mutant *Hoxa5* mice display decreased surfactant production and disrupted tracheal cartilage, leading to respiratory distress and low survival rate at birth (Aubin, Lemieux et al. 1997, Kinkead, LeBlanc et al. 2004, Mandeville, Aubin et al. 2006). *Pou3F1*, also known as *Oct6* is primarily expressed in neural cells. *Pou3F1* deletion caused lethality at birth due to respiratory distress (Bermingham, Scherer et al. 1996) (Bermingham, Shumas et al. 2002, Ghazvini, Mandemakers et al. 2002). The deletion of the other related transcription factor, *Pou2f1*, is associated with a smaller body size of embryos and fully lethality at birth (Wang, Schmidt et al. 2004). *Foxm1* expression plays a crucial role in both the epithelium and the mesenchyme. Conditional inactivation of *Foxm1* in the lung mesenchyme leads to increased smooth muscles around the proximal airways and reduced pulmonary microvasculature (Kim, Ramakrishna et al. 2005). In the lung epithelium, *Foxm1* conditional inactivation causes a reduction in sacculation and delayed differentiation of alveolar epithelial type I cells (Kalin, Wang et al. 2008).

Knockout of *Meis1* caused lethality during the embryonic stage around E14.5 due to microvascular and hematopoietic defects in the lung (Hisa, Spence et al. 2004).

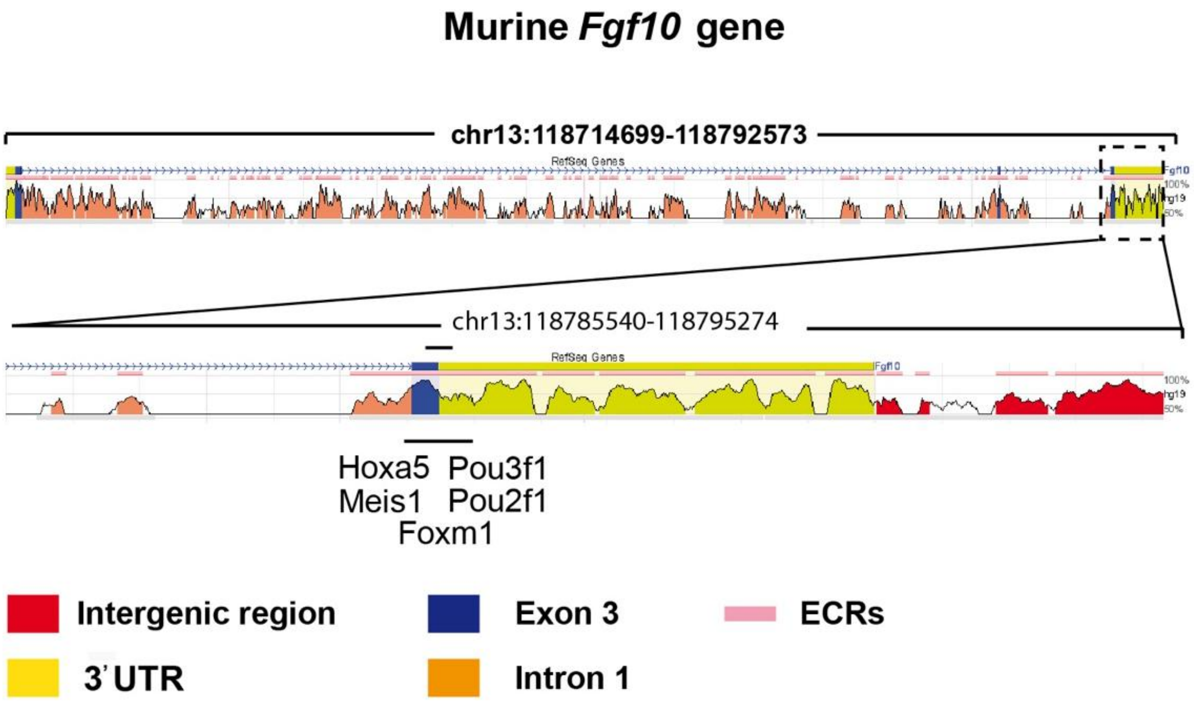

Figure 17. Bioinformatics analysis identified potential transcriptional factors binding sites in the 3′UTR of Exon 3. (A) The murine *Fgf10* gene compromises 3 exons. **(B)** High magnification of Exon 3 and the associated 3′UTR. Several putative important transcriptional factor binding sites were found in this region. (Chu, Taghizadeh et al. 2021)

FGF10+ cells are located around blood vessels in *Fgf10$^{Ki\text{-}v2/+}$; tdTom$^{flox/+}$* postnatal lungs.

To investigate the role of FGF10+ cells during the lung injury repair process, fate mapping of Fgf10+ cells in the adult stage became an essential task. Our new Fgf10$^{Ki\text{-}v2/+}$; tdTom$^{flox/+}$ mice line showed the capacity to label FGF10+ cells during the adult stage. Experimental mice were induced with tamoxifen i.p. injection at p4, and lungs were collected at postnatal day 21 (Figure 18A). Upon tamoxifen treatment to active Cre recombinase, FGF10+ cells were labelled with tdTom. As shown in IF images, the perivascular region of the lung is populated by FGF10+ cells (Figure 18B). Our previous studies showed that GLI1+ cells also reside in the perivascular niche of mice lungs. Therefore, we have proposed that FGF10 could prevent GLI1+ cells from differentiating to ACTA2-high PH-associated VSMCs. Combining the previous data, we could use the new *Fgf10* knock-in line to investigate the impact of FGF10 in the reverse remodeling stage following hypoxia and cigarette smoke induce PH.

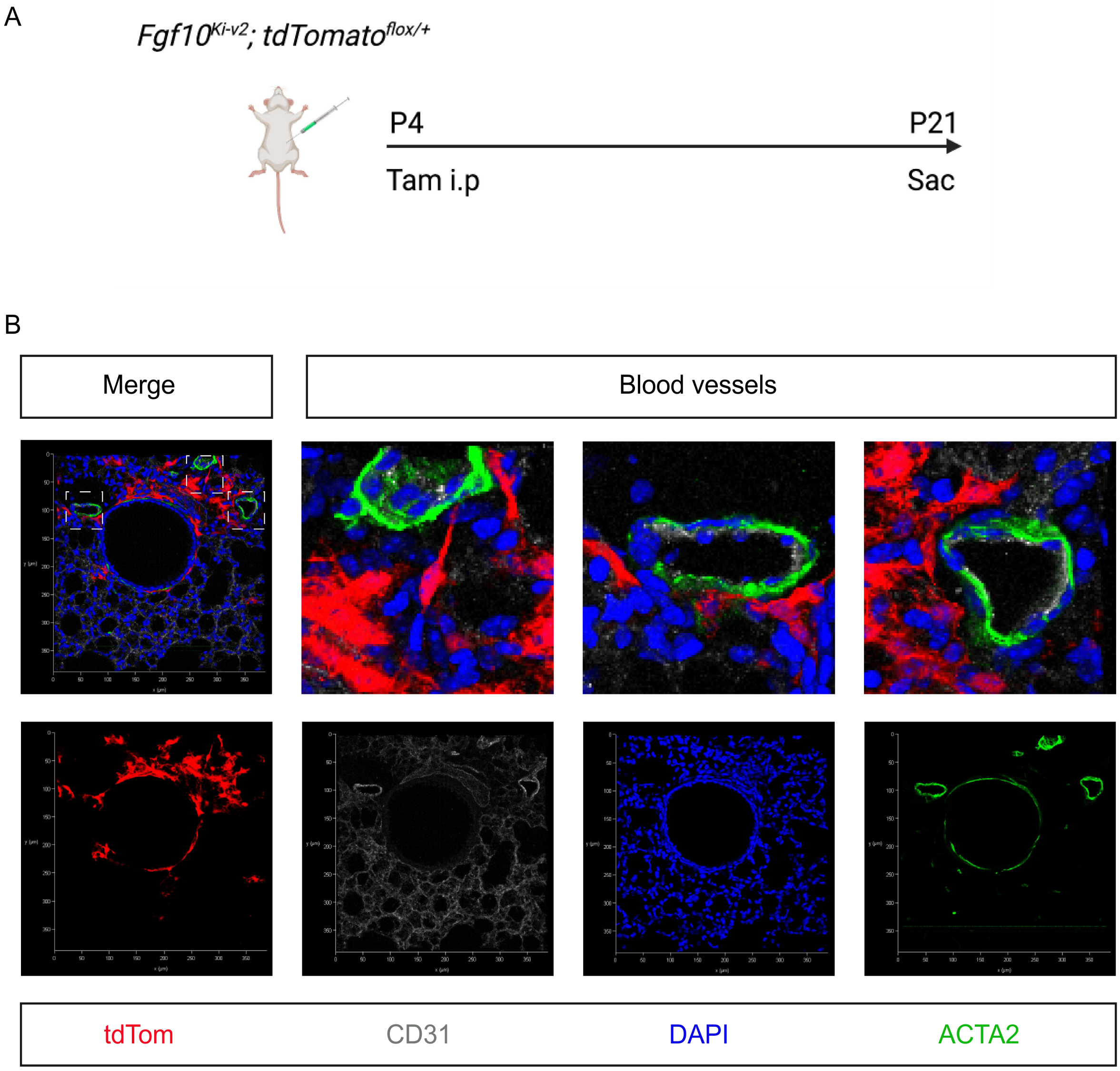

Figure 18. FGF10+ lineage cells were located around blood vessels in P21 *Fgf10*$^{Ki\text{-}v2/+}$; *tdTom*$^{flox/+}$ mice lung. (A). *Fgf10*$^{Ki\text{-}v2/+}$; *tdTom*$^{flox/+}$ mice were injected with tamoxifen at P4 to genetically label FGF10+ cells with red fluorescent tdTomato. **(B).** FGF10+ cells were found around perivascular and peribronchial sites. Post-natal day 4, P4; post-natal day 21, P21.

Discussion

Our study focussed on the GLI1+ cells in two models of vascular remodeling (HOX and SE) and reverse remodeling (HOX+ NOX and SE+L-NIL). These two models are widely used by the scientific community working on PH. We also combined lineage-tracing approaches with flow cytometry, IMARIS-based high resolution of confocal pictures, genetic ablation and scRNAseq to characterize the behavior of GLI1+ cells upon injury. Our results indicate a significant contribution of GLI1+ cells to vascular remodeling in PH and clearly demonstrated that clearance of these cells is associated with reverse remodeling. The GLI1+ cells also behaved differently in these two injury models. While HOX mainly involves differentiation of the GLI1+ cells towards the ACTA2 lineage, SE consists of both proliferation and differentiation of GLI1+ cells. We also found a different behavior of these cells in the SE model between the proximal and distal arterioles. Finally, scRNAseq allowed the identification of a cluster containing cells belonging to the SMC lineage. Velocity analysis indicates that differentiated VSMCs arise from distinct pools of SMC progenitors.

GLI1+ cells represent a critical population for pathological processes

GLI1+ cells are a major contributor to the pathogenetic ACTA2+ cells pool in idiopathic lung diseases, such as lung fibrosis, COPD, and pulmonary hypertension. Gli1 is a downstream target gene of hedgehog (*Hh*) signaling: It encodes for a transcription factor and is expressed in mesenchymal cells that reside adjacent to the SHH expressing airway epithelium (Peng, Frank et al. 2015). Studies have shown that GLI1+ cells exhibit properties of mesenchymal stem cells ex vivo (Kramann, Schneider et al. 2015). They have also been shown to contribute to fibrosis in the lung and other organs via differentiating into myofibroblasts and secreting collagen (Kramann, Schneider et al. 2015). In our study, we have shown that these cells reside in perivascular domains in the adult lungs. Furthermore, upon hypoxia- and cigarette-induced PH, GLI1+ cells integrate into the vessel wall and contribute to neo-muscularization during pulmonary remodeling in pulmonary arterioles. Therefore, GLI1+ cells play an essential role in the etiology of PH.

Challenging the dominant model that pre-existing vascular smooth muscle gives rise to newly formed PH-associated VSMCs.

To date, the accepted model regarding the formation of PH is that the pre-existing vascular smooth muscle located at the junction between muscularized and non-muscularized arterioles called “primed” VSMCs, migrate, dedifferentiate, expand and differentiate back to give rise to newly formed PH-associated VSMCs.

Primed VSMCs are positive for both SMC markers and the undifferentiated mesenchyme marker platelet-derived growth factor receptor-β (PDGFR-β). During hypoxic injury, the primed VSMCs express the pluripotency factor Krupple-like factor 4 (KLF4) and contribute to the neovascularization in distal vessels by migration dedifferentiation and proliferation. These results are essentially based on the lineage tracing of ACTA2+ cells and PDGFRβ+ cells to study the contribution of these cells in hypoxia-induced PH(Sheikh, Misra et al. 2015).

An exciting development of combining lineage tracing with scRNAseq is that it found that the driver line used to target a specific population is labeling more than expected. This discrepancy is often due to the fact that lineage tracing relies on capturing high-level reporter expressing cells, often ignoring low-level reporter expressing cells. Although the scRNAseq is a relatively unbiased method to dissect the heterogeneity of cells, it could reveal all the populations captured by a given driver. The GLI1+ cells are no exception; our scRNAseq shows that in addition to the SMC cluster, additional subpopulations of lung mesenchymal cells including lipofibroblasts, myofibroblasts/matrix fibroblasts and Col14a1+ matrix fibroblasts are observed. Similar results have been obtained using the *Acta2*$^{Cre\text{-}ERT2}$ driver (Lingampally and Bellusci, data not shown). Interestingly, these unexpected additional clusters also appear to react to the injury making it very challenging to pinpoint a precise exact subpopulation responsible for the pathological manifestations.

As a filter in our analysis, we focused on the ACTA2+ cluster, which when subclustered, contained at least 3 subpopulations (Subcluster 9, that we identified to be the VSMCs and 8 and 10, which represented the progenitors for the VSMCs based on our velocity analysis). Interestingly, *Pdgfrβ* expression is scattered among all these 3 clusters,

challenging the idea of a specific PDGFRβ+ progenitor for VSMCs. The controversies arising from using a single driver to label "specific" cell populations can in the future be resolved by the use of dual drivers (for 2 markers of a specific population) allowing to label cells expressing simultaneously the 2 markers. For example, *Cre* will be under the control of the first driver and *Dre* under the control of a second driver. In addition, the use of specific reporter mice for *Cre/Dre* activity will increase the specificity of the lineage tracing. To date, such specific markers are still unclear.

The ultimate test for the pathological relevance of GLI1+ cells in the context of PH

Genetic ablation of GLI1+ cells has been carried out to determine if GLI1+ cells are functionally involved in the pathogenesis of PH. A previous study from Kramman's group has shown that the deletion of GLI1+ cells substantially ameliorate the kidney and heart fibrosis caused by injury. They concluded that GLI1+ cells contribute to organ fibrosis, which can be a potential therapeutic target to treat injury-induced organ fibrosis. We have also performed genetic ablation of GLI1+ cells during hypoxia-induced PH. The hemodynamic and echocardiography results showed an improvement of PH in heart and lung functions indicating in a non-equivocal way that these cells are responsible for PH pathogenesis in this model.

Further investigation with FACS and IF on GLI1+ cells in the lung has been carried out. The IF images generated from PCLS found that the fluorescent-labelled GLI1+ cells decreased significantly around and in the arterioles. However, the FACS results showed only a 40% decrease of GLI1+ cells using lung homogenates. This discrepancy illustrates the necessity to define better which sub-population of GLI1+ cells is impacted.

Difference between hypoxia- and cigarette-induced PH

The cigarette smoke-induced PH model was first introduced to study pulmonary hypertension by Weissman’s group while investigating the pathogenesis of COPD(Seimetz, Parajuli et al. 2011). The clinical data collected by this group showed that about 30%-70% of COPD patients also develop PH (Seimetz, Parajuli et al. 2011). Additionally, there is increasing evidence showing that cigarette smoke has a

direct impact on pulmonary vascular dysfunction. In their study, WT mice were exposed to cigarette smoke for up to eight months. In the first three months of cigarette smoke exposure, the development of right heart hypotrophy was first detected. Within six months, lung emphysema is observed, followed by pulmonary hypertension. They have also shown that the muscularization level of pulmonary arterioles increased, which is one of the hallmarks of PH, after eight months of cigarette smoke exposure. Chronic hypoxia is one of the most commonly used animal models to induce PH in mice and rats. Compared to other traditionally utilized injury models, such as monocrotaline (MCT) injection in rats, the induction of PH by chronic hypoxia is less severe but more stable in terms of hemodynamics measurements, right ventricle hypertrophy and vascular wall thickening. Furthermore, chronic hypoxia exposure is more predictable and reproducible compared to other models.

Although the endpoint of the two injury models introduced in this study is similar, they may involve totally different mechanisms in the context of disease development. The increased muscularization of arterioles can be found in both cases. However, different features of each injury model were found in our investigation. In the FACS analysis, it was found that there is no apparent proliferation of GLI1+ cells in the hypoxia model. The contribution of GLI1+ cells to newly formed ACTA2+ cells showed a clear trend of increase. The results indicated that upon hypoxic injury, differentiation of GLI1+ cells rather than simple amplification took place. However, In the smoke-induced PH model, the number of GLI1+ cells increased significantly in FACS analysis, which indicated that smoke-induced PH involved both proliferation and differentiation of GLI1+ cells. In terms of re-exposure study, the quantification results between the two models are more diverse. During the recovery stage of hypoxia-induced PH, the numbers of GLI1+ cells maintained similar to the GLI1+ cell number in the experimental stage, as shown in

figure 5D. The treatment of L-NIL in SE mice caused a reduction of GLI1+ cells shown in both FACS and IF analysis. When comparing the contribution of resident ACTA2+ cells to newly formed muscularization in both injury models, we found the impact of hypoxia injury is more profound than SE injury, as shown in FACS analysis data. However, L-NIL treatment is more effective in rescuing the neomuscularization in SE injury than re-exposure to normoxia in HOX injury. The various level of recovery indicates another potential difference between these two injury models. This may be due to the different underlining mechanisms, as L-NIL, an iNOS inhibitor, works directly in inducing oxidative stress. In conclusion, although the neomuscularization of pulmonary arterioles occurred in both injury models. The level of muscularization in proximal and distal arterioles are different indicated by both FACS data and IF analysis on PCLS. The severity of the PH onset is not occurring at the same level. During the vascular reverse remodeling stage, the recovery process is also different.

In conclusion, we have shown that GLI1+ cells represent a major functional contributor to PH in two mouse models. We have also shown different cellular mechanisms are at work between hypoxia and smoke. In the future, further analysis of the GLI1+ cell subpopulation causative for PH needs to be carried out. Significant refinements of the existing model need to be done to integrate the GLi1+ cells. Targeting the GLI1+ cells could therefore represent a valid therapy to treat PH patients.

Involvements of fibroblast growth factors 10 (FGF10) in the lung during homeostasis and injury repair

FGF10 is an essential morphogen underlying the developmental process of multiple organs, including the lung. FGF10 signaling is also crucial during homeostasis and in the process of injury/repair in the adult lung. In addition, FGF10 dysregulation in humans has been implicated in some major respiratory diseases, such as bronchopulmonary dysplasia (BPD), Idiopathic pulmonary fibrosis (IPF) and chronic obstructive pulmonary disease (COPD) (Yuan, Volckaert et al. 2018).

In IPF, increased FGF10 expression level in IPF patients has been found (El Agha, Moiseenko et al. 2017). However, FGF10 expression is inversely correlated to the disease progression with higher levels in stable IPF vs. lower levels in end-stage IPF. Therefore, higher FGF10 expression in the early, stable stage of IPF is most likely correlated with the repair process.

Insufficient FGF10 level in prematurely newborn infants is associated with arrested lung development at the saccular stage (Prince 2018). In addition, *Fgf10* deficiency in a newborn mouse model of hyperoxia-induced BPD led to the drastic increase in lethality associated with abnormal alveolar epithelial type 2 (AT2) cell differentiation as well as surfactant production (Chao, Yahya et al. 2017).

In COPD, the conducting airway epithelium undergoes massive remodeling causing an irreversible airway obstruction (Decramer, Janssens et al. 2012) (Decramer et al., 2012). Interestingly, we have reported that the FGF10-HIPPO epithelial-mesenchymal crosstalk also maintains and recruits lung basal stem cells in the conducting airways (Volckaert, Yuan et al. 2017). While transient Fgf10 expression by ASMCs is critical for proper airway epithelial regeneration in response to injury, sustained FGF10 secretion by the ASMC niche, in response to chronic ILK/HIPPO inactivation, results in pathological changes in airway architecture resembling the abnormalities seen in COPD. Therefore, the inhibition of FGF10/FGFR2b signaling may be an inovative approach to treat chronic obstructive airway lung diseases. Conversely, the opposite situation might occur in the respiratory airways in that destruction of the alveolar compartments resulting in emphysema may be due to insufficient FGF signaling. Interestingly, recombinant FGF7 has been reported to induce de novo-alveologenesis in the elastase model of emphysema in mice (Yildirim, Muyal et al. 2010) .

The need for a new *Fgf10*$^{Cre–ERT2}$ knock-in mouse Line targeting FGF10+ cells postnatally.

The previous *Fgf10*$^{Ki–V1}$ model was mainly used to trace the FGF10+ cells during embryonic development. A near-complete loss of the labeling capacity of FGF10+ cells during postnatal stages limited its utilization in the analysis of their cell fate in adult lung homeostasis and during the process of injury/repair. To overcome the limitations of the *Fgf10*$^{Ki–V1}$ line, we generated and validated this new knock-in *Fgf10*$^{Ki–V2}$ line. Upon crossing with a tdTomato reporter line, we demonstrated that the tdTomato expression domain faithfully reproduced the previously reported *Fgf10* expression pattern (El Agha, Al Alam et al. 2012). A more robust labeling of FGF10+ cells was achieved in the postnatal period despite of a mismatch between *Cre* and *Fgf10* expression, which could be explained by the disruption of critical TFBS located in the 3′UTR of the *Fgf10* gene. Therefore, this line will be a valuable tool to further define mesenchymal cell populations in the adult lung contributing to the repair process after injury. Combined crosses with existing or novel *Dre-ERT2* recombinase driver lines may allow to capture subpopulations of FGF10+ cells/lineages based on the expression of two markers (Jones, Zhang et al. 2019). The main FGF10+ subpopulation is represented by the lipid-containing alveolar interstitial fibroblasts (lipofibroblasts or LIFs). More and more studies have acknowledged LIFs as an essential piece of the AT2 stem cell niche in the rodent lungs. Although LIFs were initially believed to only assist AT2 cells in surfactant production during neonatal life, recent studies have shown that these cells are essential for self-renewal and differentiation of AT2 stem cells during adulthood (Barkauskas, Cronce et al. 2013). Despite of the increasing interest in lipofibroblast biology, little is known about their cellular origin or the molecular pathways that control their formation during embryonic development. We have shown that in the developing mouse lung, FGF10+ cells labeled at E11.5 or E15.5 are progenitors for LIFs (El Agha, Herold et al. 2014). In addition, FGF10 is also essential for the differentiation of these progenitors into the LIF lineage (Al Alam, El Agha et al. 2015). We have also reported the existence of FGF10 positive LIFs and FGF10 negative LIFs (Al Alam, El Agha et al. 2015). The difference between these two populations is still unclear and will require further studies. In the context of bleomycin-induced lung fibrosis, in vivo lineage tracing indicates that LIFs transdifferentiate into activated myofibroblast during fibrosis formation and that a significant proportion of the labeled activated myofibroblasts transdifferentiate back to LIFs during fibrosis resolution (El Agha, Moiseenko et al. 2017).

In conclusion, we have successfully generated a new Fgf10$^{Cre–ERT2}$ line with enhanced labeling efficiency of FGF10+ cells postnatally. This line, which displays a normal expression of Fgf10 in Fgf10$^{Cre–ERT2/+}$, avoids many developmental defects linked to deficient Fgf10 expression. Therefore, it paves the way for performing cell-autonomous based studies to investigate the role of these FGF10+ cells and associated signaling pathways during lung development and disease.

FGF10: a new therapeutic candidate of PH?

During organogenesis and pathogenesis, fibroblast growth factor 10 (Fgf10) regulates mesenchymal cell differentiation in the lung. Different cell types reside in the developing lung mesenchyme. Lineage tracing in vivo was used to characterize these cells during development and disease. FGF10+ cells in the early lung mesenchyme differentiate into multiple lineages, including smooth muscle cells (SMCs), lipofibroblasts (LIFs) and other cell types, which remain to be characterized.

A recent study from Ornitz's group has shown that FGFR1/2 signalling in endothelial cells has a protective role in hypoxia-induced PH (Woo, Shen et al. 2021). Deletion of FGFRs in endothelial cells in mice shows an increased severity of PH development upon hypoxic injury. Another study has reported a clinical case that the utilization of nintedanib could exacerbate the onset of PH in IPF patients (Shimomura, Abe et al. 2019). Nintedanib is an inhibitor of FGFR. Additionally, FGF10 expression is decreased in BPD (Bronchopulmonary dysplasia) where PH development is preponderant (Chao, Yahya et al. 2017).Combining all the evidence, it is rational to hypothesize that the FGF10 signalling pathway could protect against PH-associated vascular remodeling.

Interestingly, in one of our recent studies, we demonstrated a group of GLI1+ cells secreted FGF10 during lung injury. Upon naphthalene-induced lung injury, the GLI1+ and FGF10+ cells have a supportive repair role of the bronchial epithelium (data not shown). The GLI1+ cell lineage expressed a low level of ACTA2 and was adjacent to the ACTA2+ SMCs. Gathering all the evidence, we proposed that the GLI1+ cells expressing FGF10 are involved in the repair process during the reverse remodeling of PH. we have shown that GLI1+ cells reside in the perivascular niche of lungs. These cells give rise to newly formed VSMC upon hypoxia- and cigarette smoke-induced PH. We have also gathered the evidence to show that FGF10 is involved in the vascular reverse remodeling process following cigarette smoke induce PH and subsequent RR due to treatment with iNOS inhibitor, L-NIL (Hadzic, Weissmann and Bellusci, personal communication). In the future, it is, therefore, necessary to investigate the fate and role of FGF10/GLI double-positive cells in the context of hypoxia and smoke-induced PH.

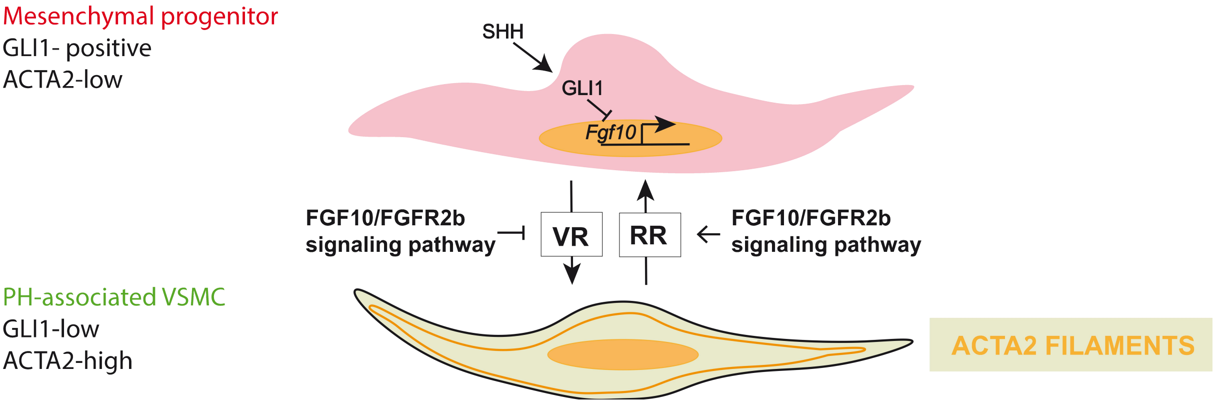

Figure 19. Proposed schematic model of crosstalk between GLI1+ mesenchymal progenitor cells and PH-associated VSMC. GLI1+ mesenchymal progenitor cells express low-level ACTA2 transdifferentiated into PH-associated VSMC with a high level of ACTA2+ expression. Expression of FGF10 prevents vascular formation from occurring in PH.

Conclusion

Overall, this study gives more insight into the cell fate of GLI1+ cells during vascular remodeling and reverses remodeling and offers an extensive characterization of the novel FGF10 transgenic mice line during the embryonic and postnatal stages.

The first part of the study gives a better understanding of the origin and fate of VSMCs in pulmonary hypertension. *Gli1*$^{Cre\text{-}ERT2}$*; tdTomoto*^{flox} line was used to analyze the contribution of GLI1+ cells to the newly formed VSMCs during two PH models: hypoxia-induced PH and smoke-induced PH. In both injury models, GLI1+ cells significantly contributed to the newly formed ACTA2+ cells in the blood vessels walls, especially in the distal arterioles. Although GLI1+ cells give rise to the newly formed ACTA2+ cells in vasculature, it is unknown if they were functionally involved in the pathogenesis of PH. *Gli1*$^{Cre\text{-}ERT2}$*; tdTomoto*^{flox}*; iDTR*^{flox} line was used to carry out genetic cell ablation in vivo. Upon administration of tamoxifen and diphtheria toxin, GLI1+ cells in the experimental mice were partially removed. Confirmed with echocardiography and lung function measurements, partial ablation of GLI1+ cells before hypoxia injury protects mice from PH development. Our results provide a novel view of the origin of disease-associated VSMCs, challenging the current thoughts that injury-related VSMCs arise from resident SMCs.

The second part of this study validates a new *Fgf10* knock-in transgenic mice line. More recent studies have shown that FGF10 has vital role in vascular remodeling in injury repair. Previously *Fgf10* knock-in mice were not sufficient to label FGF10+ cells in the postnatal stage. As a result, a novel line was designed and made. Our results show that the new *Fgf10* line is more efficient in labelling the target cells in the developmental and postnatal stages. The novel Fgf10 line allows us to study the behaviour and function of fgf10 cells in the lung injury and repair process.

.

Summary

Through the utilization of *Gli1*$^{Cre\text{-}ERT2}$ mice, the pathological role of the Gli1+ cells in PH have been delineated in this study. Previous studies showed that the perivascular niche of lung is populated by the mesenchymal Gli1+ population, which has been described as mesenchymal stem cells as its ability of trilineage differentiation in vitro. A subpopulation of the GLI1+ cell lineage is positive for PDGFRβ, giving rise to myofibroblast in lung fibrosis. In our study, IF analysis on lineage labeled GLI1+ cells contribute to the pool of newly formed ACTA2+ cells in mice hypoxia- and smoke-induced PH models. Furthermore, through the FACSs analysis, we found that the linage-labeled Gli1+ cells underwent differentiation rather than proliferation in the hypoxia-induced PH model. The percentage of Gli1+ cells in the hypoxia condition is comparable with the normoxia condition in the context of a significant increase of ACTA2+ cells in hypoxia-treated lungs. However, this situation is not applied in smoke-induced PH model. Although the percentage of ACTA2+ cells in the smoke group increased, the percentage of linage labeled Gli1+ cells also increased significantly under smoke-exposure conditions compared with room air exposure conditions. This result reveals differences between the mechanisms of the two PH models, despite similar outcomes. Further investigation is required to delineate better the mechanisms involved in these two injury models.

In an attempt to investigate the functional role of GLI1+ cells in hypoxia-induced PH, a genetic cell ablation experiment was carried out. Upon the tamoxifen and DTX administration, nearly 40% of GLI1+ cells have been ablated in *Gli1*$^{Cre\text{-}ERT2}$*; tdTomato*^{flox}*; iDTR*^{flox} lung, which was confirmed by FACS analysis. Echocardiography and IF analysis showed that the partial deletion of GLI1+ cells in mice protects the lungs from the onset of PH.

FGF10 secreted by mesenchyme is the most important growth factor in epithelium and mesenchyme interaction during lung development. GLI1+ cells are located in the perivascular and peribronchial site. Our previous study has shown that GLI1+ cells served as a source of a group of repair supportive smooth muscle cells. Deleting FGF10 in GLI1+ cells, using *Gli1*$^{Cre\text{-}ERT2}$*; Fgf10*^{flox}*; tdTomato*^{flox} line, impaired the FGF10-mediated repair process in airway epithelium caused by naphthalene injury.

Combining all the findings, FGF10 is a significant player in the injury repair process of the lung. We have generated a new FGF10 knock-in line, which allows us to lineage trace FGF10+ cells in the postnatal stage.

Last but not least, scRNA-seq was performed on *Gli1*$^{Cre\text{-}ERT2}$*; tdTomato*^{flox} mice. Twelve different subpopulations have been identified, which is consistent with the IF analysis PCLS. We found that cells from cluster 9 express vascular smooth muscle cell markers among all the clusters. Cluster 8 and 10 also express smooth muscle cell markers. Velocity analysis showed that clusters 8 and 10 are the progenitor cells of cluster 9.

Zusammenfassung

Durch die Verwendung von *Gli1*$^{Cre\text{-}ERT2}$-Mäusen wurde in dieser Studie die pathologische Rolle der Gli1+-Zellen bei PH aufgezeigt. Frühere Studien zeigten, dass die perivaskuläre Nische von der mesenchymalen Gli1+-Population besiedelt ist, die als mesenchymale Stammzellen aufgrund ihrer Fähigkeit zur Triliniendifferenzierung in vitro beschrieben wurde. Eine Subpopulation der GLI1+-Zelllinie ist positiv für PDGFRβ, was zu Myofibroblasten bei Lungenfibrose führt. In unserer Studie trägt die IF-Analyse an als GLI1+ markierten Zellen zum Pool neu gebildeter ACTA2+-Zellen in hypoxie- und rauchinduzierten PH-Modellen von Mäusen bei. Darüber hinaus fanden wir durch die FACSs-Analyse heraus, dass die Linien-markierten Gli1+-Zellen im Hypoxie-induzierten PH-Modell eher eine Differenzierung als eine Proliferation durchliefen. Der Prozentsatz an Gli1+-Zellen im Hypoxie-Zustand ist vergleichbar mit dem Normoxie-Zustand im Zusammenhang mit einem signifikanten Anstieg von ACTA2+-Zellen in Hypoxie-behandelten Lungen. Diese Situation wird jedoch nicht im rauchinduzierten PH-Modell angewendet. Obwohl der Prozentsatz der ACTA2+-Zellen in der Rauchgruppe zunahm, stieg der Prozentsatz der mit Gli1+ markierten Zelllinien unter Rauchexpositionsbedingungen im Vergleich zu Raumluftexpositionsbedingungen ebenfalls signifikant an. Dieses Ergebnis zeigt trotz ähnlicher Ergebnisse Unterschiede zwischen den Mechanismen der beiden PH-Modelle. Weitere Untersuchungen sind erforderlich, um die an diesen beiden Verletzungsmodellen beteiligten Mechanismen besser abzugrenzen.

Bei einem Versuch, die funktionelle Rolle von GLI1+-Zellen bei Hypoxie-induzierter PH zu untersuchen, wurde ein genetisches Zellablationsexperiment durchgeführt. Nach der Verabreichung von Tamoxifen und DTX wurden fast 40 % der GLI1+-Zellen in *Gli1*$^{Cre\text{-}ERT2}$ abgetragen; *tdTomato*^{flox}*; iDTR*^{flox} Lunge, was durch FACS-Analyse bestätigt wurde. Echokardiographie und IF-Analyse zeigten, dass die partielle Deletion von GLI1+-Zellen bei Mäusen die Lunge vor dem Ausbruch von PH schützt.

FGF10, das von Mesenchym sezerniert wird, ist der wichtigste Wachstumsfaktor bei der Interaktion von Epithel und Mesenchym während der Lungenentwicklung. GLI1+-Zellen befinden sich in der perivaskulären Nische und im peribronchialen Raum.

Unsere vorherige Studie hat gezeigt, dass GLI1+-Zellen als Quelle für eine Gruppe von reparaturunterstützenden, glatten Muskelzellen dienten. Löschen von FGF10 in GLI1+-Zellen unter Verwendung von Gli1Cre-ERT2; Fgf10flox; tdTomatoflox-Linie, beeinträchtigte den FGF10-vermittelten Reparaturprozess im Atemwegsepithel, verursacht durch

Naphthalin-Verletzung. Kombiniert man alle Erkenntnisse, spielt FGF10 eine wichtige Rolle im Heilungsprozess von Verletzungen der Lunge. Wir haben eine neue FGF10-Knock-in-Linie generiert, die es uns ermöglicht, FGF10+-Zellen im postnatalen Stadium zu verfolgen.

Zu guter Letzt wurde scRNA-seq auf Gli1Cre-ERT2 durchgeführt; tdTomatoflox-Mäuse. Zwölf verschiedene Subpopulationen wurden identifiziert, was mit der IF-Analyse PCLS übereinstimmt. Wir fanden heraus, dass Zellen aus Cluster 9 Marker für vaskuläre glatte Muskelzellen unter allen Clustern exprimieren. Cluster 8 und 10 exprimieren auch Marker für glatte Muskelzellen. Die Geschwindigkeitsanalyse zeigte, dass die Cluster 8 und 10 die Vorläuferzellen von Cluster 9 sind.

Reference List

Al Alam, D., E. El Agha, R. Sakurai, V. Kheirollahi, A. Moiseenko, S. Danopoulos, A. Shrestha, C. Schmoldt, J. Quantius, S. Herold, C. M. Chao, C. Tiozzo, S. De Langhe, M. V. Plikus, M. Thornton, B. Grubbs, P. Minoo, V. K. Rehan and S. Bellusci (2015). "Evidence for the involvement of fibroblast growth factor 10 in lipofibroblast formation during embryonic lung development." Development 142(23): 4139-4150.

Arciniegas, E., A. B. Sutton, T. D. Allen and A. M. Schor (1992). "Transforming growth factor beta 1 promotes the differentiation of endothelial cells into smooth muscle-like cells in vitro." J Cell Sci 103 (Pt 2): 521-529.

Aubin, J., M. Lemieux, M. Tremblay, J. Bérard and L. Jeannotte (1997). "Early postnatal lethality in Hoxa-5 mutant mice is attributable to respiratory tract defects." Dev Biol 192(2): 432-445.

Barkauskas, C. E., M. J. Cronce, C. R. Rackley, E. J. Bowie, D. R. Keene, B. R. Stripp, S. H. Randell, P. W. Noble and B. L. Hogan (2013). "Type 2 alveolar cells are stem cells in adult lung." J Clin Invest 123(7): 3025-3036.

Bermingham, J. R., Jr., S. S. Scherer, S. O'Connell, E. Arroyo, K. A. Kalla, F. L. Powell and M. G. Rosenfeld (1996). "Tst-1/Oct-6/SCIP regulates a unique step in peripheral myelination and is required for normal respiration." Genes Dev 10(14): 1751-1762.

Bermingham, J. R., Jr., S. Shumas, T. Whisenhunt, E. E. Sirkowski, S. O'Connell, S. S. Scherer and M. G. Rosenfeld (2002). "Identification of genes that are downregulated in the absence of the POU domain transcription factor pou3f1 (Oct-6, Tst-1, SCIP) in sciatic nerve." J Neurosci 22(23): 10217-10231.

Bordenave, J., L. Tu, N. Berrebeh, R. Thuillet, A. Cumont, B. L. Vely, E. Fadel, S. Nadaud, L. Savale, M. Humbert, A. Huertas and C. Guignabert (2020). "Lineage Tracing Reveals the Dynamic Contribution of Pericytes to the Blood Vessel Remodeling in Pulmonary Hypertension." Arteriosclerosis, Thrombosis, and Vascular Biology 40(3): 766-782.

Carraro, G., A. Shrestha, J. Rostkovius, A. Contreras, C.-M. Chao, E. El Agha, B. MacKenzie, S. Dilai, D. Guidolin, M. M. Taketo, A. Günther, M. E. Kumar, W. Seeger, S. De Langhe, G. Barreto and S. Bellusci (2014). "miR-142-3p balances proliferation and differentiation of mesenchymal cells during lung development." Development 141(6): 1272-1281.

Chao, C. M., F. Yahya, A. Moiseenko, C. Tiozzo, A. Shrestha, N. Ahmadvand, E. El Agha, J. Quantius, S. Dilai, V. Kheirollahi, M. Jones, J. Wilhem, G. Carraro, H. Ehrhardt, K. P. Zimmer, G. Barreto, K. Ahlbrecht, R. E. Morty, S. Herold, R. G. Abellar, W. Seeger, R. Schermuly, J. S. Zhang, P. Minoo and S. Bellusci (2017). "Fgf10 deficiency is causative for lethality in a mouse model of bronchopulmonary dysplasia." J Pathol 241(1): 91-103.

Chu, X., N. Ahmadvand, J.-S. Zhang, W. Seeger, S. Bellusci and E. El Agha (2021). "Evidence for Multiple Origins of De Novo Formed Vascular Smooth Muscle Cells in Pulmonary Hypertension: Challenging the Dominant Model of Pre-Existing Smooth Muscle Expansion." International Journal of Environmental Research and Public Health 18(16): 8584.

Crisan, M., S. Yap, L. Casteilla, C. W. Chen, M. Corselli, T. S. Park, G. Andriolo, B. Sun, B. Zheng, L. Zhang, C. Norotte, P. N. Teng, J. Traas, R. Schugar, B. M. Deasy, S. Badylak, H. J. Buhring, J. P. Giacobino, L. Lazzari, J. Huard and B. Péault (2008). "A perivascular origin for mesenchymal stem cells in multiple human organs." Cell Stem Cell 3(3): 301-313.

Crnkovic, S., L. M. Marsh, E. El Agha, R. Voswinckel, B. Ghanim, W. Klepetko, E. Stacher-Priehse, H. Olschewski, W. Bloch, S. Bellusci, A. Olschewski and G. Kwapiszewska (2018). "Resident cell lineages are preserved in pulmonary vascular remodeling." J Pathol 244(4): 485-498.

Danopoulos, S., S. Parsa, D. Al Alam, R. Tabatabai, S. Baptista, C. Tiozzo, G. Carraro, M. Wheeler, G. Barreto, T. Braun, X. Li, M. K. Hajihosseini and S. Bellusci (2013). "Transient Inhibition of FGFR2b-ligands signaling leads to irreversible loss of cellular beta-catenin organization and signaling in AER during mouse limb development." PLoS One 8(10): e76248.

De Langhe, S. P., G. Carraro, D. Tefft, C. Li, X. Xu, Y. Chai, P. Minoo, M. K. Hajihosseini, J. Drouin, V. Kaartinen and S. Bellusci (2008). "Formation and Differentiation of Multiple Mesenchymal Lineages during Lung Development Is Regulated by β-catenin Signaling." PLOS ONE 3(1): e1516.

Decramer, M., W. Janssens and M. Miravitlles (2012). "Chronic obstructive pulmonary disease." Lancet 379(9823): 1341-1351.

Diaz-Flores, L., R. Gutierrez, J. F. Madrid, H. Varela, F. Valladares, E. Acosta, P. Martin-Vasallo and L. Diaz-Flores, Jr. (2009). "Pericytes. Morphofunction, interactions and pathology in a quiescent and activated mesenchymal cell niche." Histol Histopathol 24(7): 909-969.

Dierick, F., T. Hery, B. Hoareau-Coudert, N. Mougenot, V. Monceau, C. Claude, M. Crisan, V. Besson, P. Dorfmuller, G. Marodon, E. Fadel, M. Humbert, E. Yaniz-Galende, J. S. Hulot, G. Marazzi, D. Sassoon, F. Soubrier and S. Nadaud (2016). "Resident PW1+ Progenitor Cells Participate in Vascular Remodeling During Pulmonary Arterial Hypertension." Circ Res 118(5): 822-833.

El Agha, E., D. Al Alam, G. Carraro, B. MacKenzie, K. Goth, S. P. De Langhe, R. Voswinckel, M. K. Hajihosseini, V. K. Rehan and S. Bellusci (2012). "Characterization of a novel fibroblast growth factor 10 (Fgf10) knock-in mouse line to target mesenchymal progenitors during embryonic development." PLoS One 7(6): e38452.

El Agha, E. and S. Bellusci (2014). "Walking along the Fibroblast Growth Factor 10 Route: A Key Pathway to Understand the Control and Regulation of Epithelial and Mesenchymal Cell-Lineage Formation during Lung Development and Repair after Injury." Scientifica 2014: 538379.

El Agha, E., S. Herold, D. Al Alam, J. Quantius, B. MacKenzie, G. Carraro, A. Moiseenko, C. M. Chao, P. Minoo, W. Seeger and S. Bellusci (2014). "Fgf10-positive cells represent a progenitor cell population during lung development and postnatally." Development 141(2): 296-306.

El Agha, E., R. Kramann, R. K. Schneider, X. Li, W. Seeger, B. D. Humphreys and S. Bellusci (2017). "Mesenchymal Stem Cells in Fibrotic Disease." Cell Stem Cell 21(2): 166-177.

El Agha, E., A. Moiseenko, V. Kheirollahi, S. De Langhe, S. Crnkovic, G. Kwapiszewska, M. Szibor, D. Kosanovic, F. Schwind, R. T. Schermuly, I. Henneke, B. MacKenzie, J. Quantius, S. Herold, A. Ntokou, K. Ahlbrecht, T. Braun, R. E. Morty, A. Gunther, W. Seeger and S. Bellusci (2017). "Two-Way Conversion between Lipogenic and Myogenic Fibroblastic Phenotypes Marks the Progression and Resolution of Lung Fibrosis." Cell Stem Cell 20(4): 571.

Feil, R., J. Wagner, D. Metzger and P. Chambon (1997). "Regulation of Cre recombinase activity by mutated estrogen receptor ligand-binding domains." Biochem Biophys Res Commun 237(3): 752-757.

Frid, M. G., V. A. Kale and K. R. Stenmark (2002). "Mature vascular endothelium can give rise to smooth muscle cells via endothelial-mesenchymal transdifferentiation: in vitro analysis." Circ Res 90(11): 1189-1196.

Galiè, N., M. Humbert, J. L. Vachiery, S. Gibbs, I. Lang, A. Torbicki, G. Simonneau, A. Peacock, A. Vonk Noordegraaf, M. Beghetti, A. Ghofrani, M. A. Gomez Sanchez, G. Hansmann, W. Klepetko, P. Lancellotti, M. Matucci, T. McDonagh, L. A. Pierard, P. T. Trindade, M. Zompatori and M. Hoeper (2016). "2015 ESC/ERS Guidelines for the diagnosis and treatment of pulmonary hypertension: The Joint Task Force for the Diagnosis and Treatment of Pulmonary Hypertension of the European Society of Cardiology (ESC) and the European Respiratory Society (ERS): Endorsed by: Association for European Paediatric and Congenital Cardiology (AEPC), International Society for Heart and Lung Transplantation (ISHLT)." Eur Heart J 37(1): 67-119.

Ghazvini, M., W. Mandemakers, M. Jaegle, M. Piirsoo, S. Driegen, M. Koutsourakis, X. Smit, F. Grosveld and D. Meijer (2002). "A cell type-specific allele of the POU gene Oct-6 reveals Schwann cell autonomous function in nerve development and regeneration." Embo j 21(17): 4612-4620.

Herriges, J. C., L. Yi, E. A. Hines, J. F. Harvey, G. Xu, P. A. Gray, Q. Ma and X. Sun (2012). "Genome-scale study of transcription factor expression in the branching mouse lung." Dev Dyn 241(9): 1432-1453.

Hisa, T., S. E. Spence, R. A. Rachel, M. Fujita, T. Nakamura, J. M. Ward, D. E. Devor-Henneman, Y. Saiki, H. Kutsuna, L. Tessarollo, N. A. Jenkins and N. G. Copeland (2004). "Hematopoietic, angiogenic and eye defects in Meis1 mutant animals." Embo j 23(2): 450-459.

Hopper, R. K., J. R. Moonen, I. Diebold, A. Cao, C. J. Rhodes, N. F. Tojais, J. K. Hennigs, M. Gu, L. Wang and M. Rabinovitch (2016). "In Pulmonary Arterial Hypertension, Reduced BMPR2 Promotes Endothelial-to-Mesenchymal Transition via HMGA1 and Its Target Slug." Circulation 133(18): 1783-1794.

Humbert, M., C. Guignabert, S. Bonnet, P. Dorfmüller, J. R. Klinger, M. R. Nicolls, A. J. Olschewski, S. S. Pullamsetti, R. T. Schermuly, K. R. Stenmark and M. Rabinovitch (2019). "Pathology and pathobiology of pulmonary hypertension: state of the art and research perspectives." Eur Respir J 53(1).

Jones, M., J.-S. Zhang and S. Bellusci (2019). "Bronchioalveolar stem cells vindicated!" Biotarget 3.

Jones, M. R., L. Chong and S. Bellusci (2020). "Fgf10/Fgfr2b Signaling Orchestrates the Symphony of Molecular, Cellular, and Physical Processes Required for Harmonious Airway Branching Morphogenesis." Front Cell Dev Biol 8: 620667.

Kalin, T. V., I. C. Wang, L. Meliton, Y. Zhang, S. E. Wert, X. Ren, J. Snyder, S. M. Bell, L. Graf, Jr., J. A. Whitsett and V. V. Kalinichenko (2008). "Forkhead Box m1 transcription factor is required for perinatal lung function." Proc Natl Acad Sci U S A 105(49): 19330-19335.

Kim, I. M., S. Ramakrishna, G. A. Gusarova, H. M. Yoder, R. H. Costa and V. V. Kalinichenko (2005). "The forkhead box m1 transcription factor is essential for embryonic development of pulmonary vasculature." J Biol Chem 280(23): 22278-22286.

Kinkead, R., M. LeBlanc, R. Gulemetova, M. Lalancette-Hébert, M. Lemieux, I. Mandeville and L. Jeannotte (2004). "Respiratory adaptations to lung morphological defects in adult mice lacking Hoxa5 gene function." Pediatr Res 56(4): 553-562.

Kramann, R., C. Goettsch, J. Wongboonsin, H. Iwata, R. K. Schneider, C. Kuppe, N. Kaesler, M. Chang-Panesso, F. G. Machado, S. Gratwohl, K. Madhurima, J. D. Hutcheson, S. Jain, E. Aikawa and B. D. Humphreys (2016). "Adventitial MSC-like Cells Are Progenitors of Vascular Smooth Muscle Cells and Drive Vascular Calcification in Chronic Kidney Disease." Cell Stem Cell 19(5): 628-642.

Kramann, R., R. K. Schneider, D. P. DiRocco, F. Machado, S. Fleig, P. A. Bondzie, J. M. Henderson, B. L. Ebert and B. D. Humphreys (2015). "Perivascular Gli1+ progenitors are key contributors to injury-induced organ fibrosis." Cell Stem Cell 16(1): 51-66.

Li, C., M. Li, S. Li, Y. Xing, C. Y. Yang, A. Li, Z. Borok, S. De Langhe and P. Minoo (2015). "Progenitors of secondary crest myofibroblasts are developmentally committed in early lung mesoderm." Stem Cells 33(3): 999-1012.
Lv, Y. Q., J. Wu, X. K. Li, J. S. Zhang and S. Bellusci (2019). "Role of FGF10/FGFR2b Signaling in Mouse Digestive Tract Development, Repair and Regeneration Following Injury." Front Cell Dev Biol 7: 326.

Mailleux, A. A., R. Kelly, J. M. Veltmaat, S. P. De Langhe, S. Zaffran, J. P. Thiery and S. Bellusci (2005). "Fgf10 expression identifies parabronchial smooth muscle cell progenitors and is required for their entry into the smooth muscle cell lineage." Development 132(9): 2157-2166.

Mandeville, I., J. Aubin, M. LeBlanc, M. Lalancette-Hébert, M. F. Janelle, G. M. Tremblay and L. Jeannotte (2006). "Impact of the loss of Hoxa5 function on lung alveogenesis." Am J Pathol 169(4): 1312-1327.

Mills, S. J., A. J. Cowin and P. Kaur (2013). "Pericytes, Mesenchymal Stem Cells and the Wound Healing Process." Cells 2(3): 621-634.

Moiseenko, A., V. Kheirollahi, C. M. Chao, N. Ahmadvand, J. Quantius, J. Wilhelm, S. Herold, K. Ahlbrecht, R. E. Morty, A. A. Rizvanov, P. Minoo, E. El Agha and S. Bellusci (2017). "Origin and characterization of alpha smooth muscle actin-positive cells during murine lung development." Stem Cells 35(6): 1566-1578.

Ntokou, A., J. M. Dave, A. C. Kauffman, M. Sauler, C. Ryu, J. Hwa, E. L. Herzog, I. Singh, W. M. Saltzman and D. M. Greif (2021). "Macrophage-derived PDGF-B induces muscularization in murine and human pulmonary hypertension." JCI Insight 6(6).

Pannérec, A., L. Formicola, V. Besson, G. Marazzi and D. A. Sassoon (2013). "Defining skeletal muscle resident progenitors and their cell fate potentials." Development 140(14): 2879-2891.

Passman, J. N., X. R. Dong, S.-P. Wu, C. T. Maguire, K. A. Hogan, V. L. Bautch and M. W. Majesky (2008). "A sonic hedgehog signaling domain in the arterial adventitia supports resident Sca1+ smooth muscle progenitor cells." Proceedings of the National Academy of Sciences of the United States of America 105(27): 9349-9354.

Peng, T., D. B. Frank, R. S. Kadzik, M. P. Morley, K. S. Rathi, T. Wang, S. Zhou, L. Cheng, M. M. Lu and E. E. Morrisey (2015). "Hedgehog actively maintains adult lung quiescence and regulates repair and regeneration." Nature 526(7574): 578-582.

Prince, L. S. (2018). "FGF10 and Human Lung Disease Across the Life Spectrum." Front Genet 9: 517.

Qiao, L., T. Nishimura, L. Shi, D. Sessions, A. Thrasher, J. R. Trudell, G. J. Berry, R. G. Pearl and P. N. Kao (2014). "Endothelial fate mapping in mice with pulmonary hypertension." Circulation 129(6): 692-703.

Ramasamy, S. K., A. A. Mailleux, V. V. Gupte, F. Mata, F. G. Sala, J. M. Veltmaat, P. M. Del Moral, S. De Langhe, S. Parsa, L. K. Kelly, R. Kelly, W. Shia, E. Keshet, P. Minoo, D. Warburton and S. Bellusci (2007). "Fgf10 dosage is critical for the amplification of epithelial cell progenitors and for the formation of multiple mesenchymal lineages during lung development." Dev Biol 307(2): 237-247.

Ranchoux, B., F. Antigny, C. Rucker-Martin, A. Hautefort, C. Péchoux, H. J. Bogaard, P. Dorfmüller, S. Remy, F. Lecerf, S. Planté, S. Chat, E. Fadel, A. Houssaini, I. Anegon, S. Adnot, G. Simonneau, M. Humbert, S. Cohen-Kaminsky and F. Perros (2015). "Endothelial-to-mesenchymal transition in pulmonary hypertension." Circulation 131(11): 1006-1018.

Ricard, N., L. Tu, M. Le Hiress, A. Huertas, C. Phan, R. Thuillet, C. Sattler, E. Fadel, A. Seferian, D. Montani, P. Dorfmuller, M. Humbert and C. Guignabert (2014). "Increased pericyte coverage mediated by endothelial-derived fibroblast growth factor-2 and interleukin-6 is a source of smooth muscle-like cells in pulmonary hypertension." Circulation 129(15): 1586-1597.

Sakao, S., H. Hao, N. Tanabe, Y. Kasahara, K. Kurosu and K. Tatsumi (2011). "Endothelial-like cells in chronic thromboembolic pulmonary hypertension: crosstalk with myofibroblast-like cells." Respiratory Research 12(1): 109.

Sala, F. G., P.-M. Del Moral, C. Tiozzo, D. A. Alam, D. Warburton, T. Grikscheit, J. M. Veltmaat and S. Bellusci (2011). "FGF10 controls the patterning of the tracheal cartilage rings via Shh." Development 138(2): 273-282.

Schermuly, R. T., H. A. Ghofrani, M. R. Wilkins and F. Grimminger (2011). "Mechanisms of disease: pulmonary arterial hypertension." Nat Rev Cardiol 8(8): 443-455.

Schneider, R. K., A. Mullally, A. Dugourd, F. Peisker, R. Hoogenboezem, P. M. H. Van Strien, E. M. Bindels, D. Heckl, G. Büsche, D. Fleck, G. Müller-Newen, J. Wongboonsin, M. Ventura Ferreira, V. G. Puelles, J. Saez-Rodriguez, B. L. Ebert, B. D. Humphreys and R. Kramann (2018). "Gli1(+) Mesenchymal Stromal Cells Are a Key Driver of Bone Marrow Fibrosis and an Important Cellular Therapeutic Target." Cell Stem Cell 23(2): 308-309.

Seimetz, M., N. Parajuli, A. Pichl, F. Veit, G. Kwapiszewska, Friederike C. Weisel, K. Milger, B. Egemnazarov, A. Turowska, B. Fuchs, S. Nikam, M. Roth, A. Sydykov, T. Medebach, W. Klepetko, P. Jaksch, R. Dumitrascu, H. Garn, R. Voswinckel, S. Kostin, W. Seeger, Ralph T. Schermuly, F. Grimminger, Hossein A. Ghofrani and N. Weissmann (2011). "Inducible NOS Inhibition Reverses Tobacco-Smoke-Induced Emphysema and Pulmonary Hypertension in Mice." Cell 147(2): 293-305.

Sheikh, Abdul Q., Janet K. Lighthouse and Daniel M. Greif (2014). "Recapitulation of Developing Artery Muscularization in Pulmonary Hypertension." Cell Reports 6(5): 809-817.

Sheikh, A. Q., A. Misra, I. O. Rosas, R. H. Adams and D. M. Greif (2015). "Smooth muscle cell progenitors are primed to muscularize in pulmonary hypertension." Sci Transl Med 7(308): 308ra159.
Shimomura, I., M. Abe, Y. Li, K. Tsushima, S. Sakao, N. Tanabe, M. Ikusaka and K. Tatsumi (2019). "Pulmonary Hypertension Exacerbated by Nintedanib Administration for Idiopathic Pulmonary Fibrosis." Intern Med 58(7): 965-968.

Steffes, L. C., A. A. Froistad, A. Andruska, M. Boehm, M. McGlynn, F. Zhang, W. Zhang, D. Hou, X. Tian, L. Miquerol, K. Nadeau, R. J. Metzger, E. Spiekerkoetter and M. E. Kumar (2020). "A Notch3-Marked Subpopulation of Vascular Smooth Muscle Cells Is the Cell of Origin for Occlusive Pulmonary Vascular Lesions." Circulation 142(16): 1545-1561.

Suzuki, T., E. J. Carrier, M. H. Talati, A. Rathinasabapathy, X. Chen, R. Nishimura, Y. Tada, K. Tatsumi and J. West (2018). "Isolation and characterization of endothelial-to-mesenchymal transition cells in pulmonary arterial hypertension." American Journal of Physiology-Lung Cellular and Molecular Physiology 314(1): L118-L126.

Taghizadeh, S., M. Heiner, J. Wilhelm, S. Herold, C. Chen, J. Zhang and S. Bellusci (2021). "Characterization in mice of the stromal niche maintaining AT2 stem cell self-renewal in homeostasis and disease." bioRxiv: 2021.2001.2028.428090.

Volckaert, T., T. Yuan, C. M. Chao, H. Bell, A. Sitaula, L. Szimmtenings, E. El Agha, D. Chanda, S. Majka, S. Bellusci, V. J. Thannickal, R. Fassler and S. P. De Langhe (2017). "Fgf10-Hippo Epithelial-Mesenchymal Crosstalk Maintains and Recruits Lung Basal Stem Cells." Dev Cell 43(1): 48-59 e45.

Wang, V. E., T. Schmidt, J. Chen, P. A. Sharp and D. Tantin (2004). "Embryonic lethality, decreased erythropoiesis, and defective octamer-dependent promoter activation in Oct-1-deficient mice." Mol Cell Biol 24(3): 1022-1032.

Woo, K. V., I. Y. Shen, C. J. Weinheimer, A. Kovacs, J. Nigro, C. Y. Lin, M. Chakinala, D. E. Byers and D. M. Ornitz (2021). "Endothelial FGF signaling is protective in hypoxia-induced pulmonary hypertension." J Clin Invest 131(17).

Yildirim, A. O., V. Muyal, G. John, B. Müller, C. Seifart, M. Kasper and H. Fehrenbach (2010). "Palifermin induces alveolar maintenance programs in emphysematous mice." Am J Respir Crit Care Med 181(7): 705-717.

Yuan, T., T. Volckaert, D. Chanda, V. J. Thannickal and S. P. De Langhe (2018). "Fgf10 Signaling in Lung Development, Homeostasis, Disease, and Repair After Injury." Front Genet 9: 418.

Zhang, Y., J. M. Fons, M. K. Hajihosseini, T. Zhang and A. S. Tucker (2020). "An Essential Requirement for Fgf10 in Pinna Extension Sheds Light on Auricle Defects in LADD Syndrome." Front Cell Dev Biol 8: 609643.

Acknowledgments

This project would not have been possible without the support of many people. So, I would like to show my appreciation in this section.

First of all, I would like to thank my Professor, Saverio Bellusci, who has been an ideal teacher, mentor and thesis supervisor. He has always provided advice and encouragements during my study. I extremely grateful that he took me on as a student and continued to have faith in me over years. Your invaluable feedback towards my thesis have been very important to me.

Furthermore, i would like to extend my special thanks to Prof. Dr. Elie El Algha as my mentor in the lab and tutor in MBML class. He has always been there to support and inspire me with his insightful ideas and constructive criticisms. He has taught me a lot from wet lab techniques, data analyzing to paper writing.

I also acknowledge Dr. Ana Ivonne Vazquez-Armendariz and Dr. Susanne Herold for their help with FACS. I would like to thank Stefan and Karin to help me with lung function and hemodynamics measurements. I would like to thank Dr. Simone Kraut for helping me with echocardiography measurements. I would like to thank Dr. Janine Koepke for helping with single cell sequencing.

Many thanks to Dr. Rory Morty, the former director of MBML program, who organized fabulous retreats for MBML students every year. I would like to thank Prof. Dr. Eveline Baumgart-Vogt and Dr. Lorna Lück, the organizers of the GGL program. I would also like to thank Prof. Dr. Werner Seeger, Prof. Dr. Norbert Weissmann, Prof. Dr. Andreas Günther and Dr. Stijn De Langhe for their advice and constructive criticism.

I would also like to thank my fabulous colleagues from Bellusci Lab for being such nice co-workers and making my work-life much easier. I want to thank Kerstin to help me with all my animal experiments. She taught me how to use the online animal organizing system. I want to thank Heike to help me with my apartment renting and settle down in the first couple days in Giessen. I want to thank Vahid, Alena and Cho for helping me and getting me familiar with the campus and lab. I would like to thank Arun to be a good classmate and colleague in MBML class and in the lab. We have studied and worked together for long time.

Finally, I would like to thank my family for helping me emotionally and financially. During the long journey of chasing my life-goal, from Canada to Australia and eventually to Germany, they have always stood by my side and been there for me. I am so grateful to have them in my life.

There are so many people who helped me during my PhD studies. I cannot express my fully appreciation here. I would like to wish all of them the brightest future in their life.